SYNTHESIS AND CHARACTERIZATION OF MAGNETIC NANOPARTICLES FOR USE AS SENSORS

By
Victoria L. Calero Díaz del Castillo

A thesis submitted in partial fulfillment of the requirements for the degree of

DOCTOR OF PHILOSOPHY
In
CHEMICAL ENGINEERING

UNIVERSITY OF PUERTO RICO
MAYAGÜEZ CAMPUS
June, 2009

Approved by:

_____	_____
Carlos Rinaldi, PhD President, Thesis Committee	Date
_____	_____
Oscar J. Perales-Perez, PhD Member, Thesis Committee	Date
_____	_____
Madeline Torres-Lugo, PhD Member, Thesis Committee	Date
_____	_____
Samuel P. Hernandez, PhD Member, Thesis Committee	Date
_____	_____
David Suleiman R., PhD Chair, Chemical Engineering	Date
_____	_____
Astrid Cruz Pol., PhD Graduate Studies Representative	Date

ABSTRACT

A comprehensive study of physical and magnetic properties of cobalt substituted ferrite and magnetite nanoparticles synthesized by thermal-decomposition was carried out. Initially, a systematic study of the effect of synthesis conditions on final size, crystalline structure, and composition of cobalt substituted ferrite nanoparticles synthesized by thermal-decomposition was carried out. Using a statistical design of experiments, the impact of the temperature and time during nucleation and growth stages on final particle size, lattice parameter, and Fe/Co ratio was determined.

Based on DC and AC susceptibility measurements, the effect of sample preparation on determination of the anisotropy constant of magnetite nanoparticles was studied. Magnetite nanoparticles synthesized by the thermal-decomposition method were fixed in a poly(styrene-divinylbenzene) matrix at 0.1%, 1%, and 6%(w/w). ZFC curves and the out-of-phase component of the dynamic susceptibility were obtained for each of sample and using Néel and Vogel-Fulcher models, the anisotropy constant was determined. The effect of particle size on the anisotropy constant of magnetite nanoparticles was also studied. In this case, magnetite with different diameter were synthesized by vary the synthesis conditions during thermal-decomposition method. Magnetite nanoparticles were fixed in poly(styrene-divinylbenzene) at 0.1% (w/w) and ZFC curves and AC susceptibility measurements were carried out

Finally, cobalt ferrite nanoparticles synthesized by the thermal-decomposition method were tested as possible sensors. Cobalt ferrite nanoparticles were functionalized with biotin using a COO^--silane coupling agent. Using AC measurements, avidin molecules at a concentration of 1 μM in aqueous solution could be detected by monitoring the change in Brownian relaxation time after the attachment of avidin molecule to biotinylized cobalt ferrite nanoparticle. This analysis required a sample volume of 100 μl and on 8 μg of the protein to be detected.

ACKNOWLEDGEMENTS

I want to thank everyone who shared with me in this period of my life, specially:

My labmates and friends: Adriana, Carola, Jorge, and Dennise for its help, adviser and friendship. Ana Maria, Ana G., Arlex, Gerardo, Marisol, and Richard for you friendship.

I specially want to thank my advisor Dr. Carlos Rinaldi for his support, help, and trust. Thank you.

Gladiz (my mom), Alex (my father), Kelly, Jenny (my sisters and friends), Melba, Victoria (my grandmothers) and Carlos (my uncle) for all their love and support during my life.

Dr. Arturo Hernandez for access to X-ray diffraction and Darlene Santiago and Roberto Olaya for help me with the measurements.
Dr. Boqueres for access to ICP and Yeira Padilla for help me with ICP runs.
Dr. Oscar Perales for access to TGA and DSC and Boris Renteria for help me with the measurements
Roberto Olayo for help me with DSC measurements
PREM for training and short courses which were very important in my development as a professional, and for supporting the project and me.
We acknowledge the UPR-Rio Piedras Center for Nanoscale Materials, financed by NASA-URC grants number NASA-NCC3-1034, for the use of the High Resolution Transmission Electron Microscope. We are grateful to Oscar Resto for assisting in taking our TEM images.
This work was supported by the US National Science Foundation (NSF), PREM program (DMR-0520527), the NSF CREST program (HRD-0833112) and the Puerto Rico Institute for Functional Nanomaterials, supported by the NSF EPSCoR program (OIA-0701525).

CONTENT

LIST OF FIGURES

1. INTRODUCTION

The synthesis of uniform, nanometer sized, and non-agglomerated particles of transition metal oxides has been the goal of several studies. This great interest in metal oxide materials is due to their magnetic, ferroelectric, superconducting, or electronic properties [1]. As a result of this great variety of properties, metal oxide nanoparticles have numerous potential applications such as in materials development, biomedical sciences, energy storage, electrochemistry, and others [2].

For many of these applications magnetic nanoparticles have been used because they can be manipulated through a magnetic field. In order to simplify interpretation of experiments it is essential to obtain monodisperse and non-agglomerated nanoparticles, and to understand the relaxation mechanism of the nanoparticles after a magnetic field is applied. One example of an application with strict requirements on the morphology and properties of nanoparticles is the use of magnetic nanoparticles in sensors. This technique is based on the change in the response of the nanoparticles to an oscillating magnetic field. When the analyte attaches to a functionalized nanoparticle, the particle's hydrodynamic size increases, causing an increase in the relaxation time, which can be observed using a magnetometer or AC susceptometer.

In the search for monodisperse and non-agglomerated nanoparticles, various methods have been proposed to synthesize nanoparticles, such as coprecipitation, wet-grinding, reverse micelles, and the thermal-decomposition method. In all cases, particles

with diameters less than 50 nm can be obtained but non-agglomerated nanoparticles with a narrow size distribution can only be obtained by methods such as reverse micelles and thermal decomposition.

For many applications, including sensors, the performance of magnetic nanoparticles depends of their intrinsic, single-particle magnetic properties, such as mechanism of response to a time varying magnetic field. For this reason, it is imperative to accurately determine or even model the relaxation mechanism of the magnetic dipoles within the nanoparticles. In doing so, the magnetic anisotropy constant plays a key role because its magnitude typically determines the dominant relaxation mechanism. Techniques such as DC and AC magnetic measurements have been used to determine the anisotropy constant of a great variety of ferrite nanoparticles, obtaining values that are often higher than the bulk material. Unfortunately, the effect of particle-particle interactions is often neglected, hence the reported values may represent an effective collective parameter, rather than an intrinsic property of the nanoparticles.

Cobalt ferrite and magnetite nanoparticles have been synthesized by the thermal decomposition method. The thermal decomposition method produces nanoparticles that are highly crystalline and with a narrow size distribution and which can be suspended in organic solvents. In order to determine appropriate synthesis conditions to obtain cobalt ferrite particles with 10 – 20 nm diameter and a narrow size distribution, a statistical analysis was carried out by varying the temperature and time during the nucleation and growth stages. Transmission electron microscopy was used to determine nanoparticle

diameter and, using a 2^{4-1} experimental design, the impact of synthesis conditions on diameter were determined.

ZFC and AC susceptibility measurements were used to determine the anisotropy constant of samples with several magnetite nanoparticle concentrations. The effect of particle concentration on determination of the anisotropy constant was studied using samples with 0.1%, 1%, and 6%(w/w) fixed in a poly(styrene-divinylbenzene) (PSDVB) matrix. The anisotropy constant was also determined for magnetite nanoparticles with 6, 9, and 11 nm diameter. In this case the samples were prepared at 0.1% (w/w) in PSDVB.

Due to its high anisotropy constant, cobalt ferrite nanoparticles synthesized by thermal decomposition method were used in a sensor application. Biotin-avidin complex was used to demonstrate detection through AC susceptibility measurements. A ligand exchange was necessary to transfer the cobalt ferrite nanoparticle from organic to aqueous phase whereas a biotinylation process was needed to attach the biotin molecule to the nanoparticle surface. Out-of-phase component of dynamic susceptibility dependence on time and frequency of biotinylated nanoparticles was measured before and after contact with avidin. Dynamic light scattering was used to confirm increase of the hydrodynamic diameter caused by avidin attachment to biotinylated nanoparticles.

2. OBJETIVES

Our objective was the development of sample preparation and characterization techniques in order to determine the intrinsic magnetic properties of magnetic nanoparticles. Particularly, we were interested in the anisotropy constant of magnetic nanoparticles. In order to use magnetic particles in sensors based on relaxation time, nanoparticles with a narrow size distribution, diameters between 10-20 nm, high crystallinity, and high anisotropy constant are needed to assure that relaxation is by the Brownian mechanism.

2.1 Specific Objectives

- Synthesize cobalt ferrite nanoparticles with a narrow size distribution, diameter between 10 to 20 nm, with complete incorporation of cobalt in the ferrite structure, and with high crystallinity.
- Characterize the cobalt ferrite nanoparticles using X-ray diffraction, superconducting quantum interference device (SQUID) magnetometry, transmission electron microscopy (TEM), and inductively coupled plasma optical emission spectroscopy (ICP-OES) techniques.
- Determine the effect of sample preparation on determining particle magnetic properties such as the anisotropy constant.
- Study the variation of the anisotropy constant with particle diameter.

- Functionalize cobalt ferrite nanoparticles with biotin and bind avidin molecules to biotinylated cobalt ferrite nanoparticles to demonstrate application in a sensor.

3. BACKGROUND

3.1. Magnetic nanoparticles

3.1.1. Magnetic behaviour

Magnetic materials can be classified based on the change of the magnetization M or magnetic induction B when a magnetic field is applied [3, 4]. When a magnetic field is applied to a material, its magnetic moment increases and can be characterized through the susceptibility χ [5]:

$$\chi = \frac{M}{H} \tag{1}$$

Diamagnetism

Diamagnetism is present when the constituent atoms have zero net magnetic moment. In this case the magnetization is directed opposite to the field and is described by a constant negative susceptibility [5].

Paramagnetism

Paramagnetic materials consist of atoms with a permanent dipole moment. In the absence of an applied magnetic field the dipole moments are randomly oriented (no net magnetization). In the presence of a magnetic field these moments align by rotation in the

direction of the field and the material acquires a net magnetization. Paramagnetic materials are described by a constant positive susceptibility.

Ferro/ferri-magnetism

Ferro or ferri-magnetic materials possess a magnetic moment in the absence of an external field and a very large permanent magnetization [3]. In this case the susceptibility is a multivalued nonlinear function which has saturation and hysteresis.

3.1.2. Ferrofluids

A ferrofluid is a stable colloidal dispersion of magnetic single-domain nanoparticles with diameters under 20 nm. The particles are coated by surfactant/polymer dispersant layers which prevent their agglomeration (Figure 1). The coated particles are suspended in the fluid and undergo rotational and translational Brownian motion [6].

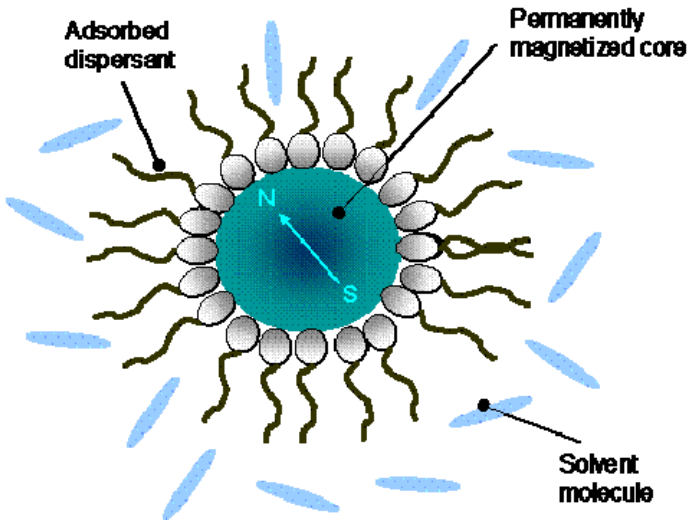

Figure 1: Schematic of magnetic nanoparticles in a ferrofluid

Ferrofluids retain the properties of a fluid even in the presence of high magnetic fields, in which the particles do not separate from the carrier liquid. Additionally, ferrofluids have their surfaces functionalized for specific applications, such as (i) magneto-responsive colloidal extractants [7], (ii) targeted drug delivery vectors [8, 9], (iii) magnetocytolysis agents for treatment of localized cancerous tumors [2, 10], (iv) in magnetic cell sorting schemes [11], and in nanosensors [12]. Various researchers have focused on developing sensors for biological targets, where the nanoparticles are coated with a dispersant bound to an analyte-specific ligand [12, 13].

As mentioned before, ferrofluids are composed of magnetic nanoparticles, usually ferrites such as magnetite, maghemite, cobalt ferrite, and others. Ferrites are electrically insulating ferrimagnetic oxides. Ferrites are widely used in high-frequency applications, because an AC field does not induce undesirable eddy currents in an insulating material [3, 4].

Table 3-1*: Anisotropy constants of some ferrites [15]*

Ferrite	**Anisotropy constant K_1 (erg/cm^3)**
$FeFe_2O_4$*	-1.1×10^5
$Co_{0.8}Fe_{2.2}O_4$	3.9×10^6
$MnFe_2O_4$	-28×10^3
$Co_{0.3}Mn_{0.4}Fe_2O_4$	1.1×10^6

* Reference [16]

Cobalt ferrite, $CoFe_2O_4$, is a cubic ferrite with inverse spinel structure. This ferrite is characterized by having an anisotropy constant higher than other common ferrites (Table 3.1) such as magnetite and maghemite. The anisotropy constant of bulk cobalt ferrite is in the range of 1.8 to 3.0 x 10^6 erg/cm^3 and the saturation magnetization is 80.8 emu/g at room temperature and 93.9 emu/g at 5 K [14].

When magnetic nanoparticles are under an applied magnetic field, the particles tend to align with the field direction either by particle rotation or by dipole moment rotation inside the particle until they achieve their saturation magnetization at high field. This change in magnetization with the applied field can be described by a magnetization curve.

If the field is reduced from saturation, the magnetization curve does not retrace its original path as a result of a decrease of the magnetization at a lower rate (Figure 2). This effect in the magnetization curve is called a hysteresis loop, the area is indicative of the magnetic energy losses during the magnetization process. When the field reaches zero, the magnetic particles remain magnetized because some particles are oriented in the former direction. This residual magnetization is called remancence M_r. To demagnetize the particles (M_r=0), a field with opposite direction must be applied. The magnitude of field required to lower the nanoparticle magnetization to zero is called the coercivity H_c.

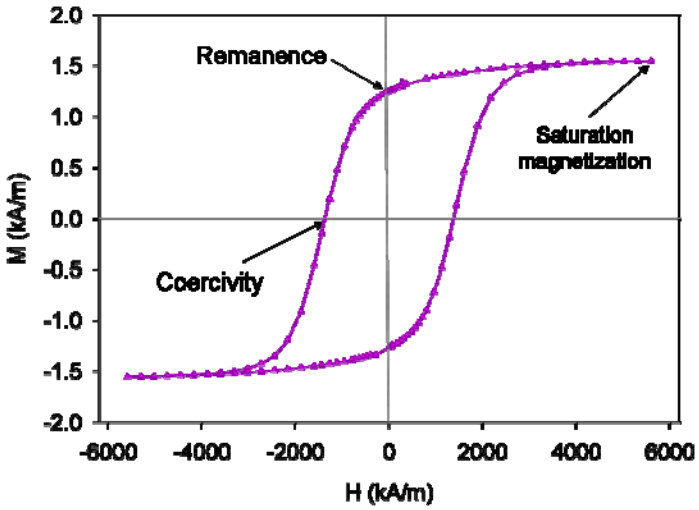

Figure 2: Magnetization curve showing hysteresis, saturation, remanence, and coercivity.

In the case of a ferrofluid or superparamagnetic nanoparticles, the change of magnetization is also described by a magnetization curve. In contrast with ferri/ferro magnetic materials, when the field is reduced from saturation, the magnetization curve retraces its original path; therefore no hysteresis loop is observed and zero values of remanence magnetization and coercivity field are observed. Langevin provided a relation between the net magnetization and the magnetic moments of suspended particles, assuming that magnetic interactions between the particles are negligible

$$\frac{M}{\phi M d} = \frac{\overline{m}}{m} = \coth\alpha - \frac{1}{\alpha} = L(\alpha) \qquad (2)$$

where $L(\alpha)$ is the Langevin function, M_d is the domain magnetization, ϕ is the volume fraction, and $\alpha = \frac{mH}{kT}$ is the ratio between the magnetic and thermal energy, called the Langevin parameter [6].

There are two commonly accepted mechanisms by which the magnetization of a ferrofluid relaxes after the applied magnetic field has changed. In the first mechanism relaxation occurs by particle rotation in the liquid. This particle rotation is due to rotational Brownian motion and is characterized by a Brownian rotational diffusion time τ_B of hydrodynamic origin given by

$$\tau_B = \frac{3V_h\eta_0}{kT} \tag{3}$$

where V_h is the particle hydrodynamic volume and η_0 the viscosity of the carrier liquid. The second relaxation mechanism occurs by magnetic dipole rotation, which has a characteristic time given by the so-called Néel relaxation time

$$\tau_N = \tau_0 \exp\left(\frac{KV}{kT}\right) \tag{4}$$

where τ_0 is assumed to have an approximate value of 10^{-9} s.

When an oscillating magnetic field, $H = H_o \cos(\Omega t)$, is applied to a ferrofluid, the Debye model is considered to describe the dynamic response of the magnetization. The Debye model is obtained by solving the Smoluchowski equation for the orientation distribution function of the magnetic dipole moment considering small values of the Langevin parameter $\alpha \ll 1 (\alpha = mH / k_B T)$ and the mean dipole of the system, $\langle \mu \cos\theta \rangle = \int_0^{\pi} \mu \cos\theta f \sin\theta d\theta$, to obtain the magnetization of the particles

$$M = \chi' H_0 \cos\Omega t + \chi'' H_0 \sin\Omega t \tag{5}$$

where χ' and χ'' are the in-phase and out-of-phase components of the dynamic susceptibility, respectively and are given by

$$\chi' = \frac{\chi_0}{1+\Omega^2\tau^2} \tag{6}$$

and

$$\chi'' = \frac{\chi_0 \Omega\tau}{1+\Omega^2\tau^2}. \tag{7}$$

In equations (6) and (7) χ_0 is the initial susceptibility, Ω is the radian frequency of the applied field, and τ is the relaxation time. The in-phase component χ' gives information about the amount of magnetic flux penetration in the sample [17] whereas the out-of-phase component χ'' is related to energy losses [18, 19].

3.2. Synthesis of nanoparticles by thermal-decomposition method.

Thermal-decomposition is a non-hydrolytic method which produces monodisperse and highly crystalline nanoparticles with diameters between 4 nm to 16 nm. This chemical method separates the nucleation and growth processes, which tend to take place at different temperatures, generating monodisperse particles (Figure 3). In this case a short nucleation phase followed by slow controlled growth are necessary [1, 20].

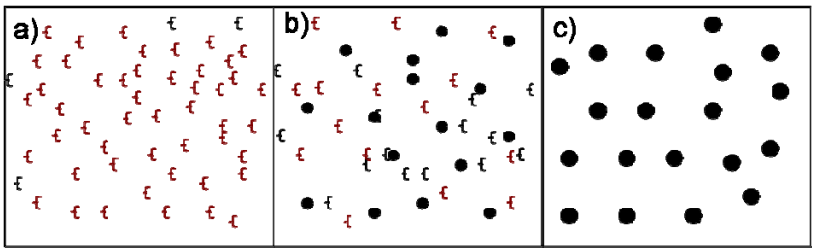

Figure 3: Schematic of particle formation in thermal-decomposition method. After the metals precursors are mixed in organic solvents, the temperature is increased to favor the formation of metal monomers (a). Nuclei start to form when organic solution is saturated with monomers (b). The formation of nuclei stop when the monomer concentration decrease lower of saturation concentration Then, temperature is increased to permit the growth of the nuclei and therefore formation of monodisperse nanoparticles (c).

The thermal-decomposition method permits the control of particle size by regulating the reaction parameters of time, temperature, concentrations of reagents and surfactant, and chain length of the surfactant [1]. The surfactant is absorbed reversiblely to the nanoparticle surface providing a means for mediating growth and imparting useful behavior like stability in solution [21, 22]. It has been observed that the use of two different kinds of surfactants during synthesis produces highly monodisperse nanoparticles. One of the surfactants is bound weakly, such as TOPO, TBP, and amines, to the metal surface permitting rapid growth whereas the other surfactant binds strongly,

such as oleic acid, decreasing the growth rate [22, 23]. As mentioned above, the reaction temperature is an important factor for particle size control because it permits separation of the nucleation and growth phases. At low temperatures, the nucleation phase is favored by generation of more nuclei whereas at higher temperatures the growth phase is favored. At high temperatures smaller particles dissolve and deposit on the larger particles (Ostwald ripening) [1]. The smaller particles possess higher surface free energy which makes them less stable with respect to dissolution in the solvent than larger particles. This stability difference results in a slow diffusion of material from small particles to the surface of large particles [22].

Oleic acid is the most widely used surfactant in nanoparticle synthesis by thermal-decomposition because it produces uniform, spherical, monodisperse nanoparticles and also because it is an excellent stabilizing agent. Furthermore, oleic acid not only acts as an effective steric barrier but also as a mild catalyst [24]. Oleic acid is a monounsaturated fatty acid with formula $C_{18}H_{34}O_2$ ($CH_3(CH_2)_7CH=CH(CH_2)_7COOH$).

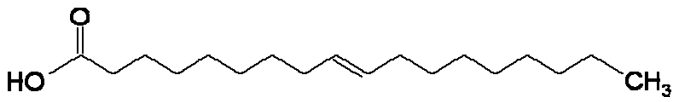

Oleic acid structure

During synthesis, the oleic acid binds so tightly to the particle surface that it impedes particle growth. For this reason in many cases a co-surfactant is used, such as

amines, trialkylphosphines, and others, in order to produce a tight ligand shell which protects the particles from aggregation and oxidation but permits growth [25].

The thermal-decomposition method has been widely used to synthesize spherical and monodisperse nanoparticles with diameters between 4 to 20 nm. Hyeon et al [26] used the thermal-decomposition method to synthesize maghemite nanoparticles with 4, 7, 11, and 16 nm diameter. Iron pentacarbonyl was reacted with oleic acid at 120 ºC in octyl ether to produce an iron oleate complex. Then the mixture was heated to reflux and cooled to room temperature. Trimethylamine oxide was added to the mixture to oxidize the iron particles to maghemite and the solution was heated at reflux. After the solution was cooled to room temperature, ethanol was added to precipitate the nanoparticles, which were redispersed in hexane. In order to obtain different particle sizes, the molar ratio of $Fe(CO)_5$ and oleic acid (Fe/OA) was changed from 1:1, 1:2 and 1:3, resulting in particles of 4, 7, and 11 nm diameter. Particles with diameter of 16 nm were obtained through a seed process, where iron oleate complex was added to a solution of particles of 11 nm and heated to reflux. The electron diffraction and X-ray powder patterns show a material that is highly crystalline in nature and has a structure consistent with maghemite.

Sun et al [27] synthesized Fe_3O_4, $CoFe_2O_4$, and $MnFe_2O_4$ nanoparticles using the thermal-decomposition method. Iron (III) acetylacetonate was used as source of metal ions, oleic acid and oleylamine as surfactants, 1,2-hexadecanediol as oxidizing agent, and phenyl ether or benzyl ether as solvents. All reagents were mixed and heated at 200 ºC. Then heated at reflux and cooled to room temperature. Ethanol was added to precipitate

the nanoparticles which were then re-suspended in hexane. In order to produce MFe_2O_4 (M=Co or Mn) nanoparticles, cobalt (II) acetylacetonate or manganese (II) acetylacetonate was added to the mixture before heating to 200 ºC. Nanoparticles of 4 nm and 6 nm diameter were obtained using phenyl ether (b.p. 259 °C) and benzyl ether (b.p. 298 °C), respectively, as solvents. Nanoparticles of 20 nm diameter were obtained through a seed-mediated growth process. The use of oleic acid together with oleylamine was crucial to formation of nanoparticles. Using only oleic acid, a viscous red-brown product was obtained, which was difficult to purify, whereas using oleylamine only, a lower yield was obtained in comparison to the yield obtained when the two surfactants were used. High resolution TEM imaging showed atomic planes with 2.98 Å interplanar distance, corresponding to (220) planes in the inverse spinel-structured Fe_3O_4. Electron diffraction patterns and XRD confirmed the formation of Fe_3O_4 when $Fe(acac)_3$ was used during synthesis. Magnetic measurements of Fe_3O_4 nanoparticles indicate superparamagnetic behavior at room temperature. At 10 K the particles are ferromagnetic with coercivity of 450 Oe. A Fe:Co and Fe:Mn ratio of 2:1 was obtained by ICP-OES for both cases, confirming the formation of $CoFe_2O_4$ and $MnFe_2O_4$. XRD confirmed the formation of crystalline particles with a cubic spinel structure. Coercivities of 400 Oe at 300K and 20 kOe at 10 K were obtained for $CoFe_2O_4$. Such high coercivity indicates the incorporation of Co cations in the oxide increases the magnetic anisotropy of the materials.

Iron oxide magnetic nanoparticles of sizes smaller than 12 nm and with standard deviations of 15% were obtained by Roca et al [28]. Thermal-decomposition of iron acetylacetonate in phenyl ether and octyl ether was used to obtain these particles.

Particles with mean size of 11 nm were synthesized by mixing the iron oleate complex with oleic acid in octyl ether and heating to reflux, whereas particles of 5.7 nm diameter were synthesized by mixing iron acetylacetonate [$Fe(acac)_3$], 1,2-hexadecanodiol, oleic acid, oleylamine and phenyl ether and heating at 200 ºC for 30 minutes and then heating to reflux. The largest particles present diamond, cubic, and triangular shapes whereas the smaller ones were spherical in shape. XRD spectra show peaks characteristic of planes of magnetite with a lattice parameter of 8.396 Å. Bands at 1625 and 1530 cm^{-1} were observed in FTIR, which were attributed to C-O stretching of oleic acid bound to the nanoparticles. Fe-O stretching of magnetite was also observed at 430 and 610 cm^{-1}. Weight loss with temperature of 25% and 30% were obtained for particles of 5.7 and 11 nm diameter, respectively, which correspond to a monolayer of oleic acid adsorbed on the surface. The nanoparticles exhibited superparamagnetic behavior at room temperature. At 5 K, coercivities of 300 and 175 Oe were obtained for 11 and 5 nm particle diameters.

Manganese ferrite nanocrystals were obtained by thermal-decomposition of Fe-Mn-oleate complex by Kan et al (2004) [29]. The complex was formed from the reaction of iron pentacarbonyl, dimanganese decacarbonyl, and oleic acid in octyl ether at 300 °C. Trimethylamine N-oxide was used to oxidize the resulting alloy nanoparticles to manganese ferrite. The oxidizer was added to the metal-complex at room temperature and then the solution was heated to 140 °C for an hour and then to reflux for an hour. The particles were precipitated by addition of ethanol to the solution at room temperature. TEM images show particles with diameters from 5 nm to 10 nm depending of the oleic

acid/metal precursor's ratio. When oleic acid/metal ratio of 1:1, 2:1, and 3:1 were used, particles of 5, 7, and 10 nm diameter were obtained, respectively. A further increase in the ratio of oleic acid/metal did not result in larger particles but resulted in particles with a broad particle size distribution. XRD showed peaks at 73.58°, 88.46°, and 103.66° and ICP and EDX analysis show a 1:2 molar ratio of Mn to Fe confirming the formation of manganese ferrite nanoparticles.

Park et al (2004) [20] reported the thermal-decomposition process using iron-oleate complex to produce iron oxide nanoparticles with 12 nm diameter. The iron-oleate complex was prepared by mixing iron chloride and sodium oleate in a solution of ethanol/hexane/deionized water and heated to 70 °C for 4 hours. The product was washed with distilled water and the hexane was evaporated. The thermal-decompositon process was done by dissolving the iron-oleate complex and additional oleic acid in octadecene and heating the mixture to 320 °C for 30 minutes. The nanocrystals were precipitated with ethanol and centrifuged. XRD patterns show a cubic spinel structure of magnetite whereas X-ray absorption spectroscopy (XAS) and X-ray magnetic circular dichroism spectroscopy (XMCD) show two phases are formed: γ-Fe_2O_3 and Fe_3O_4. The mechanism of nanoparticle formation was studied using thermogravimetric analysis, differential scanning calorimetry, and FTIR. The results show that nucleation occurs at 200-240 °C, caused by the dissociation of one oleate ligand from the complex with CO_2 elimination, whereas the growth phase occurs at 300 °C, initiated by dissociation of the other two oleate ligands from the iron-oleate complex. Nanoparticles with diameters of 5 nm, 9 nm, 12 nm, 16 nm, and 22 nm could also be synthesized by using the solvents: hexadecane (b.p. 274 °C), octyl ether (b.p. 287 °C), octadecene (b.p. 317 °C), eicosene (b.p. 330 °C),

and tryoctylamine (b.p. 365 °C), respectively. The different particle sizes obtained were attributed to an increase in the reactivity of the iron-oleate complex in the solvent with increase in the boiling point.

Zhang et al (2006) [30] studied the interactions between oleic acid and magnetic nanoparticles when the particles were synthesized by thermal-decomposition. A mixture of $Fe(acac)_2$, 1,2-hexadecanediol, benzyl ether, oleic acid, and oleylamine was heated to 200 °C for 30 min and then heated to 298 °C for 30 min. Particles of 7 nm diameter were obtained after a wash process with ethanol. XRD patterns showed the formation of the Fe_3O_4 crystal structure. FTIR spectra of the nanoparticles show bands at 2922 and 2852 cm^{-1} which were attributed to shifted bands of the asymmetric and symmetric CH_2 stretch. This shift was caused by the field of the solid surface and it is an indication that the hydrocarbon chains that surround the particle were in a closed-packed, crystalline state. Bands characteristic of asymmetric and symmetric COO^- stretch were present (1541 and 1639 cm^{-1}) as was a band at 1050 cm^{-1} characteristic of C-O single bond which demonstrates that oleic acid was chemisorbed onto the nanoparticles as a carboxylate. XPS was also used to prove the binding of the oleic acid onto Fe_3O_4. Peaks at 284.6, 287.4 and 724.1 eV characteristic of C-C in the aliphatic chain, COO^-, and COO-Fe bond respectively, were observed. Two desorption processes were observed by TGA at 260 and 380 °C. This behavior was attributed to oleic acid which may be bonded to iron ions with different state.

3.3. Sensors based on magnetic nanoparticles

There are various proposed sensors based on magnetic nanoparticles in the literature. Some of these sensors take advantage of the hydrodynamic size dependence of the magnetization response of magnetic nanoparticles in solution. The principle of detection consists of specific binding of a magnetic nanoparticle to a targeted analyte, with a resulting change in hydrodynamic radius and hence of magnetic relaxation time. When such binding occurs, an ostensibly measurable change in the magnetization response should result, hence making detection of the analyte possible.

There are several techniques to detect biomolecules using magnetic nanoparticles such as SQUID based sensors, birefringence based sensors, spin-spin relaxation based sensors, among others.

3.3.1. SQUID based sensors

Some researchers have taken advantage of extreme magnetization sensitivity of Superconducting Quantum Interference Device (SQUID) based magnetometers to measure changes in magnetic relaxation time due to binding of magnetic nanoparticles to biomolecules. In the majority of cases, detection is achieved by measuring the decay in the magnetization within an instrument-dependent time window when an external field is applied and then removed. With the applied field the magnetic moments of the particles tend to align resulting in net magnetization.

After switching off the magnetic field, the moments of the magnetic nanoparticles return to equilibrium through the Brownian mechanism.

Kötitz *et al.* (1997) {Kotitz, 1997 #117} used this sensor to detect collagen by measuring the magnetization of nanoparticles of iron oxide coated with dextran and bound, through monoclonal antibodies, with collagen type III. Collagen type III was immobilized on polystyrene tubes with collagen type III antigen absorbed previously onto the surface of the tubes. The tubes were filled with nanoparticle labels and then washed. A remanence measurement was performed with the tubes before and after washing; obtaining same signals in both cases. This indicated that magnetization relaxed by the Neél mechanism because of the immobility of the particles on tube walls. Katsura *et al.* (2001) analyzed the polymorphism of the human genome by DNA chip detection using a high-T_c SQUID. This method involved the modification of one end of the DNA with Biotin so as to immobilize the DNA on the chip and the other end with digoxigenin (DIG) for binding to the magnetic particles. Binding between DIG and magnetic nanoparticles of iron oxide was effected using an anti-DIG antibody. The chip was scanned using the high-T_c SQUID system, obtaining a pattern of magnetic flux agreed with that of the loaded DNA {Katsura, 2001 #118}

3.3.2. Birefrigence based sensors.

The binding of streptavidin and biotin was studied using birefringence measurements by Romanus et al (2002) {Romanus, 2002 #119}, in which case the diameter before and after adding different amounts of human immunoglobulin M

(hIgM) to magnetic particles coated with antibody against hIgM was estimated from the optical response of the suspension. Wilhelm *et al*. (2002) {Wilhelm, 2002 #120} detected linking between magnetic nanoparticles and a biological effector, immnunoglobuline G (IgG), by measuring the size shift of the single nanoparticles to magnetic nanoparticles linked with IgG. Maghemite nanoparticles coated with DMSA were combined with different amounts of IgG and birefringence measurements showed a change in the relaxation time as the available IgG amount per particle increased. The hydrodynamic diameter was determined using equation (5). The diameter of the DMSA-coated maghemite particles was 34.7 nm. When the IgG was added, the calculated diameter was observed to increase too, demonstrating binding between DMSA-coated magnetic nanoparticles and IgG.

3.3.3. Spin-spin relaxation based sensors.

Magnetic nanoparticles can self-assembly to formed larger nanoassemblies. In this process, the magnetic nanoparticles are considered as magnetic relaxation switches due to enhanced of spin-spin relaxation times caused by higher efficiency at dephasing the spins of surrounding water protons. Based on spin-spin relaxation times measurements using a nuclear magnetic resonance, Perez et al. {Perez, 2002 #76} sense different types of reversible molecular interactions. Superparamagnetic colloidal iron oxide core coated with aminated dextran and coupled with 12-bp thiolated oligonucleotides was used to sense complementary oligonucleotides. After hybridization of magnetic particles with a target, these formed

clusters resulted in decreased in the spin-spin relaxation times of near water molecules. Also, Peter et al. sensed enzymatic activity through increase of relaxation time using nanoparticles coupled with avidin incubated with DEVD peptides to recognize caspase 3 enzyme.

3.3.4. AC susceptibility based on sensors

It is possible to measure binding or immobilization of magnetic nanoparticles through changes in the magnetic relaxation time after a magnetic field has been applied, known as Magnetorelaxometry. Magnetization decay in small free nanoparticles is due to Brownian relaxation where the time constant (equation 3) increases with increasing hydrodynamic volume V_h, as when an analyte binds to the nanoparticles. The Néel time constant does not change as it only depends on the magnetic volume V_p and so is independent of binding to the magnetic nanoparticles. If the particles attach to a solid phase, their motion is inhibited and magnetization decay is due to Néel relaxation [31].

Connolly *et al.* (2001) [32] proposed AC susceptibility measurements for detection of biomolecules in aqueous solution. For a suspension of magnetic particles whose hydrodynamic radius increases from 75 nm to 76 nm with binding of a biomolecule they calculated a shift in the peak of χ'' of 10 Hz. They also calculated the frequency-dependent susceptibility for mixtures of particles with different size distribution observing two peaks as a result of different relaxation times of the two distributions. Chung *et al*. (2005) [33] used avidin coated magnetite nanoparticles to

detect S-protein. When biotinylated S-protein was added to the coated nanoparticles, the peak frequency of χ'' decreases from 210 to 120 Hz. A 60 nm hydrodynamic radius was determined using equation (3) and (7) after adding S-protein while TEM measurements, before addition indicated 50 nm diameter. This increase in the hydrodynamic size confirms the binding between S-protein and magnetic nanoparticles. Fornara et al (2008) [34] used AC susceptibility measurements to detect Brucella antibodies. Magnetite nanoparticles of ~ 20 nm were synthesized by hydrolysis of chelate metal alkoxide complexes at high temperature in solutions of a chelating alcohol. Magnetite nanoparticles were functionalized with lipopolysaccarides by adsorption through van der Waals interactions. LPS-magnetite nanoparticles were added to solutions with and without Brucella antibodies and AC measurements were done. A shift of the out-of-phase component of dynamic susceptibility curve peak from 50 kHz to 20 Hz was observed in the sample with antibodies. This shift of the out-of-phase component peak indicates that the hydrodynamic diameter of the particles increased from 20 to ~260 nm due to attachment of the antibodies. No shift in the out-of-phase component was observed in the sample without antibodies.

3.3.5. Sensors based on sensors magnetic nanoparticles

Halbreich et al (1998) [83] synthesized maghemite nanoparticles by the coprecipitation method. Nanoparticles were functionalized with dimercaptosuccinic acid which gives stability to the nanoparticles at physiological pH and ionic conditions (0.15M NaCl at pH 7.4). Additionally, DMSA permits binding of effectors directly to the

particle surface. Recombinant human annexin V was bound to nanoparticles through DMSA and used to characterize phospholipid distribution in cellular membranes, particularly phosphatidylserine (PS), on mouse red blood cells. PS exposure on the cell surface is associated with blood coagulation and apoptosis. Magnetic cell sorting and magnetic separation were used to determine PS exposure. Annexin-nanoparticles were incubated with red blood cells. Then, a magnetic field gradient was applied to the sample and magnetic cell sorting revealed from retained magnetic nanoparticles the PS exposure. Any detectable annexin-nanoparticles binding to red blood cells was observed in freshly collected mouse blood whereas after 24 hours of incubation, 10 % of the cells bound annexin-nanoparticles. DMSA-maghemite nanoparticle were also used for magnetocytolisis of THP1 cells and macrophages. In this case, DMSA-maghemite nanoparticles were bound to THP1 human monocytic cells through S-S bridges. Then, an oscillating magnetic field (0.01 T at 1 MHz) was applied and an increase in temperature caused by energy dissipation was observed. Cell death was evident 3-6 hours after 10 min incubation in the magnetic field.

DMSA-nanoparticles were also used by Huh et al (2005) [84] for detection of cancer cells using magnetic resonance. Magnetite nanoparticles with 9 nm diameter were synthesized by the thermal-decompositon method. Then, a phase transfer reaction was performed by mixing magnetite nanoparticles with a large excess of DMSA for 24 hours, obtaining stable aqueous solutions. This high stability in aqueous media and high monodispersity permitted the use of DMSA-magnetite for cancer diagnosis by functionalization with cancer-targeting antibody. Herceptin was used as targeting antibody due to high specific binding to the HER2/neu receptor overexpressed in breast

cancer cells. Herceptin was bound to DMSA-magnetite nanoparticles through sulfo-SMCC (Sulfosuccinimidyl 4-(maleimidomethyl)cyclohexane-1-carboxylate) cross-linking procedure. In vitro binding specificity and efficiency studies were done using weighted spin-echo images. No change was observed when non-functionalized nanoparticles were used. In contrast when herceptin-magnetite nanoparticles were used a significant darkening of MR image was observed. This change in the MR images indicated selective binding of the functionalized nanoparticles to the cancer cells. The relationship between MR signals and the binding activity of herceptin nanoparticles was also studied by using different levels of HER2/neu receptor. An increase in the HER2/neu expression resulted in a darker MR signal which revealed an excellent specific binding efficiency of herceptin-magnetite nanoparticles.

Josephson et al (1999) [85] functionalized iron oxide nanoparticles with a peptide sequence from the HIV-tat protein to improve intracellular magnetic labeling of different cells. Superparamagnetic dextran iron oxide nanoparticles were synthesized and functionalized with fluorescent tat peptide. The fluorescent peptide was attached to nanoparticle through an amine group present in dextran iron oxide nanoparticles using N-succinimidyl-3-(2-pyridyldithio)propionate (SPDP). Three cell types were tested: murine lymphocytes, human natural killer cells, and HeLa cells. Increased cellular uptake of tat-peptide-nanoparticles was observed in the three cases. When tat-peptide nanoparticles were used, an uptake about 100 fold higher was obtained in comparison when non-funtionalized nanoparticles were used. Fluorescence microscopy showed the tat-peptide nanoparticles were distributed in the cytoplasm with particularly high concentrations in the nucleus and nucleolus. Relatively homogenous distribution was observed which

indicates no lysosoma accumulation was obtained in contrast when endocytosis pathways are used for cell labeling.

4. EFFECT OF REACTION TEMPERATURE AND TIME ON $CoFe_2O_4$ OBTAINED THROUGH THE THERMAL-DECOMPOSITION METHOD

A statistical design of experiments was used to study the effect of reaction temperature and time on the synthesis of cobalt ferrite nanoparticles by the thermal-decomposition method. A 2^{4-2} factorial experimental design with two central points was used in which the control variables were the time and temperature of the nucleation and growth stages. Transmission electron microscopy, X-ray diffraction, inductively coupled plasma optical emission spectroscopy, and magnetic measurements were used for particle characterization. Cobalt-substituted ferrite ($Co_xFe_{3-x}O_4$) nanoparticles with diameters between 9 nm to 13 nm were obtained by varying the nucleation temperature between 150 ºC and 250 ºC, the growth temperature between 300 ºC and 330 ºC, and the time in each stage between 60 min and 120 min. Statistical analysis showed that only the temperatures had an influence on the final particle size. The analysis of variance indicates that increasing the nucleation temperature resulted in decreased particle size whereas increasing the temperature in the growth stage resulted in an increase in particle size. Additionally, statistical analysis showed that the growth temperature had an effect on Fe/Co ratio. An increase in the growth temperature produces a decrease in the Fe/Co ratio. Finally, a statistically significant correlation was found between particle diameter

and saturation magnetization at 5 K and 300 K. No correlation was found between diameter and other magnetic properties.

The synthesis of uniform, nanometer sized, and non-agglomerated particles of transition metal oxides has been the goal of several studies. This great interest in metal oxide materials is due to their magnetic, ferroelectric, superconducting, and electronic properties [1]. Various methods have been proposed to synthesize nanoparticles such as coprecipitation [35], wet-grinding [36], reverse micelles [37], and the thermal-decomposition method [38]. In most cases, particles with diameters less than 50 nm are obtained, but non-agglomerated nanoparticles are usually only obtained by methods such as reverse micelles and thermodecomposition. The thermodecomposition method has the advantage of producing particles with high crystallinity. The high temperatures used in the thermodecomposition method provide the energy necessary to arrange the atoms in the crystal, resulting in a highly crystalline structure.

Some studies have focused on control of particle size by regulating reaction parameters such as time, temperature, and surfactant and reagent concentrations [1, 21, 39-43]. The effect of surfactant on shape and particle diameter has been reported [24, 44-46]. Yu et al (2004) studied the effect of oleic acid concentration. Keeping the time of reaction at 60 minutes and using OA/Fe ratios of 3.2, 6 and 8, magnetite nanocrystals with average diameter of 7, 20 and 28 nm were obtained. When an OA/Fe = 10 was used no nanocrystals were formed because excess of OA inhibited nuclei formation. The increase in diameter with increasing OA/Fe ratio was attributed to lower monomer

reactivity. With increasing ligand concentration less nuclei were formed resulting in larger nanoparticles because there was more precursor available in the solution. Similar behavior was observed by Kang et al (2004) [29]. Kang et al synthesized manganese ferrite nanoparticles by thermal decomposition of Fe-Mn oleate complex in octyl ether at ~ 300 ºC then oxidized using trimethylamine N-oxide. OA/Fe ratio was varied from 1 to 3 producing particles with diameters from 5 nm to 10 nm. For OA/Fe ratio higher than 3, larger particles sizes were not obtained. Instead, a broad size distribution was obtained. X-ray diffraction, electron diffraction, and X-ray spectroscopy confirmed the formation of crystalline manganese ferrite particles. The temperature dependence of magnetization was measured. An increase in blocking temperature from 30 K to 85 K was observed with increasing particle diameter from 5 to 10 nm. This increase in the blocking temperature was attributed to an increase in the magnetic anisotropy energy.

Teng et al (2004) [47] synthesized magnetite nanoparticles in octyl ether at 275 ºC for 60 minutes using iron pentacarbonyl as metal precursor. OA/Fe ratios between 1 and 4 were used. Teng et al observed formation of polydisperse nanoparticles when a ratio of OA/Fe < 2 was used. This polydispersity was attributed to low concentration of OA which does not stabilize the nanoparticles. For ratios of OA/Fe > 3 monodisperse nanoparticles were obtained where OA/Fe = 3 was considered to be the lower limit to synthesize monodisperse nanoparticles. Using an OA/Fe ratio of 3, magnetite nanoparticles were also synthesized in octyl ether at 275 ºC varying the reaction time from 60 to 150 min 10, 16, and 25 nm particles were obtained when the reaction time was 60, 90, and 150 min, respectively. The increase in diameter was ascribed to Ostwald ripening - small particles dissolve during the prolonged reaction time and deposit on large

ones. For a reaction time of 3 hours, polydisperse particles with 35 nm diameter were obtained. Yin et al [24] studied the influence of molar ratio of oleic acid to Fe atoms on the particle size of maghemite. A mixture of $Fe(CO)_5$, trioctylamine, and oleic acid was heated under nitrogen atmosphere to obtain a black solution. The solution was kept at this temperature for an hour and then it was cooled to room temperature and trimethylamine N-oxide was added. The mixture was heated to 350 °C for one hour. When a molar ratio of $Fe(CO)_5$/oleic acid of 1 was used, the decomposition temperature was 265 °C and particles of 4 nm diameter were synthesized. This small particle size was attributed to the fast nucleation rate (there was not enough surfactant to arrest isolated iron atoms). When the ratio was increased to 2, the decomposition temperature increases to 280 ° and 7 nm diameter particles were obtained with a broad size distribution. Upon increasing the Fe/oleic acid ratio to 3, uniform and spherical particles with 11 nm diameter were obtained.

Shukla et al [44] investigated the effect of surfactant on the shape and size of cobalt nanoparticles. Cobalt nanoparticles were synthesized by thermal-decomposition of cobalt octacarbonyl in diclorobenzene using several surfactants. A mixture of two surfactants in diclorobenzene was heated to 150 ºC then a cobalt octacarbonyl diclorobenzene solution was added. The mixture was heated to reflux for 30 min. Initially, octadecylamine (ODA) was used as primary surfactant whereas trioctylphosphine oxide (TOPO) and tridodecylamine (TDDA) were used as secondary surfactants. Spherical nanoparticles (10 nm) were obtained when TOPO was used as surfactant whereas hexagonal particles and wide size distributions were obtained when using TDDA. In a second experiment, TOPO was used as primary surfactant whereas

ODA and didoceylamine (DDA) were used as secondary surfactants. Spherical particles of 10 nm were obtained in both cases. Yin et al (2004) [24] synthesized γ-Fe_2O_3 nanoparticles using different surfactants: oleic acid, lauric acid, and octanoic acid. In this case, a mixture of $Fe(CO)_5$, trioctylamine, and the surfactant was heated under nitrogen atmosphere until the solution was black. The solution was kept at this temperature for an hour and then it was cooled to room temperature and trimethylamine N-oxide was added. The mixture was heated to 350 °C for one hour. Ethanol was used to precipitate the nanoparticles. Particles with 6, 9, and 12 nm diameter were obtained using as surfactants octanoic acid, lauric acid, and oleic acid, respectively. The difference in size was attributed to the length of the carbon chain, the greater the length of the carbon chain, the greater the decomposition temperature (dt), producing larger particles (octanoic dt = 264 ºC, lauric acid dt = 280 ºC, and oleic acid dt = 288 ºC). When a surfactant with short chain length such as butyric acid was used, the decomposition temperature decreased to 205 ºC and particles were not formed. Particles with 20 nm diameter were obtained without surfactant whereas the decomposition temperature increases to 360 ºC. These results indicate that the surfactant not only prevents particle agglomeration but it also acts as catalyst. Longer carbon chains for the surfactant diminish its effect as a catalyst.

A literature review of the effect of organic solvent and several surfactants on particles diameter is showed in Table 4-1 whereas a literature review of the effect of oleic acid and iron ratio on particle diameter is showed in Table 4-2.

Table 4-1: Literature review of the effect of organic solvents and several surfactants on particle diameter

	Particles	Reactives	Parameter	Results
Xie et al (2006)	Fe_3O_4	$Fe(acac)_3$ Oleic acid Oleylamine Hexadecanediol	Phenylether (259ºC) Benzylether (298ºC) Octadecene (310ºC)	4 nm 6 nm 12 nm
Sun et al (2004)	Fe_3O_4 $CoFe_2O_4$ $MnFe_2O_4$	$M(acac)_x$ Hexadecanediol Oleic acid	Phenyl ether Benzyl ether	4 nm 6 nm
Park et al (2004)	Fe_3O_4	$Fe(Cl)_3$ Oleci acid	Hexadecene (274ºC) Octyl ether (287ºC) Octadecene (310ºC) Eicosene (330ºC) tryoctylamine (365ºC)	5 nm 9 nm 12 nm 16 nm 22 nm
Shukla et al (2006)	Co	$Co(CO)_8$ Diclorobenzene	ODA/TOPO ODA/TDDA TOPO/DDA	10nm-spherical High lns-hexagonal 10nm-spherical
Yin et al (2004)	Fe_2O_3	Octyl ether $Fe(CO)_5$ trioctylamine	Oleic acid Lauric acid Octanoic acid Butyric acid Without surfactant	12 nm 9 nm 6 nm No particles 20 nm

As mentioned above, the reaction temperature is an important factor for particle size control because it permits separation of the nucleation and growth phases. It has been argued that using high temperatures during the nucleation phase favors the generation of more nuclei. On the other hand, high temperatures during the growth phase cause smaller particles to dissolve and deposit on to larger particles (Ostwald ripening) [1]. Based on

these arguments it is expected that high temperatures in the nucleation phase result in smaller particles, whereas high temperatures in the growth phase result in larger particles.

Table 4-2: Literature review of the effect of oleic acid and iron ratio on particle diameter

	Particles	Reactive	Parameter	Results
Hyeon et al (2002)	Fe_2O_3	Octyl ether $Fe(CO)_5$ Oleic acid	1<OA/Fe<3	4<d<11 nm
Yu et al (2004)	Fe_3O_4	Octadecene FeO(OH) Oleic acid	35min<tg<65min 65<tg<120min 3<OA/Fe<8 OA/Fe=10	6<d<9 nm Higher ln □ 7<d<28 nm No particles
Kang et al (2004)	$MnFe_2O_4$	Octyl ether Fe-Mn oleate Oleic acid	1<OA/Fe<3 OA/Fe>3	5<d<10 nm Higher ln σ
Teng et al (2004)	Fe_3O_4	Octyl ether $Fe(CO)_5$ Oleic acid	1<OA/Fe<4	OA/Fe=3 limit to narrow size distribution
Yin et al (2004)	Fe_2O_3	Octyl ether $Fe(COO)_5$ Oleic acid	1<OA/Fe<3	4<d<7 nm

The effect of temperature on particle size was studied by Xie et al [48]. Magnetite nanoparticles were synthesized by mixing iron (III) acetylacetonate, oleic acid, oleylamine, and hexadecanediol in an organic solvent. The mixture was heated to 200 ºC for 2 hours and then heated to reflux for 1 hour. When phenyl ether (b.p. 259 ºC) was used as solvent, nanoparticles with diameters of 4 nm were synthesized whereas using benzyl ether (298 ºC) or octadecene (310 ºC), diameters of 6 nm and 12 nm were obtained. The increase in particle size with increasing boiling point of the organic solvent revealed that high reaction temperature during the growth stage facilitated the formation

of large nanoparticles. Magnetization curves were obtained and saturation magnetization over 74 emu/g and superparamagnetism behavior was observed.

Yu et al (2004) [39] varied the reaction time during the thermal-decomposition process of iron (III) oxide hydrate (FeO(OH)) to synthesize magnetite nanoparticles. Iron oxide was mixed with oleic acid and octadecene. Then, the mixture was heated at 320 ºC for 35, 45, and 65 minutes obtaining particles with 6.4, 7.7, and 9 nm diameter, respectively. When longer periods (60-120 min) were used they obtained similar diameter but wide size distribution, which was attributed to Oswald ripening.

Based on results presented in the literature to obtain particles with a determined diameter and narrow size distribution, we made modifications (organic solvent, reaction temperature, and reaction time) to the thermal-decomposition method reported by Sun et al [27] to obtain cobalt ferrite particles with 10 nm – 20 nm diameter and narrow size distribution. Oleic acid and oleylamine were used as surfactants and to control shape and particle diameter. Octadecene was used as solvent due to its high boiling point, which permits synthesizing particles with larger diameter (~ 12 nm to ~ 20 nm). A ratio of OA/Fe of 3 was used in all syntheses in order to promote the formation of spherical nanoparticles with a narrow size distribution. In this work, the temperatures and times during nucleation and growth stages were varied. A statistical design of experiments was used to quantitatively assess the effect of these variables on particle diameter, size distribution, lattice parameter, Fe/Co ratio, and magnetic properties. Particles were characterized with respect to size and morphology by TEM, crystallinity by XRD, composition by ICP-OES, and magnetic properties by SQUID magnetometry.

4.1. Materials

Metals : Iron (III) acetylacetonate ($Fe(C_5H_7O_2)_3$, 99.9 % metal basis form Sigma Aldrich), and Cobalt (II) acetylacetonate ($Co(C_5H_7O_2)_2$, 97% pure from Sigma Aldrich); Surfactants: Oleic acid ($CH_3(CH_2)_7CH=CH(CH_2)_7COOH$, 99% pure from Sigma Aldrich), Oleylamine ($CH_3(CH_2)_7CH=CH(CH_2)_7CH_2NH_2$, >70 % GC from Sigma Aldrich); Organic Solvents: Hexane ($CH_3(CH_2)_4CH_3$, reagent grade from Sigma Aldrich); octadecene ($CH_3(CH_2)_{15}CH=CH_2$ from Fluka), Ethanol (CH_3CH_2OH, 99% pure from Aldrich); Chloroform ($CHCl_3$, 99% pure from Fisher.

4.2. Synthesis procedure

Cobal ferrite nanoparticles were synthesized by the thermal-decomposition method. Iron (III) acetylacetonate (0.067 M) and cobalt (II) acetylacetonate (0.034 M) were added to an octadecene solution, with 0.3 M oleic acid and 0.3 M oleylamine. The mixture was heated at a rate of 12.5 °C/min up to the nucleation temperature and was kept at this temperature for a specified time period. Then, the mixture was heated at a rate of 3.5 °C/min up to the growth temperature (Figure 4).

A 2^{4-1} experiment was used to study the effect of synthesis conditions on the nanoparticles properties. The independent variables were the temperature and time of the nucleation and growth phases whereas the particle diameter, lattice parameter, and Fe/Co

ratio were the dependent variables. Using the MINITAB® program, random runs were obtained (see Table 4-3).

After synthesis, the solution was cooled and a wash process with ethanol and chloroform was carried out. Initially, ethanol was added to the solution and the nanoparticles were precipitated by centrifugation (8000 rpm for 20 min). The precipitate was re-suspended in chloroform to dissolve the free oleic acid and ethanol and centrifugation was used again to precipitate the nanoparticles. This wash process was repeated three times in order to eliminate free oleic acid. The nanoparticles were dried in a vacuum oven at 80 °C.

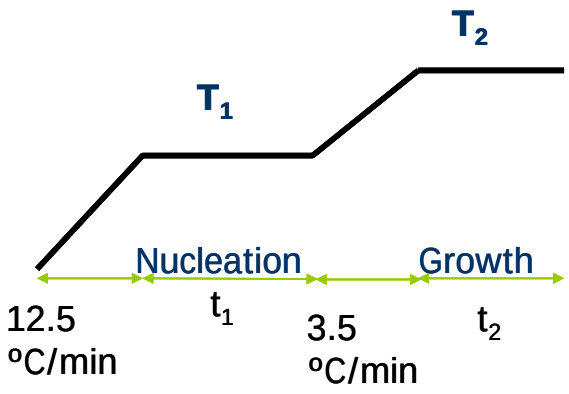

Figure 4: Schematic of thermal-decomposition synthesis procedure using a ramp and soak.

A fractional experiment was used to observe the impact of temperature and time during the nucleation and growth stages on the particle size. A 2^{4-1} experiment was done because of the cost to produce a full factorial experiment. In the case of a full factorial 16 runs are needed whereas with a fractional experiment the number of runs is reduced to 8. Two central points were used in 2^{4-1} experiment in order to verify the curvature of the data. Considering as independent variables the temperature and time in the two stages,

random runs were obtained for the 2^{4-1} experiment. The low and high levels used for the nucleation temperature were 150 ºC and 250 ºC respectively, whereas in the growth stages 300 ºC was used as a low level and 330 ºC as a high level. In both stages, the low and high levels used in the time variable were 60 and 120 minutes, respectively (Table 4-3).

Table 4-3: Random runs of synthesis of cobalt ferrite nanoparticles by thermal-decomposition method.

Run	T_1(°C)	t_1(min)	T_2(°C)	t_2(min)
1	250	120	300	60
2	250	120	330	120
3	150	120	300	120
4	200	90	315	90
5	150	120	330	60
6	250	60	330	60
7	200	90	315	90
8	250	60	300	120
9	150	60	330	120
10	150	60	300	60

4.3. Characterization

Morphology of the particles was characterized using a Zeiss 922 200 kV Transmission Electron Microscope. Samples were prepared by suspending the dry nanoparticles in hexane and sonicating for 10 minutes. An ultrathin carbon grid was submerged in the solution. The grid was placed on filter paper to absorb the excess solvent and dried at room temperature to promote the slow evaporation of the solvent and

obtain a uniform deposition of nanoparticles on the grid. Then the grid was placed in a vacuum oven at 80 ºC to assure the complete evaporation of the solvent. Crystallographic analysis was done in a Rigaku Ultima II X-ray diffractometer. The ratio of Fe/Co was determined using a Perkin Elmer Optima 2000 DV inductively coupled plasma optical emission spectrometer. The sample was prepared by dissolving the dry particles in a solution at 2%(v/v) of HNO_3. Organic mass fraction in the dry sample was determined by thermogravimetric analysis using a TA Instruments Q-2950 TGA. Fourier Transform Infrared spectra were obtained in a Varian 800 FT-IR. Magnetic properties were measured using a Quantum Design MPMS XL-7 SQUID magnetometer. Samples were prepared by suspending the nanoparticles in a paraffin matrix. The paraffin was melted and then the nanoparticles were added and mixed. The oleic acid coated nanoparticles readily disperse in liquid paraffin. The mixtures were added to a capsule and permitted to cool to room temperature. Magnetization curves were obtained at 300 K and 5 K with up to 7 Tesla fields.

4.4. Results

Figure 5 shows some representative TEM images of cobalt ferrite nanoparticles synthesized by thermodecompositon. In this case, TEM images of cobalt ferrite nanoparticles synthesized under the extremes of synthesis conditions tested are shown. Un-agglomerated nanoparticles were obtained for all synthesis conditions (see Appendix A1). Using the imageJ program, the diameter of 300 particles was measured and fitted to

a log-normal distribution to obtain the average diameter and geometric deviation for each synthesis condition**.**

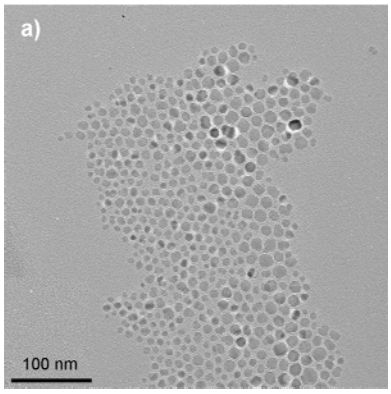

T_1=150 °C t_1=120 min T_2= 300 °C t_2=120 min

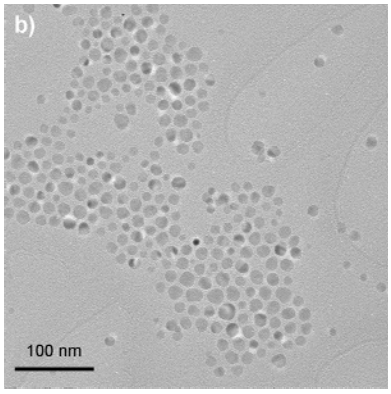

T_1=150 °C t_1=120 min T_2= 330 °C t_2=60 min

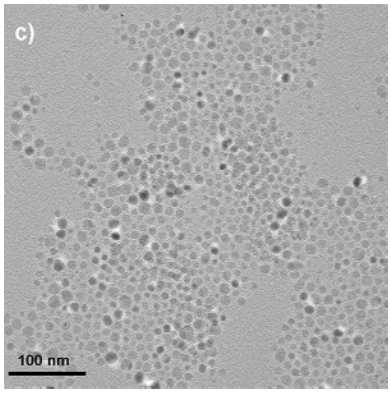

T_1=250 °C t_1=60 min T_2= 330 °C t_2=60 min

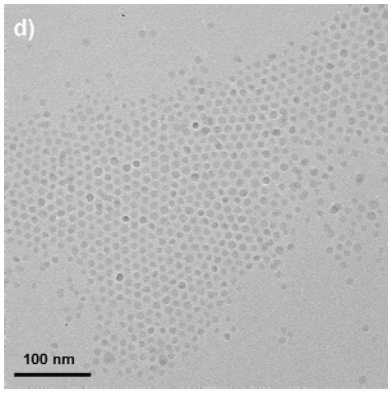

T_1=250 °C t_1=60 min T_2= 300 °C t_2=120 min

Figure 5: TEM images of cobalt ferrite particles synthesized by thermal-decomposition method at nucleation (T_1) and growth (T_2) temperature and nucleation (t_1) and growth (t_2) time.

Table 4-4 shows the results. Geometric deviations less than 0.25 were obtained, which confirm that the thermal-decomposition method produces nanoparticles with a narrow size distribution. The mean diameter and geometric deviation obtained using a log normal distribution were processed using the MINITAB® program.

Table 4-4: Physical characteristics of $Co_xFe_{3-x}O_4$ nanoparticles synthesized by the thermal-decomposition method.

	$CoFe_2O_4$			
Run	D_{TEM}	Ln σ	a(Å)	Fe/Co (atomic)
1	10.61	0.24	8.39	2.87
2	10.72	0.19	8.43	1.97
3	11.03	0.23	8.40	2.78
4	11.92	0.20	8.41	2.51
5	13.03	0.20	8.40	1.75
6	10.01	0.25	8.36	2.06
7	12.32	0.24	8.36	2.67
8	8.75	0.12	8.33	1.47
9	13.16	0.21	8.40	1.39
10	11.48	0.12	8.38	2.83

Initial results (Table 4-6) showed that temperature and time during the synthesis process did not have a statistically significant impact (p-value > 0.18) on size distribution. When particle size was the answer variable (Table 4-6) an impact of the nucleation temperature was observed (p-value = 0.059); whereas the reaction time in both stages did not have a statistically significant impact (p-value > 0.24) on the answer variable. Also, the normal probability plot of residuals (Figure 6) indicated that the sample data do not possess normal behavior, therefore an analysis of variance could not be used. For this reason, a simpler analysis was used for which the experiment was collapsed. In this case, only the temperature in each stage was considered as the independent variable, resulting in a full factorial 2^2 design, with replica and two central points. The analysis of variance results are shown in Table 4-7.

Table 4-5: Statistical analysis of 2^{4-1} experiment considering size distribution as answer variable.

Term	Effect	Coeff	T	P
Constant		0.1949	16.38	0.039
T_1	0.0124	0.0062	0.52	0.694
t_1	0.0393	0.0196	1.65	0.346
T_2	0.0368	0.0184	1.55	0.622
t_2	-0.0161	-0.0080	-0.68	0.805
T_1*t_1	-0.0079	-0.0038	-0.32	0.866
T_1*T_2	-0.0051	-0.0025	-0.21	0.182
T_1*t_2	-0.0811	-0.041	-3.41	0.510

R^2(adj) = 53.97%

Table 4-6: Statistical analysis of 2^{4-1} experiment considering particle diameter as answer variable.

Term	Effect	Coeff	T	P
Constant		11.099	110.99	0.006
T_1	-2.152	-1.076	-10.76	0.059
t_1	0.497	0.249	2.49	0.243
T_2	1.263	0.631	6.31	0.100
t_2	-0.367	-0.184	-1.84	0.317
T_1*t_1	-0.788	0.394	3.94	0.158
T_1*T_2	-0.578	-0.289	-2.89	0.212
T_1*t_2	-0.207	-0.104	-1.04	0.488

R^2(adj) = 95.8%

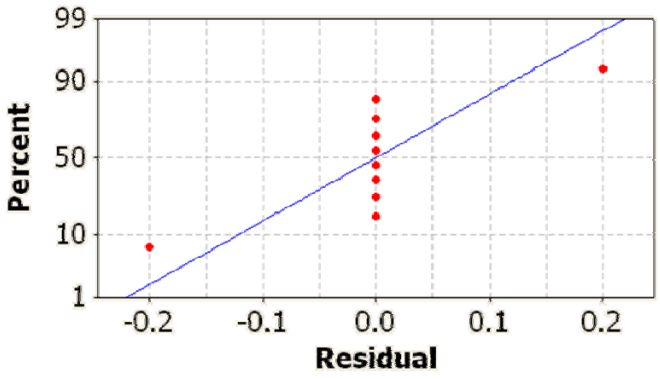

Figure 6: Normal probability plot of residuals for the 2^{4-1} experiment.

With a 95% confidence level we can conclude that the nucleation and growth temperature had an impact on the particle size with p-values of 0.006 and 0.042, respectively. The nucleation temperature had a negative impact, which means that an increase in temperature promotes a decrease in particle diameter. This is consistent with the argument that at low temperatures fewer nuclei are formed and therefore more precursors are available in the solution for particle growth. On the other hand, the growth temperature had a positive impact, which means that high growth temperature results in an increase in the diameter of the particles. In Figure 7, the normal probability distribution of residuals is shown.

Table 4-7: Statistical analysis of 2^2 experiment.

Term	Effect	Coeff	T	P
Constant		11.099	47.63	0.000
T_1	-2.152	-1.076	-4.62	0.006
T_2	1.262	0.631	2.71	0.042
T_1*T_2	-0.578	-0.289	-1.24	0.270

R^2(adj) = 76.96%

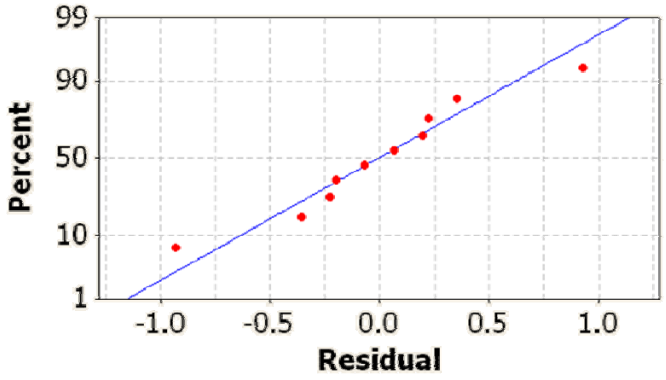

Figure 7: Normal probability plot of residuals for the 2^2 experiment.

A representative electron diffraction patterns is show in Figure 8. In all cases, well defined rings which are an indication that the nanoparticles are crystalline. Interplanar spacing and plane indexes of the different crystallographic planes were difficult to determine due to high brightness of the pictures caused by oleic acid on the surface of the nanoparticles.

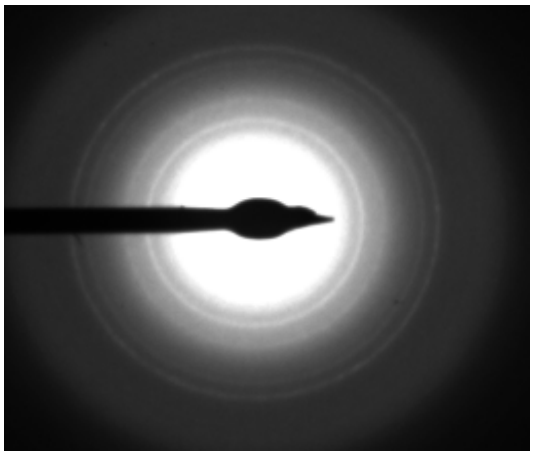

Figure 8: Electron diffraction of cobalt ferrite nanoparticles synthesized by thermal-decomposition method T_N=250 C, t_N=120 min., T_G=330 C, t_G=120 min.

Figure 9 shows a representative x-ray diffraction pattern of the cobalt ferrite nanoparticles synthesized under the same synthesis conditions as in Figure 5. In some samples (i.e. Figure 9d) significant background was observed which is due to oleic acid present in the samples. All peaks characteristic of the inverse spinel crystalline structure can be observed. Similar patterns were obtained for all synthesis conditions (see Appendix A.2). Bragg's law was used to determine the lattice parameter *a* of the particles. The values obtained are shown inAll peaks characteristic of the inverse spinel crystalline structure can be observed. Similar patterns were obtained for all synthesis conditions. Bragg's law was used to determine the lattice parameter *a* of the particles.

The values obtained are shown in Table 4-4. The lattice parameters *a* found for all samples are near the values reported for bulk cobalt ferrite (*a*=8.39 Å). The lattice parameter was statistically analyzed using a fractional experiment. Results showed that temperature and time did not have a statistically significant impact (p-value > 0.37) on lattice parameter (Table 4-8).

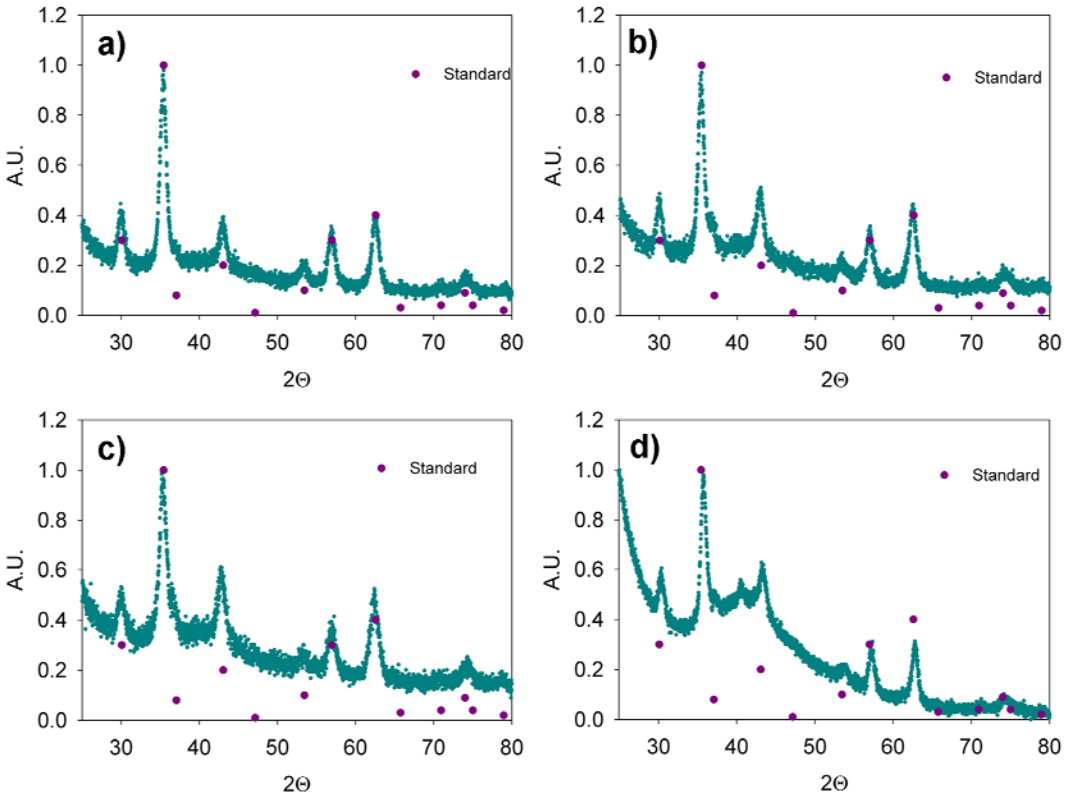

Figure 9: X-ray diffraction patterns of cobalt ferrite nanoparticles synthesized by the thermal-decomposition method. Synthesis conditions: a) T_1=150 °C t_1=120 min T_2= 300 °C t_2=120 min; b) T_1=150 °C t_1=120 min T_2= 330 °C t_2=60 min; c) T_1=250 °C t_1=60 min T_2= 330 °C t_2=60 min; and d) T_1=250 °C t_1=60 min T_2= 300 °C t_2=120 min.

Elemental analysis confirmed the incorporation of cobalt ions in the structure of the ferrite for all synthesis conditions. Although the metal precursor ratio (Fe/Co) was 2,

the synthesized particles presented different Fe/Co ratio (see Table 4-4) which is an indication of formation of cobalt-substituted ferrites ($Co_xFe_{3-x}O_4$, $0.77 < x < 1.25$).

Table 4-8: Statistical analysis of 2^{4-1} experiment considering lattice parameter as answer variable.

Term	Effect	Coeff	T	P
Constant		8.3863	670.9	0.001
T_1	-0.0175	-0.0088	-0.7	0.611
t_1	0.0375	0.0188	1.5	0.374
T_2	0.0225	0.0113	0.9	0.533
t_2	0.0075	0.0038	0.3	0.814
T_1*t_1	0.0275	0.0138	1.1	0.470
T_1*T_2	0.0125	-0.0063	0.5	0.705
T_1*t_2	-0.0025	-0.0012	-0.1	0.937

$R^2(adj) = 0.00\%$

The Fe/Co ratio was analyzed statistically. Considering 95% confidence, initial results (Table 4-9) showed there was no impact of temperature and time during thermal-decomposition (p-value > 0.077) on the Fe/Co ratio. Collapsing the experiment (Table 4-10) and considering only the temperatures as independent variables, the growth temperature apparently has an impact (p-value = 0.099) on Fe/Co ratio. A statistical analysis was carried out between Fe/Co ratio and lattice parameter and diameter and lattice parameter. No correlation was observed between Fe/Co ratio and lattice parameter (p-value > 0.73) neither between diameter and lattice parameter (p-value > 0.34) (see appendix A.4).

FTIR spectra (Figure 10a) showed bands characteristic of oleic acid. Bands at 2920, 2851 and 1465 cm^{-1} characteristic of the CH_2 chains present in the oleic acid were

observed [37]. A low intensity broad band at 1637 cm^{-1} was observed which was attributed to C-O vibration. Compared to the band at ~1710 cm^{-1} of free oleic acid, the appearance of this band at low frequency is an indication of the bound oleic acid [28].The band at 1710 cm^{-1} characteristic of free oleic acid was small, which is an indication that the amount of free oleic acid present in the sample is negligible.

Table 4-9**:** Statistical analysis of 2^{4-1} experiment considering Fe/Co as answer variable

Term	Effect	Coeff	T	P
Constant		2.123	53.06	0.012
T_1	-0.060	-0.030	-0.75	0.590
t_1	0.440	0.220	5.50	0.114
T_2	-0.660	-0.330	-8.25	0.077
t_2	-0.440	-0.220	-5.50	0.114
T_1*t_1	0.215	0.108	2.69	0.227
T_1*T_2	0.505	0.253	6.31	0.100
T_1*t_2	-0.305	-0.153	5.23	0.120

R^2(adj) = 96.89%

Table 4-10**:** Statistical analysis of 2^2 experiment considering Fe/Co as answer variable.

Term	Effect	Coeff	T	P
Constant		2.123	0.163	0.000
T_1	-0.060	-0.030	-0.18	0.861
T_2	-0.660	-0.330	-2.02	0.099
T_1*T_2	0.505	0.253	1.55	0.256

R^2(adj) = 31.58%

In order to reduce the amount of oleic acid in the sample, the sample was subjected to an additional washing process with ethanol and chloroform (two additional cycles). FTIR spectra (Figure 10b) showed a decrease in the band at 1710 cm^{-1} but the

band's intensity in the range of 2900 to 2800 cm^{-1} was the same. This observation indicates that an additional wash process only decreases the amount of free oleic acid but it does not decrease the oleic acid bound to the surface of the nanoparticles. TGA results confirm this affirmation. A decrease in the peak intensity at ~ 200 ºC, corresponding to free oleic acid, was observed whereas at ~ 400 K, corresponding to oleic acid bound to particle surface, no change in the peak intensity was observed.

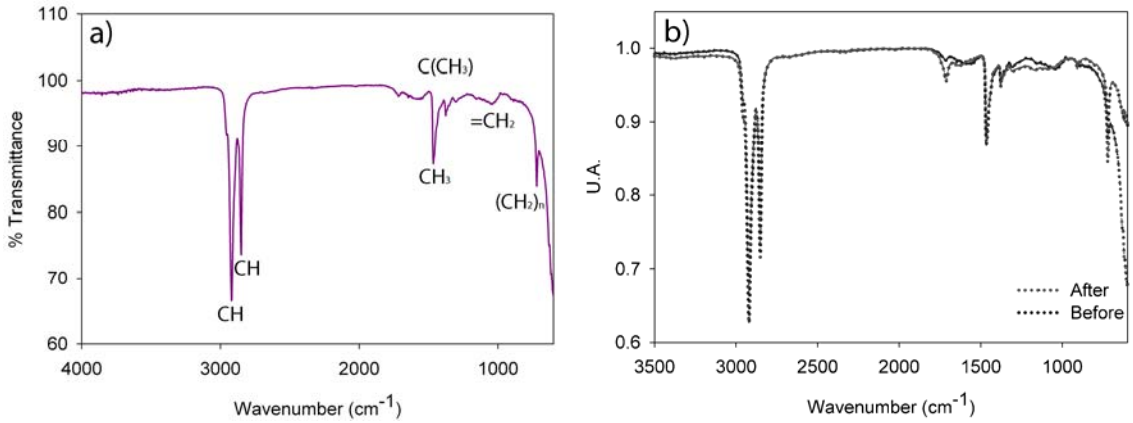

Figure 10: FTIR spectrum of cobalt ferrite nanoparticles synthesized by thermal-decomposition: a) synthesis condition T_1=250 °C, t_1=60 min., T_2=300 °C, and t_2=120 min, b) before and after of additional washing process with ethanol and chloroform.

Magnetization curves at 5 K and 300 K were measured (see representative example in Figure 11), obtaining in all cases hysteresis at 5 K (Appendix A.3) with coercivities and remanence as high as 23 kOe and 108 emu/$g_{ferrite}$, respectively, which are characteristic of single domain particles. The high coercivities confirmed the incorporation of Co ions into ferrite structure. At 300 K only three of the samples presented coercivity in the range of 0.3 – 0.1 kOe (Table 4-11). Due to high organic percentage (> 93%) presented in some samples, it is possible that the particles were not

completely fixed in the paraffin matrix, therefore the particles relaxed also by Brownian mechanism as a consequence no coercivity was observed.

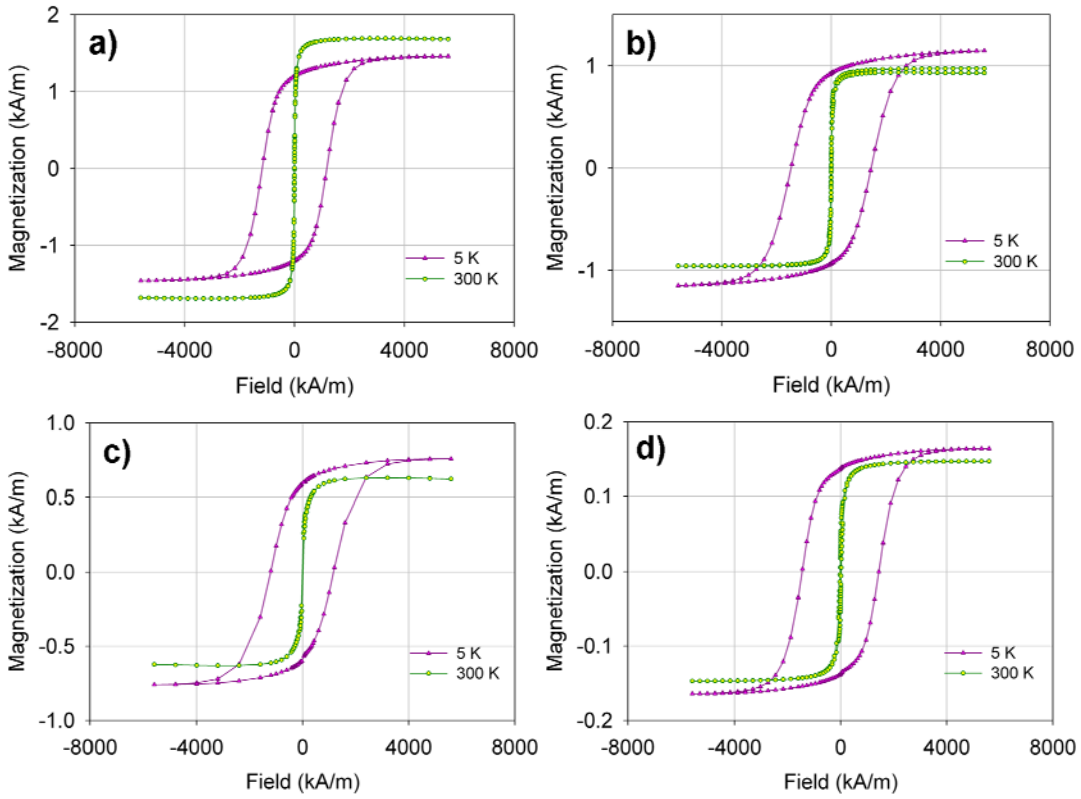

Figure 11: Magnetization curves for cobalt-substituted ferrite synthesized by thermodecomposition. Synthesis conditions: a) T_1=150 °C t_1=120 min T_2= 300 °C t_2=120 min; b) T_1=150 °C t_1=120 min T_2= 330 °C t_2=60 min; c) T_1=250 °C t_1=60 min T_2= 330 °C t_2=60 min; and d) T_1=250 °C t_1=60 min T_2= 300 °C t_2=120 min.

Reduced remanent magnetization values near those of bulk $CoFe_2O_4$ (M_r/M_s[0 K] = 0.83) were obtained for almost all samples which is an indication that the synthesized particles possess positive cubic anisotropy, characteristic of cobalt ferrite. For the sample from run 7, a value of Mr/Ms ≈ 0.5 was obtained. This is an indication that particles are non-interacting uniaxial single domains [14].

Table 4-11: Magnetic properties of cobalt-substituted ferrite nanoparticles synthesized by thermal-decomposition.

	5 K				300 K		
Run	M_s ($emu/g_{ferrite}$)	M_r ($emu/g_{ferrite}$)	H_c (KOe)	M_r/M_s	M_s ($emu/g_{ferrite}$)	M_r ($emu/g_{ferrite}$)	H_c (KOe)
1	111.4	91.7	17.7	0.82	92.4	0.8	0.0
2	120.3	94.7	17.3	0.79	100.9	3.4	0.0
3	91.3	72.5	14.6	0.79	106.3	0.9	0.0
4	98.3	77.4	14.3	0.79	83.7	19.8	0.3
5	125.1	108.9	18.2	0.87	113.7	5.0	0.0
6	53.4	43.1	15.3	0.81	44.8	4.3	0.1
7	42.3	22.9	3.5	0.54	42.4	15.7	0.0
8	106.3	87.5	23.0	0.82	87.5	25.0	0.3
9	88.9	75.7	17.5	0.85	85.6	18.1	0.1
10	151.0	128.9	12.3	0.84	132.6	2.6	0.0
Bulk	90.0			0.83*	80.3		

* Extrapolated to 0 K

Statistical analysis was also considered having as answer variable the magnetic properties of the cobalt-substitued ferrite nanoparticles synthesized by thermal-decomposition (see appendix A.4). No correlation was found between synthesis conditions and magnetic properties (saturation magnetization, coercivity, remanence and reduced remanence) . Considering a 2^{4-1} factorial, p-values higher than 0.13 were obtained whereas using a 2^2 factorial p-values higher than 0.17 were obtained. When a regression was considered using as independent variable particle diameter, a relation with saturation magnetization at 5 K and 300 K was observed (see Table 4-12 and Table 4-13). In both cases a positive effect was observed which means that increasing the particle size

increases the saturation magnetization. This increase in saturation magnetization with increasing diameter is expected because of the decrease in surface/volume ratio and therefore of the contribution of the so-called "magnetically dead layer". A regression analysis between Fe/Co ratio and lattice parameter and magnetic properties was carried out. P-values higher than 0.3 were obtained which indicates that there is no correlation between Fe/Co and lattice parameter and the magnetic properties.

Table 4-12**:** Regression between particle diameter and saturation magnetization at 5 K.

Term	Coeff	T	P
Constant	4.05	0.09	0.932
Diameter	8.14	2.23	0.061

R^2(adj) = 33.10%

Table 4-13**:** Regression between particle diameter and saturation magnetization at 300 K.

Term	Coeff	T	P
Constant	11.10	0.26	0.804
Diameter	6.69	1.95	0.092

R^2(adj) = 26.10%

4.5. Conclusions

Cobalt-substituted ferrite nanoparticles with diameters between 9 and 13 nm were synthesized by the thermodecomposition of metal (Fe, Co) acetylacetonate in octadecene, in presence of oleic acid and oleylamine. The use of oleic acid and oleylamine as surfactants permitted formation of non-agglomerated and narrowly dispersed ($\ln \sigma < 0.25$) nanoparticles. Statistical analysis showed, with 95 % confidence, that the

temperature during the nucleation and growth stages had an effect on diameter. The nucleation temperature had a negative effect whereas the growth temperature had a positive effect. This indicates that smaller size particles can be obtained with higher nucleation temperature and lower growth temperature. In contrast, when a low temperature is used during the nucleation stage and a high temperature during the growth stage larger particles can be formed. Statistically, no effects of reaction times (60 – 120 min) on diameter were observed which indicates that 60 minutes of reaction time was enough time to complete formation and growth of nuclei. The statistical analysis also showed with 95% confidence that temperature and time during thermodecomposition method had no an effect on size distribution, lattice parameter, and Fe/Co ratio. At 90% confidence, the growth temperature had a negative impact on the Fe/Co ratio, indicating that higher temperatures promote incorporation of Co into the crystal structure. The use of octadecene as solvent permitted synthesizing nanoparticles at high temperatures. This high temperature favored the formation of highly crystalline cobalt-substituted ferrite with inverse spinel structure and positive cubic anisotropy. Magnetization measurements at 5 K showed high coercivities, most higher than 10 kOe, which indicates incorporation of cobalt ions into the ferrite structure. The factorial analysis did not show any correlation between synthesis conditions and magnetic properties but the regression analysis showed that increasing particle diameter increases the saturation magnetization. The regression analysis also showed no correlation between Fe/Co ratio and lattice parameter and magnetic properties.

5. EFFECT OF SAMPLE CONCENTRATION ON THE DETERMINATION OF ANISOTROPY CONSTANT OF MAGNETIC NANOPARTICLES

Techniques such as equilibrium (DC) and dynamic (AC) magnetic measurements have been used to determine the anisotropy constant of a variety of magnetic nanoparticles, obtaining values that are often an order of magnitude higher than the corresponding bulk material. Unfortunately, the effect of particle-particle interactions is often neglected, hence the reported values are an effective collective parameter, rather than an intrinsic property. In this study DC and AC magnetic measurements are used to determine the anisotropy constant of magnetic nanoparticles fixed in a cross-linked polymer matrix. Nanoparticle concentrations of 0.1%, 1%, 6% and 33%(w/w) were used in order to determine the effect of concentration, and hence interactions, on the value determined for the anisotropy constant. The effect of interaction on determining the magnetocrystalline anisotropy constant was accounted for by using the Néel and Vogel-Fulcher relaxation models, the latter with an effective interaction temperature determined from independent measurements. A decrease in the anisotropy constant determined from these measurements was observed with decreasing particle concentration from ~6100 kerg/cm^3 to ~500 kerg/cm^3 using the Vogel-Fulcher model and from ~9100 kerg/cm^3 to ~1100 kerg/cm^3 using the Néel model. The values obtained for the most dilute samples using the Vogel-Fulcher model are of comparable magnitude to bulk values for magnetite. More importantly, the value of τ_0 obtained from AC susceptibility decreased

from 10^{-32} to 10^{-9} s with decreasing particle concentration. As τ_0 is expected to be of the order of 10^{-9} s, these results indicate that the value of magnetic anisotropy determined for the dilute sample represents an intrinsic rather than effective property. These measurements and analysis illustrate the importance of particle concentration/interactions in determining the intrinsic magnetic properties of nanoparticles, particularly the anisotropy constant.

In the past decade, magnetic nanoparticles have attracted great interest in areas such as engineering, chemistry and medicine, due to their interesting electrical, optical, magnetic, and chemical properties which are distinct from those of the bulk material. Magnetic nanoparticles have been used for separation processes [7, 49, 50], in catalyst recovery [51, 52], in heat-exchange [53, 54], in cancer treatment [55, 56], and in sensors [12, 33, 57, 58], among other applications. The performance of magnetic nanoparticles in many of these applications depends on the intrinsic properties of the nanopartocules, such as saturation magnetization and mechanism of response to time varying magnetic fields.

As one example of an application with strict requirements on the magnetic properties of nanoparticles, the use of magnetic nanoparticles in sensors has attracted great interest as it allows the analysis of samples without a cleaning or separation step due to the fact that the detection mechanism is based on changes in the response of the nanoparticles to an oscillating magnetic field. When the analyte attaches to a functionalized nanoparticle, the particle's hydrodynamic size increases, causing an increase in the relaxation time which can be observed using a magnetometer or AC

susceptometer [13, 33, 34]. As a mention in the chapter 3 there are two characteristic magnetic relaxation mechanisms of colloidal non-interacting magnetic particles: Brownian relaxation (τ_B equation (3)) and Néel relaxation (τ_N equation (4)). When $\tau_N \ll \tau_B$ relaxation occurs through the Néel mechanism, whereas if $\tau_N \gg \tau_B$ relaxation occurs through the Brownian mechanism. In most suspensions of magnetic nanoparticles, both relaxation processes are present and the mechanism with the shorter time is expected to dominate, resulting in an effective relaxation time. If the nanoparticles are fixed in a solid matrix, only the Néel mechanism is effective. The relaxation times given by equation (3) and (4) are strictly for the case of infinitely dilute systems with no particle-particle interactions. Because only τ_B depends on the particle hydrodynamic diameter it is clear that sensor applications require particles with $\tau_N >> \tau_B$ and hence with high values of K.

Equation (4) is strictly valid only collections of non-interacting dipoles. Most samples of magnetic nanoparticles, especially those used for magnetic measurements, have short particle-particle separation distances which result in magnetic dipole-dipole interactions between particles. In the case of particles with weak magnetic interactions, Shtrikman and Wolhlfarth [59] proposed the Vogel-Fulcher law to describe the temperature dependence of the characteristic time for Néel relaxation

$$\tau_{VF} = \tau_0 \exp\left(\frac{KV_m}{k(T - T_0)}\right) \tag{8}$$

where T_0 is the interaction temperature parameter, a measure of the interparticle interaction strength. For temperatures above T_0 the thermal energy dominates, while below T_0 the interaction energy governs the relaxation process [60].

In determining the magnetic properties of nanoparticles one is usually forced to make measurements in samples consisting of a collection of vast number of particles. Because magnetic interactions clearly affect the collective response of the nanoparticles one must realize that even when a given model appears to fit the observed response the properties determined from the measurements may in fact be "apparent" or "effective" properties. In order to determine the intrinsic properties of the nanoparticles one must either suppress particle-particle interactions or somehow accounts for them during data analysis.

In order to use magnetic nanoparticles in sensors based on relaxation time, it is very important to know the mechanism by which the nanoparticles relax. One way to determine the relaxation mechanism is through the intrinsic anisotropy constant value.

The anisotropy constant can be determined by magnetic measurements such as zero-field-cooled (ZFC) magnetization curves and AC susceptibility measurements, in samples wherein magnetic relaxation is through the Néel mechanism. In a zero-field-cooled measurement, the sample is cooled to a desired temperature, then a magnetic field is applied and the magnetization of the sample is measured as the temperature increases. As the temperature increases the ZFC magnetization of the sample increases up to

maximum. The temperature at which this maximum occurs is referred to as the blocking temperature, T_B. Above the blocking temperature, the thermal energy is larger than the magnetic energy barrier, and the ZFC magnetization decreases with increasing temperature. At the peak of the ZFC curve, some authors [16, 26, 61, 62] assume that the Néel relaxation time is comparable to the time scale of the measurement τ_{obs} and therefore, using equation (4), the anisotropy constant can be determined by

$$K = \frac{k_B (T_B - T_0)}{V} \ln\left(\frac{\tau_{obs}}{\tau_0}\right) \tag{9}$$

The result corresponding to equation (4) can be obtained by setting $T_0 = 0$. It must be noted that using equation (9) to estimate the anisotropy constant requires independent knowledge of T_0, τ_{obs}, and τ_0. For τ_{obs} a value of 100 s is assumed and for τ_0 a value of 10^{-9}s. Many authors neglect T_0 as they do not determine it independently. Furthermore in using equation (9) the applied magnetic field must be small, as equation (3) and (4) are strictly valid at the limit of small fields.

In the case of AC susceptibility measurements, the in-phase component of the AC susceptibility χ' is measured as a function of temperature at various frequencies. The curve of in-phase component curve as a function of temperature usually presents a peak which shifts with frequency. The variation of this peak with applied frequency can be used to estimate the magnetic anisotropy. It is commonly assumed that the peak of the χ' vs. T curve corresponds to the condition $\Omega\tau = 1$, hence plotting $\ln(1/\Omega)$ vs. $1/T$ should

yield a linear relation in which the slope provides an estimate for *KV*. Using the Vogel-Fulcher model one obtains

$$\ln \frac{1}{\Omega} = \ln \tau_0 + \frac{KV}{k(T - T_0)} \tag{10}$$

Note that in order to account for interactions in equation (10) an independent valur for T_0 is needed. Again, the result for the Néel model, equation (4), can be obtained by setting $T_0 = 0$. One advantage of using equation (10) to estimate K is that the value of τ_0 can also be obtained from the infinite temperature intercept. Few authors report values for τ_0 estimated in this way, even when they use the equation (10) to estimate K. Many of those who do report τ_0 obtain values in the range of 10^{-16}-10^{-20} s, which are too small to be considered physically valid. This would indicate that the assumptions of equation (10) do not apply for the sample, which implies that the value of the anisotropy constant from equation (10) is an apparent value and not truly an intrinsic property of the nanoparticles. As noted above, T_0 is needed in order to apply equations (9) and (10). The interaction temperature parameter T_0 can be independently determined through low field magnetization curves, measured at different temperatures. At low field, the particle magnetization is described by an initial susceptibility χ_0 given by

$$\chi_i = \frac{A}{T - T_0} \tag{11}$$

When equation (11) applies a plot of $1/\chi_0$ vs. T yields a straight line whose intercept with the $1/\chi_0$ axis contains the interaction temperature parameter T_0.

Several studies on the effect of particle-particle interactions on magnetic properties, such as saturation magnetization, reduced magnetization, and blocking temperature for nanoparticles of Co [63], magnetite [64, 65], Fe-C [66], maghemite [67], and cobalt and manganese ferrites have been done[68]. However, a systematic study of the effect of particle-particle interactions on the value of the magnetic anisotropy constant determined from such measurements has not been reported. Previous studies have estimated the anisotropy constant of magnetite [16, 69] and cobalt ferrite [70-72] nanoparticles dispersed in paraffin or high boiling point solvents. AC susceptibility and DC magnetization measurements have shown an increase in the magnetic relaxation time with increasing particle concentration [65, 67]. However, physically unrealistic values of the characteristic time τ_0 ($10^{-29}<\tau_0<10^{-19}$ s) have been obtained using the in-phase component of the dynamic susceptibility and the Néel model [73-75]. A literature review of the effect of particle concentration on magnetic properties of nanoparticles is shown in Table 5-2.

Here, we report the effect of particle-particle interactions on ZFC, FC, and AC susceptibility curves and especially on the anisotropy constant determined from these measurements for magnetic nanoparticles. In this case magnetite nanoparticles were used as probes due to cobalt-substituted ferrite obtained by thermal-decomposition method (Chapter 4) presented high barrier energy (see Appendix B.1).

Table 5-1: Literature review of the effect of particle concentration on magnetic properties of nanoparticles

	Particles	Property	K_{ZFC} (erg/cm^3)	K_{AC} (erg/cm^3)
Luo et al (1991)	Fe_3O_4 fixed in oil (T_f=210K)	T_B increase with increasing [particle]		
Jonsson et al (1995)	Fe_2O_3fixed in solvent (T_f=180K)	χ', χ'', and ZFC peaks shift to higher T with increasing [particle]		
Held et al (2001)	Co fixed in paraffin	M_S increase with increasing [particle]		
Vestal et al (2004)	$CoFe_2O_4$ and $MnFe_2O_4$ fixed in eicosane	T_B increase with increasing [particle], M_r/M_S		
Hanh et al (2003)	$CoFe_2O_4$ fixed in epoxy			$5x10^7$
Lin et al (2006)	Fe oxide		$3\text{-}8\ x10^5$	
Baldi et al (2007)	$Co_xFe_{3-x}O_4$ fixed in paraffin			1.5 MJ/m^3 $\tau_0=10^{-20}$ s
Tackett et al (2008)	$Co_xFe_{3-x}O_4$ fixed in epoxy		$2\text{-}5x10^5$	$4\text{-}10x10^5$ $10^{-19}<\tau_0<10^{-29}$ s

This high barrier energy did not permit observed the transition from ferromagnetic to superparamagnetic in the temperature range studied (4 K – 400 K) therefore not peak was observed in ZFC and AC susceptibility curves. Measurements were performed in a temperature range of 4 – 400 K with the nanoparticles fixed in a poly(styrene-divinylbenzene) (PSDVB) matrix. Because the glass transition temperature of PSDVB is higher than 400 K, the relaxation mechanism for the entire temperature

range accessible in our instrument was the Néel mechanism. Our results show how these measurements can be combined in order to determine the intrinsic values of τ_0 and K for magnetic nanoparticles.

5.1. Materials

Iron (III) acetylacetonate ($Fe(C_5H_7O_2)_3$, 99.9 % metal basis), was obtained from Sigma Aldrich and used as metal precursor; Oleic acid ($CH_3(CH_2)_7CH=CH(CH_2)_7COOH$, 99% pure) and Oleylamine ($CH_3(CH_2)_7CH=CH(CH_2)_7CH_2NH_2$, >70 % GC) from Sigma Aldrich were used as surfactants; 1,2-hexadecanediol ($CH_3(CH_2)_{13}CHOHCH_2OH$, 90% from Sigma Aldrich) was used as oxidizing agent. Solvents used were octadecene ($CH_3(CH_2)_{15}CH=CH_2$ from Fluka), hexane ($CH_3(CH_2)_4CH_3$, reagent grade from Sigma Aldrich), ethanol (CH_3CH_2OH, 99% pure from Aldrich), and Chloroform ($CHCl_3$, 99% pure from Fisher).

5.2. Synthesis procedure

Magnetite nanoparticles were synthesized by the thermal-decomposition method, by adding iron (III) acetylacetonate, at a concentration of 0.1 M, to an octadecene solution with 0.3 M oleic acid, 0.3 M oleylamine, and 0.3 M 1,2-hexadecanediol. The mixture was heated at a rate of 12.5 °C/min to 200 ºC and was kept at this temperature

for 90 minutes. Then the mixture was heated at a rate of 3.5 °C/min to 315 ºC, and kept at 315 ºC for 90 minutes. After synthesis, the solution was cooled and washed with ethanol and chloroform. Initially, ethanol was added to the solution and particles were precipitated by centrifugation for 20 min at 8000 rpm. The precipitate was re-suspended in chloroform to separate the free oleic acid. Ethanol and centrifugation were used again to precipitate the nanoparticles. The precipitate was suspended in hexane by ultrasonication. The solution was centrifuged to 2000 rpm for 10 minutes to precipitate the un-suspended nanoparticles. The precipitate was dried in a vacuum oven at 80 °C.

5.3. Characterization

Morphology of the particles was characterized using a Zeiss 922 200 kV Transmission Electron Microscope. Samples were prepared by suspending the dry nanoparticles in hexane and sonicating for 10 minutes. An ultrathin carbon grid was submerged in the solution. The grid was placed on filter paper to absorb the excess solvent and dried at room temperature to promote the slow evaporation of the solvent and obtain a uniform deposition of nanoparticles on the grid. Then the grid was placed in a vacuum oven at 80 ºC to assure the complete evaporation of the solvent. Crystallographic analysis was done in a Rigaku Ultima II X-ray diffractometer. Thermogravimetric analysis was done in a Q-2950 TGA from TA Instruments.

To study the effect of particle-particle magnetic interactions on magnetic properties determined from DC and AC measurements, the nanoparticles were fixed in a solid matrix of poly(styrene-divinylbencene). Nanoparticles were suspended in a solution of styrene with 15%(v/v) of DVB and 0.37%(w/w) of azobisisobutyronitrile (AIBN). Various amounts of magnetite were added to the solution to obtain concentrations of 6%, 1%, and 0.1% (w/w). The mixtures were heated at 70 ºC until polymerization was complete.

To assure that the matrix used to fix the magnetic nanoparticles was solid at all temperatures used, differential scanning calorimetry (DSC) was done using a TA instruments Q20 DSC. The sample with particles was first heated to 473 K and slowly cooled to room temperature. Then the DSC curve was obtained by heating the sample at a rate of 10 K/min to 473 K.

Magnetic properties were measured using a Quantum Design MPMS XL-7 SQUID magnetometer. Zero field cooled curves were obtained by cooling the sample under zero applied field to 4 K, then applying a field of 10 Oe and warming the sample to 400 K taking magnetization measurements at regular intervals. Field cooled curves were obtained by cooling the sample from 400 K to 4 K under the applied field, taking magnetization measurements at regular intervals. Magnetization curves were obtained at 4 K, 300 K, and 400 K with up to 7 Tesla fields. Also, magnetization curves were obtained at low field (± 20 Oe) for temperatures between 4 and 400 K. The AC susceptibility of the samples was measured as a function of temperature using a 4 Oe drive amplitude and a frequency range of 1 to 1000 Hz.

5.4. Results

TEM showed that non-agglomerated nanoparticles were obtained (Figure 12). Using the imageJ program, the diameter of 300 particles was measured and fitted to a log-normal distribution with an average diameter of 8.5 nm and geometric deviation of 0.15, indicating that the sample has a very narrow particle size distribution.

X-ray diffraction showed that the nanoparticles synthesized are highly crystalline, Figure 13. The presence of several peaks characteristic of the inverse spinel structure confirmed the formation of a ferrite (Figure 13). A lattice parameter of a = 8.38 Å was found, which is comparable with that of bulk magnetite (a=8.39 Å).

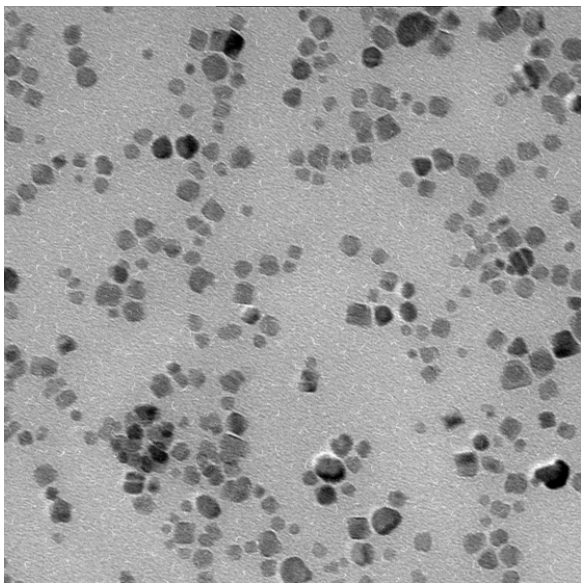

Figure 12: TEM of magnetite nanoparticles synthesized by the thermal-decomposition method and used to prepare all samples.

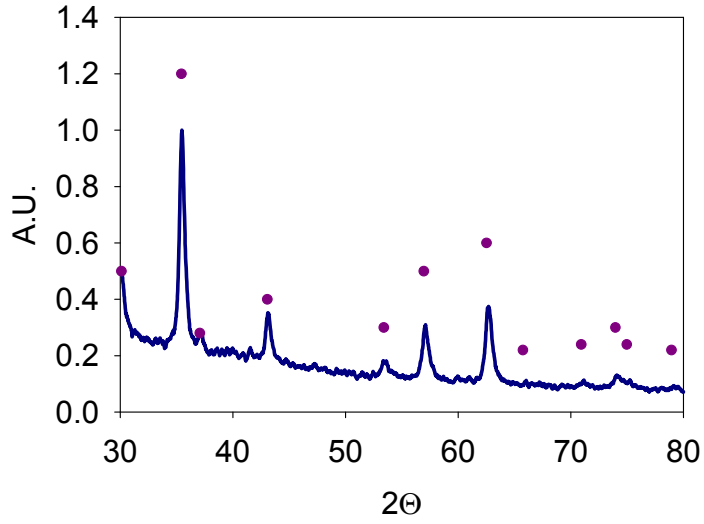

Figure 13: X-ray diffraction pattern of magnetite nanoparticles used to prepare all composite samples. Dots represent peak positions for an inverse spinel crystal structure.

According to TGA, 67% (w/w) of the sample was found to be organic material (Figure 13). Thermo gravimetric analysis showed large drops in sample mass at ~200 ºC (16.3%w/w) and ~400 ºC (41.4%w/w) which were attributed to free oleic acid and oleic acid bound to the surface of the nanoparticles, respectively. The iron oxide cores correspond to 33%(w/w) of the samples. Based on this percentage of Fe_3O_4 the samples fixed in PSDVB with different concentrations were prepared.

The DSC curve for PSDVB (see Appendix B.2) showed no transitions up to 473 K, which indicates that the polymer chains are rigid and therefore the particles fixed in the matrix would not physically rotate during the magnetic measurements. The use of polystyrene-DVB as matrix provides the opportunity of measuring magnetic properties at temperatures as high as 473 K, but the upper limit of our SQUID magnetometer is 400 K.

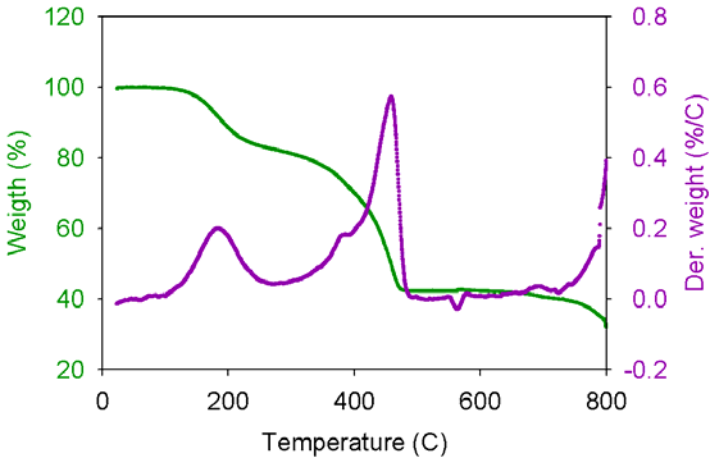

Figure 14: Thermogravimetric analysis of magnetite nanoparticles synthesized by thermal-decomposition

Coercivity, remanence, and saturation magnetization were obtained from magnetization curves at 4 K, 300 K, and 400 K (Figure 15) and are summarized in Table 5-3. At 4 K the coercivity was unaffected by particle concentration whereas the saturation magnetization and remanence were strongly influenced. At 300 K and 400 K the values obtained for coercivity and remanence were less 4 emu/gFe_3O_4 and 15 Oe. The saturation magnetization at 300 K and 400 K was found to decrease with increasing particle concentration. The observed decrease in saturation magnetization at all temperatures with particle concentration can be attributed to frustration caused by the competition between particle-particle interactions and particle magnetic anisotropy on the spin-relaxation process. In concentrated samples, the particle-particle interactions become comparable to the magnetic anisotropy energies. Similar observations have been made previously [67].

Magnetization curves at low field (-20 to 20 Oe) were obtained to determine the relative inter-particle interaction parameter in each sample (Figure 16). Figure 17 shows

the relation between the initial susceptibility and temperature for the sample with 0.1%(w/w) magnetite, for the temperature range where the data follows equation (11). Using this model the interaction temperature parameter (T_0) was obtained for each sample (see Table 5-2).

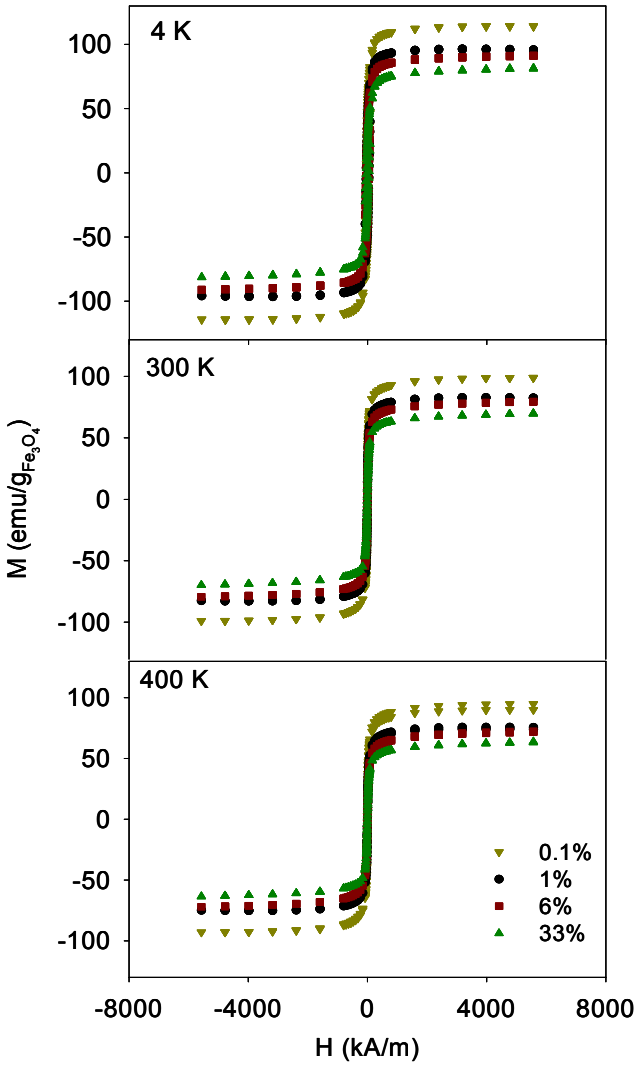

Figure 15: Magnetization curves at 4 K, 300 K and 400 K for samples of magnetite nanoparticles in a poly(styrene-divinylbenzene) matrix (0.1%, 1% and 6%) and as prepared oleic acid coated nanoparticles (33%).

Table 5-2: Magnetic properties of magnetite nanoparticle samples of different concentrations.

ϕ (w_{Fe3O4}/w)	T_0 (K)	T_B (K)	4 K				300 K	400 K
			Hc (Oe)	Mr (emu/g_{Fe3O4})	Ms (emu/g_{Fe3O4})	Mr/Ms	Ms (emu/g_{Fe3O4})	Ms (emu/g_{Fe3O4})
0.1%*	56	98	562	50	115	0.43	100	94
1%*	103	218	540	39	97	0.40	84	75
6%*	111	246	564	36	93	0.39	81	73
33%**	16	263	573	26	83	0.31	71	65

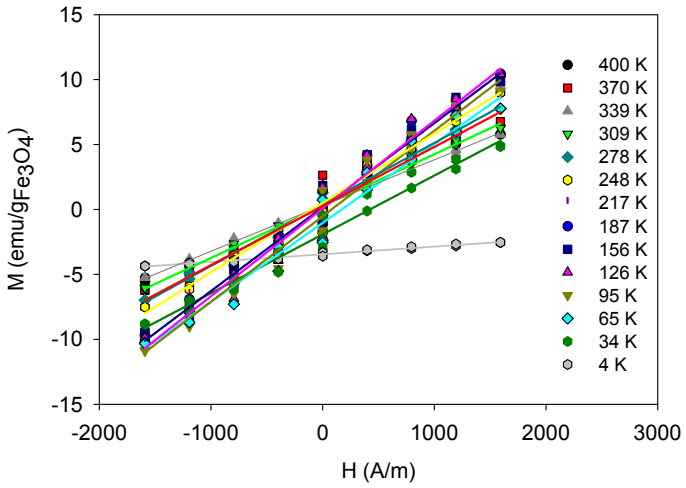

Figure 16: Low field magnetization curves for the sample with 0.1% (w/w) fraction of magnetite nanoparticles in a poly(styrene-divinylbenzene) matrix, at temperatures between 4 K and 400 K.

An increase in the interaction temperature parameter was observed with increasing particle concentration, which can be attributed to a decrease in the particle-particle distance at higher concentrations. With decreasing distance between particles the magnetic field produced by a particle increasingly influences its neighbors, which prevents the dipoles from aligning completely with the external magnetic field. In the

case of the sample at 33%, the interaction parameter was lower than the interaction parameter for the more diluted samples. This lower value can be attributed to the fact that particles could relax by both Brownian and Néel mechanisms because they are not really fixed in a solid matrix. The free oleic acid still permits particle rotation, even if it is hindered by friction. In spite of the fact that the sample with 0.1%w/w is highly diluted, particle-particle interaction was evident as the value of the interaction temperature parameter is 56 K. Lower concentrations (0.05%w/w) resulted in SQUID measurement problems due to background effects.

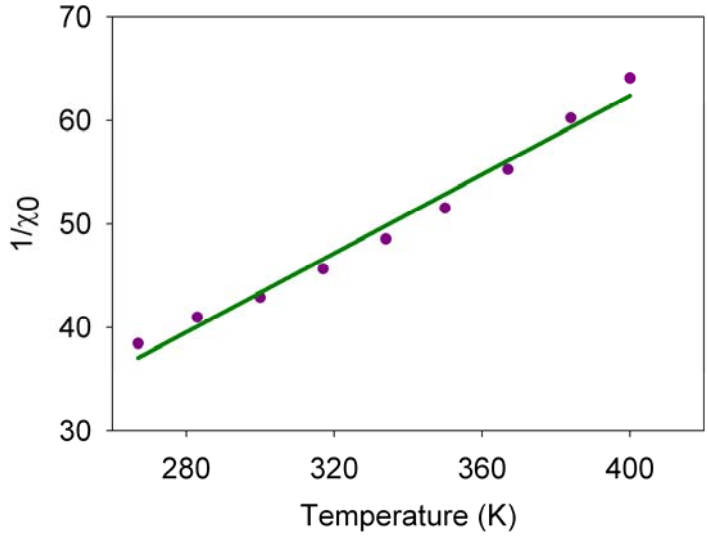

Figure 17: Initial susceptibility data fitted to Curie-Weiss model.

Zero field cooled (ZFC) and field cooled (FC) magnetization curves were obtained for each sample at 10 Oe and are shown in Figure 18. In FC curves, the magnetization continuously increases with decreasing temperature in diluted samples, in

contrast to the concentrated sample (33%w/w) where the magnetization becomes almost constant at low temperature.

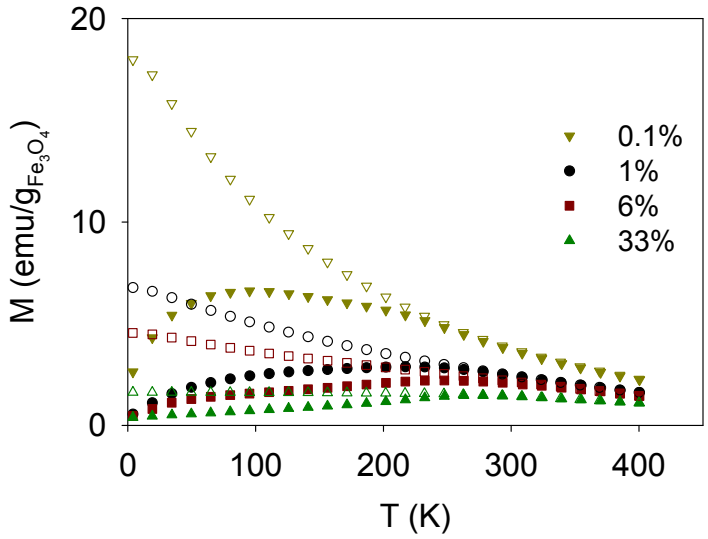

Figure 18: Zero field cooled (closed symbols) and field cooled (open symbols) magnetization curves for all samples, obtained using a 796 A/m (10 Oe) field.

The constant magnetization of the FC curve for concentrated samples can be attributed to the coupling of magnetic moments with decreasing temperature, preventing moment alignment with a field the 10 Oe. Similar behavior was observed for diluted and concentrated samples of Fe_2O_3 by Jonssson et al. [67] and for Fe_{1-x}-C_x by Hanso et al [76]. In the case of the ZFC curve, with increasing particle concentration the magnetization per particle mass decreases, while the ZFC curve peak shifts from ~ 95 K to ~ 263 K.

Using the maximum temperature of the ZFC curve, the Néel or Vogel-Fulcher relaxation time, assuming that the time scale of the measurement ($\tau = 100\ s$) is equal to

the relaxation time at the blocking temperature, and assuming $\tau_0 = 10^{-9} s$, the anisotropy constant was determined from

$$K = \frac{25 K_B (T_B - T_0)}{V_m} \tag{12}$$

Table 5-3 presents the values of the anisotropy constant obtained using these assumptions. As the concentration of the particles increases, the estimated anisotropy constant increases. Using the Néel model the values of the anisotropy constant are one order of magnetite higher than those for the bulk (135 kerg/cm^3) [77] for all samples, whereas using the Vogel-Fulcher (VF) model the anisotropy constant for the sample at 0.1%(w/w) is of the same order of magnitude as the bulk, though it is still higher by a factor of ~ 4.

Table 5-3: Anisotropy constants determined from ZFC measurements and AC susceptibility measurements using the Néel (N) and Vogel-Fulcher (VF) models.

	ZFC		AC susceptibility			
ϕ (w_{Fe3O4}/w)	K_N (kerg/cm^3)	K_{VF} (kerg/cm^3)	$\tau_{0\text{-}N}$ (s)	K_N (kerg/cm^3)	$\tau_{0\text{-}VF}$ (s)	K_{VF} (kerg/cm^3)
0.1%*	1076	464	$2x10^{-9}$	1161	$2x10^{-7}$	547
1%*	2390	1265	$2x10^{-23}$	5670	$4x10^{-16}$	2300
6%*	2690	1477	$8x10^{-30}$	7958	$5x10^{-20}$	3180
33%**	2872	2697	$2x10^{-32}$	9274	$6x10^{-31}$	8271

The in-phase χ' component of the dynamic susceptibility as a function of temperature is shown in Figure 19. With increasing particle concentration the peak of the curve shifts to higher temperatures. This shift is due to the existence of stronger particle-particle interactions [64, 67].

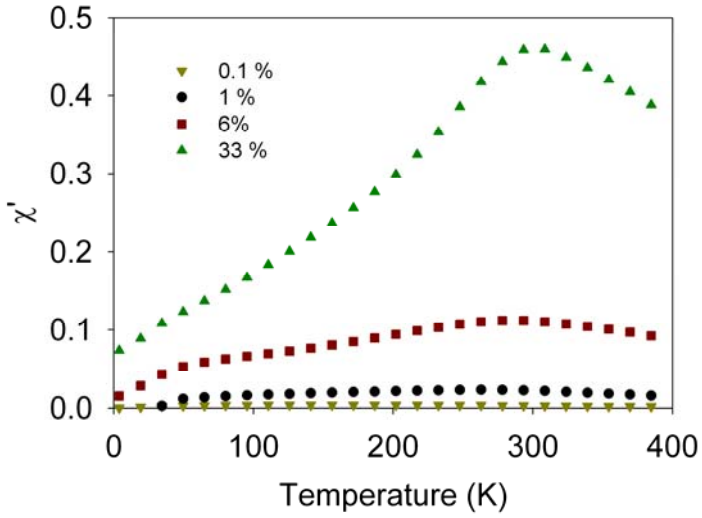

Figure 19: In-phase component of the dynamic susceptibility at 1Hz for samples with various concentrations of magnetite nanoparticles.

The in-phase component as a function of temperature at various frequencies is shown in Figure 20. As usual, the peak temperature decreased with increasing frequency. Using the values of the peak, Figure 21 was obtained. From equation (10) the anisotropy constant K and the characteristic time τ_0 for the different concentrations were obtained (Table 5-3). Physically realistic values for the characteristic time were obtained only for the sample at 0.1% whereas for the more concentrated samples this parameter was in the range of 10^{-16} to 10^{-32} s. For the anisotropy constant, a value of ~547 kerg/cm^3 was obtained for the sample at 0.1% using the Vogel-Fulcher model. This value is of the same order as that of

bulk magnetite (135 kerg/cm^3) though higher by a factor of ~4. Using the Néel model an anisotropy constant that was one order of magnitude higher than the bulk was obtained. For the concentrated samples (1%, 6%, and 33%) the value of the anisotropy constant using the two models was an order of magnitude higher than that of bulk magnetite. Although the Vogel-Fulcher considers interparticle interactions, this model works well only for weak interactions [59] which could explain the high values of the anisotropy constant obtained for the samples with concentration higher that 1% and higher. This is an indication that the interaction in these samples has a strong influence on the value of the anisotropy constant determine from the measurements, despite the fact that the nanoparticles are dispersed in a polymer matrix.

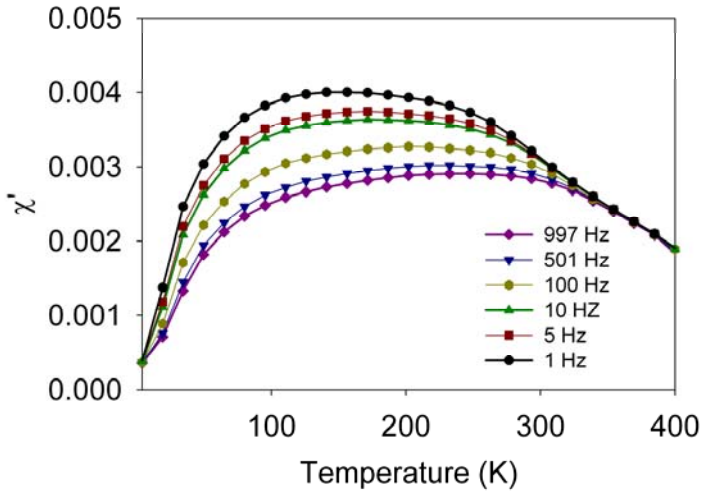

Figure 20: Variation of the in-phase component of the dynamic susceptibility with frequency for the sample with 0.1%(w/w) magnetite nanoparticles fixed in a poly(styrene-divinylbenzene) matrix.

Finally, we note that the values for K_N and K_{VF} obtained from ZFC and AC susceptibility measurements are in excellent agreement for the 0.1% sample. This is an

indication that the assumptions underlying equations (9), (10), and (11) are met and that therefore the values obtained for τ_0 and K are at least good estimates of the intrinsic properties of the nanoparticles. Because the Vogel-Fulcher model considers particle-particle interactions, for which there is evidence even in the 0.1% sample, we believe the anisotropy constant of 460-550 Kerg/cm^3 is probably the better estimate. Though these values are higher than those for the bulk (135 kerg/cm^3) they are still in the same order of magnitude.

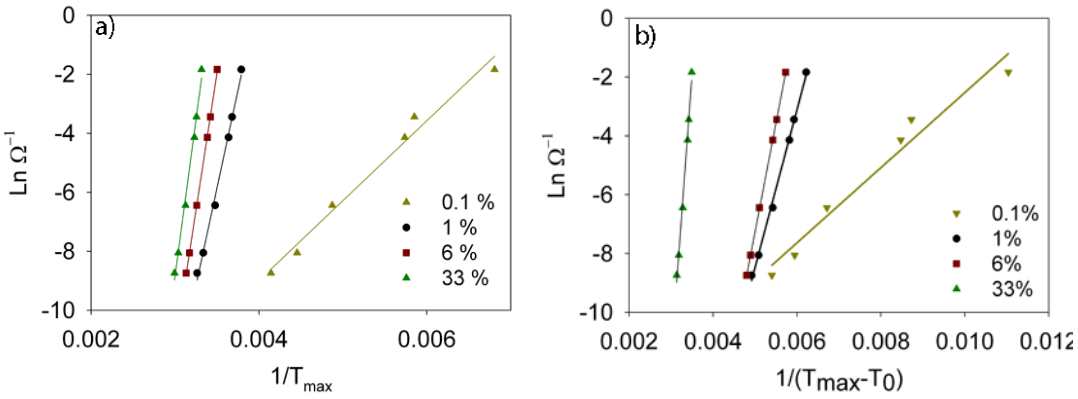

Figure 21: Plot of the inverse applied field frequency as a function of the inverse temperature corresponding to the peak of in-phase component of dynamic susceptibility. a) using Néel's model for τ and b) using the Volger-Fuchler model for τ.

5.5. Conclusions

We have demonstrated the impact of sample preparation and particle concentration on the determination of the magnetic anisotropy constant for magnetic nanoparticles. ZFC and AC susceptibility measurements were used to determine the anisotropy constant of magnetite nanoparticles using samples with several nanoparticle concentrations. As the magnetite concentration decreased, the anisotropy constant

determined from these measurements decreased down to values that were on the same order of magnitude as the bulk material. For a particle concentration of 0.1% w/w the magnetic properties determined through ZFC and AC susceptibility were in very good agreement and the value of the characteristic time τ_0 was in the expected range, indicating that the magnetic properties determined for this sample are representative of the intrinsic properties of the nanoparticles. For samples with particle concentrations higher than 1% w/w and higher, the value of τ_0 was too small to be physically valid, which indicates that though the data appears to fit the Néel and Vogel-Fulcher models, the value of the magnetic anisotropy obtained for these samples is likely an apparent or effective property of the collection of nanoparticles.

Our measurements and observations indicate that low field ZFC measurements in highly dilute samples may be used to estimate the anisotropy constant of magnetic nanoparticles. More importantly, our results indicate that monitoring the value of τ_0 obtained through AC susceptibility measurements provides a good indication of the validity of the value obtained for the magnetic anisotropy.

According to our measurements and analysis, 8.5 nm diameter magnetite nanoparticles have an anisotropy constant of approximately 460-550 kerg/cm^3, which is higher than, but in the same order of magnitude as the bulk material.

6. EFFECT OF PARTICLE SIZE ON THE MAGNETIC ANISOTROPY OF MAGNETITE NANOPARTICLES

Magnetite nanoparticles of 6, 9, and 11 nm diameter were synthesized by the thermal-decomposition method. DC and AC measurements were used to determine the anisotropy constant of magnetic nanoparticles fixed in a cross-linked polymer matrix. Néel and Vogel-Fulcher relaxation models were used to determine the anisotropy constant. Values of the anisotropy constant of ~ 600 kerg/cm^3 and ~ 300 kerg/cm^3 were obtained using the Néel model while values of ~ 160 kerg/cm^3 and ~90 kerg/cm^3 were obtained using the VF model for particles with 6 and 9 nm, respectively. For the sample with particles of 11 nm diameter, the anisotropy constant determined using AC susceptibility was higher (>100%) than the anisotropy constant obtained through ZFC curve. This discrepancy between these values was attributed to wide size distribution (ln $\sigma = 0.23$) of the sample which affected the determination of the anisotropy constant using these techniques. Using ZFC curves a decrease in the anisotropy constant from 610 kerg/cm^3 to 129 kerg/cm^3 using the Néel model and from 183 kerg/cm^3 to 45 kerg/cm^3 using the VF model were obtained with increasing diameter from 6 to 11 nm. Whereas using AC susceptibility measurements, first a decrease in the anisotropy constant was observed with increasing diameter from 6 nm to 9 nm then a decrease in the anisotropy constant was obtained with increasing from 9 nm to 11 nm diameter. This increase in the anisotropy constant was attributed to the wide size distribution of the nanoparticles.

Previous studies on the effect of nanoparticle diameter on magnetic properties of ferrites have been reported. Roca et al [28] obtained highly crystalline magnetite nanoparticles using two methods. In the first method, iron-oleate was added to a mixture of oleic acid and octyl ether. The solution was heated to reflux for 30 minutes. Particles with 11 nm diameter were obtained. In the second method, iron acetylacetonate was mixed with 1,2-hexadecanediol, oleic acid, oleylamine, and phenyl ether. The mixture was heated to 200 ºC for 30 min. Afterwards, the mixture was heated to reflux and kept at this temperature for 30 min. With this process, particles with a diameter of ~6 nm were obtained. Particles of ~7 nm diameter were synthesized using as seeds the particles of ~ 6 nm diameter. In this case, seed particles in phenyl ether were mixed with iron acetylacetonate and 1,2-hexadecanediol and heated to 200 ºC for 30 min. Then, the mixture was heated to reflux for 30 min. TEM images showed that the synthesized particles were spherical with the exception of the 11 nm particles which had diamond, cubic, and triangular shapes. Magnetic measurements revealed superparamagnetic behavior at room temperature for all samples. Saturation magnetization was observed to decrease with decreasing particle diameter, which was attributed to an increase in the surface area/volume ratio which increases canting effects at the surface. At 5 K, hysteresis was observed and coercivities from 300 to 175 Oe were obtained when the particle diameter diminished from 11 to 6 nm. The decrease in coercivity with diameter indicated that surface anisotropy is not the origin of the coercivity. Therefore they considered that the oleic acid bound to the surface produces a decrease in the spin disorder at the surface, decreasing in this way the surface anisotropy. The peak of the ZFC curve shifted to lower temperatures when the diameter decreased. Using the value of

the peak, the anisotropy constant was determined. A decrease in the anisotropy constant from 4 x 10^5 erg/cm^3 to 3 x 10^5 erg/cm^3 with particle size from 11 nm to 6 nm was observed.

Lin et al [16] observed opposite magnetic behavior for particles between 8 and 18 nm. Particles were synthesized in two organic solvents by thermal-decomposition of FeO(OH) with oleic acid. The synthesis process consisted in the preparation of a solution with the precursor, the organic solvent (octadecene or docosane), and oleic acid. The solution was heated to reflux and kept at this temperature for a determined time (1 – 5 h). The ratio of OA/Fe determined the final particle size. Particles with diameters in the range of 8 to 11 nm were obtained using octadecene as solvent whereas diameters in the range of 11 to18 nm were obtained using docosane. X-ray diffraction patterns showed peaks characteristic of a ferrite crystalline structure. Due to the brownish luster color of the sample a mixture of magnetite and maghemite was considered. Magnetic measurements were done with the sample as synthesized. ZFC curves showed that the blocking temperature decreased with particle size. Using the value of the peak, anisotropy constants in the range of 3.2 x 10^5 – 8.2 x10^5 erg/cm^3 were obtained where the higher value corresponded to the smaller particle size. In this work, surface anisotropy was considered to be responsible of the increase in the anisotropy constant with decreasing particle size. Also, surface anisotropy was considered to cause the decrease in saturation magnetization with diameter. Note that in this study, as in Roca et al, the particles were coated with OA.

Reverse micelles under reflux conditions were used by Lee et al [37] to synthesize magnetite nanoparticles. Magnetite particles with 3, 5, and 7 nm were synthesized by adding hydrazine at 100 ºC to a solution formed by aqueous iron salt solution, sodium dodecylbenzenesulfonate, and xylene. Then, the mixture was heated to reflux. Magnetic measurements revealed an increase in blocking temperature (45 K to 85 K and to 105 K) and saturation magnetization (135 emu/g to 152 emu/g and to 173 emu/g) with particle size (3 nm, 5 nm, and 7 nm). Saturation magnetization decreased with size which was attributed to surface effects.

Table 6-1 shows a literature review of the effect of particle diameter on anisotropy constant value.

Table 6-1: Literature review of the diameter effect on anisotropy constant value

	Particles	Matrix	ZFC	AC susceptibility
Hou et al (2003)	Fe_3O_4		$32x10^5$ erg/cm^3 (8 nm) $9\ x10^5$ erg/cm^3 (11nm)	
Lin et al (2006)	Fe oxide	Organic solvents	3-8 $x10^5$ erg/cm^3 18-8 nm	
Roca et al (2006)	Fe_3O_4		3-4$x10^5$ erg/cm^3 6-11 nm	
Guardia et al (2007)	Fe_3O_4	powder	$5x10^5$ erg/cm^3 6 nm	
Peddis et al (2008)	$CoFe_2O_4$	silica		$2x10^6$erg/cm^3 (2 nm) $t_0=10^{-11}$ s 5% $2x10^5$erg/cm^3 (7nm) $t_0=10^{-14}$ s 15%

In the majority of the literature, authors do not report the method of preparation of samples for magnetic measurements which, as was demonstrated Chapter 5, has a strong influence on magnetic properties determined experimentally. In many cases, the magnetic measurements are done with powder samples or with samples as synthesized where particle-particle interactions could have a profound effect on these measurements. Here, we report near-intrinsic magnetic properties of magnetite nanoparticles with diameters of 6, 9, and 11 nm. Samples in a PSDVB matrix with 0.1% magnetite nanoparticles were used.

6.1. Materials

Iron (III) acetylacetonate ($Fe(C_5H_7O_2)_3$, 99.9 % metal basis), was obtained from Sigma Aldrich and used as metal precursor; Oleic acid ($CH_3(CH_2)_7CH=CH(CH_2)_7COOH$, 99% pure) and Oleylamine ($CH_3(CH_2)_7CH=CH(CH_2)_7CH_2NH_2$, >70 % GC) from Sigma Aldrich were used as surfactants; 1,2-hexadecanediol ($CH_3(CH_2)_{13}CHOHCH_2OH$, 90% from Sigma Aldrich) was used as oxidizing agent. Solvents used were octadecene ($CH_3(CH_2)_{15}CH=CH_2$ from Fluka), hexane ($CH_3(CH_2)_4CH_3$, reagent grade from Sigma Aldrich), ethanol (CH_3CH_2OH, 99% pure from Aldrich), and chloroform ($CHCl_3$, 99% pure from Fisher).

6.2. Synthesis procedure

Magnetite nanoparticles were synthesized through the thermal-decomposition method, by adding iron (III) acetylacetonate at a concentration of 0.1 M to an octadecene solution with 0.3 M oleic acid, 0.3 M oleylamine, and 0.3 M 1,2-hexadecanediol. The mixture was heated at a rate of 12.5 °C/min to nucleation temperature and was kept at this temperature for a specified time. Then the mixture was heated at a rate of 3.5 °C/min to the growth temperature and kept at this temperature for a specified time. After synthesis, the solution was cooled and washed with ethanol and chloroform. Initially, ethanol was added to the solution and particles were precipitated by centrifugation for 20 min at 8000 rpm. The precipitate was re-suspended in chloroform to separate the free oleic acid. Ethanol and centrifugation were used again to precipitate the nanoparticles. The precipitate was suspended in hexane by ultrasonication. The solution was centrifuged to 2000 rpm for 10 minutes to precipitate the un-suspended nanoparticles. The precipitate was dried in a vacuum oven at 80 °C.

In order to obtain particles with different diameters, the temperature and time during the nucleation and growth stages were varied (see Table 6-2).

Table 6-2: Synthesis conditions for synthesis of magnetite of several diameters by thermal-decomposition method

Run	T_1	t_1	T_2	t_2
1	150	120	300	120
2	250	60	320	60
3	150	120	320	60

6.3. Characterization

Morphology of the particles was characterized using a Zeiss 922 200 kV Transmission Electron Microscope. Samples were prepared by suspending the dry nanoparticles in hexane and sonicating for 10 minutes. An ultrathin carbon grid was submerged in the solution. The grid was placed on filter paper to absorb the excess solvent and dried at room temperature to promote the slow evaporation of the solvent and thereby obtain a uniform deposition of nanoparticles on the grid. Then the grid was placed in a vacuum oven at 80 ºC to assure the complete evaporation of the solvent. Crystallographic analysis was done in a Rigaku Ultima II X-ray diffractometer. Thermogravimetric analysis was done in a Q-2950 TGA from TA Instruments.

In order to determine the intrinsic magnetic properties, the nanoparticles were fixed in a solid matrix of poly(styrene-divinylbencene). The nanoparticles were suspended in a solution of styrene with 15%(v/v) of DVB and 0.37%(w/w) of azobisisobutyronitrile (AIBN). Magnetite nanoparticles were added to the solution to obtain a concentration of 0.1% (w/w). The mixtures were heated at 70 ºC until polymerization was complete.

Magnetic properties were measured using a Quantum Design MPMS XL-7 SQUID magnetometer. Zero field cooled curves were obtained by cooling the sample under zero applied field to 4 K, then applying the desired field and warming the sample to 400 K taking magnetization measurements at regular intervals. Field cooled curves were obtained by cooling the sample from 400 K to 4 K under the applied field, taking

magnetization measurements at regular intervals. Magnetization curves were obtained at 4 K, 300 K, and 400 K with up to 7 Tesla fields. Also, magnetization curves were obtained at low field (± 20 Oe) for temperatures between 4 and 400 K. The AC susceptibility of the samples was measured as a function of temperature using 4 Oe drive amplitude and a frequency range of 1 to 1000 Hz.

6.4. Results

Near-spherical and non-agglomerated nanoparticles were obtained by the thermal-decomposition method (Figure 22). The average diameter of the nanoparticles was obtained by measuring the diameter of 300 particles using the imageJ program and fitting to a log-normal distribution. Particles of 6, 9 and 11 nm diameter with geometric deviations smaller than 0.23 were obtained. X-ray diffraction showed that the nanoparticles synthesized are highly crystalline. The presence of several peaks characteristic of the inverse spinel structure confirmed the formation of a ferrite. A lattice parameter of a = 8.38 Å was obtained, which is comparable with that of bulk magnetite (a=8.39 Å).

Thermo gravimetric analysis showed large drops in sample weight at ~200 ºC and ~400 ºC which were attributed to free oleic acid and oleic acid bound to the surface of the nanoparticles, respectively. Samples in poly(styrene-divinylbenzene) were prepared with 0.1% (w/w) of magnetite nanoparticles using results from TGA.

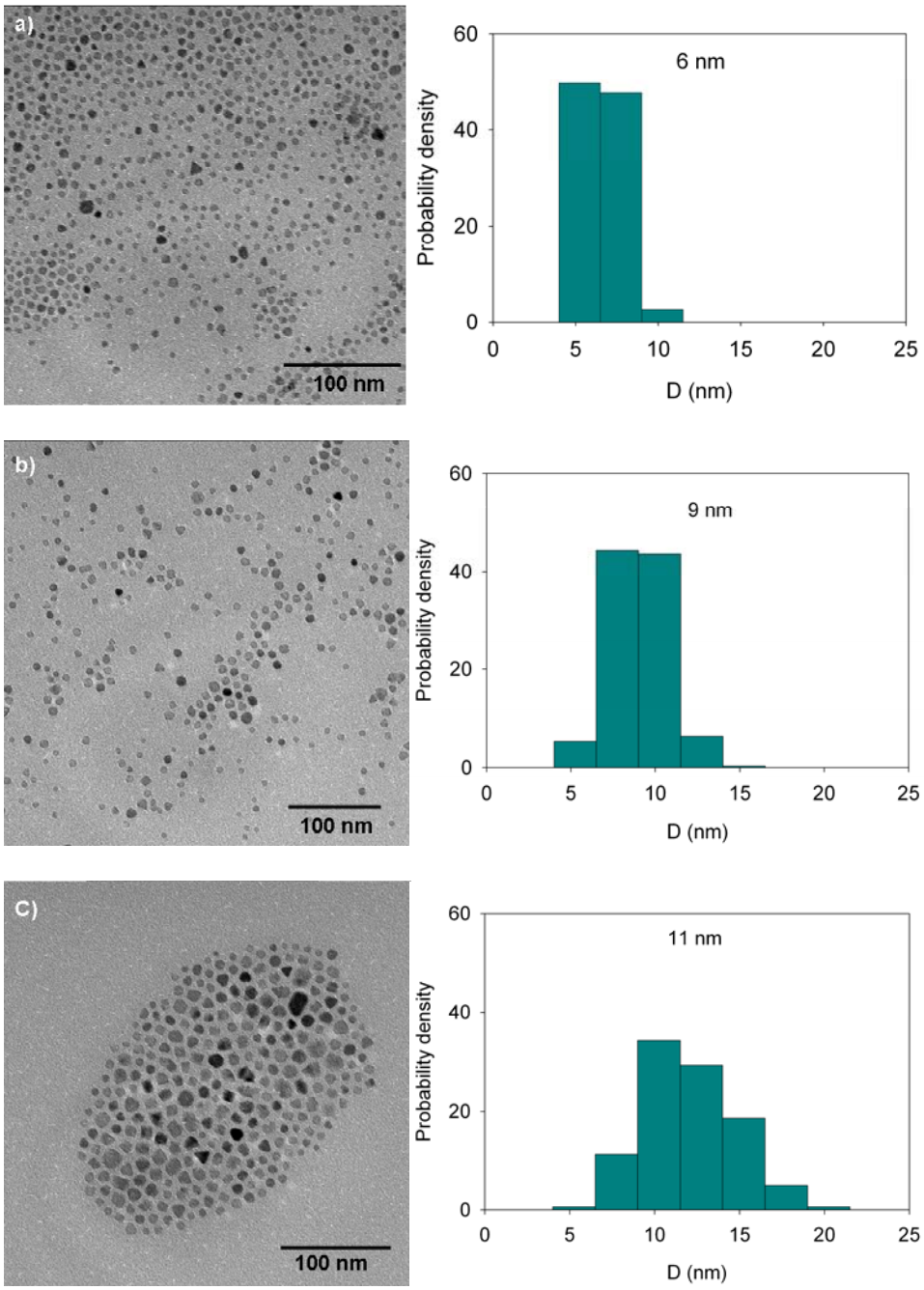

Figure 22: TEM images and size distribution of magnetite nanoparticles synthesized by thermal-decomposition method: a) T_1= 150 ºC, t_1=120 min., T_2= 300 ºC, t_2=120 min; b) T_1= 250 ºC, t_1= 60 min., T_2= 320 ºC, t_2= 60 min; c) T_1= 150 ºC, t_1=120 min., T_2= 320 ºC, t_2=60 min

The DSC curve for PSDVB showed no transitions in the measured temperature range (see appendix B.2), which indicates that the polymer chains are rigid and therefore

the particles fixed in the matrix would not physically rotate during the magnetic measurements.

Magnetization curves at 4 K, 300 K, and 400 K are shown in Figure 23. At 4 K hysteresis was observed for all samples whereas at 300 K and 400 K hysteresis was not observed. At 4 K, magnetite nanoparticles presented coercivities of up to ~500 Oe and remanence of up to ~ 60 emu/$g_{Fe3O4.}$ Table 6-3 summarizes values of coercivity, remanence, and saturation magnetization at 4 K, 300 K, and 400 K. An increase in coervicity with diameter was observed whereas no clear correlation was observed between diameter and saturation magnetization or remanence, which was attributed to two factors. First, the size distribution of the particle may affect these observations. The particles with 6 and 9 nm diameter presented a narrow size distribution whereas particles of 11 nm had a wider size distribution. With increasing diameter from 6 to 9 nm, the saturation magnetization increases whereas increasing the diameter from 9 nm to 11 nm results in a decrease in saturation magnetization.

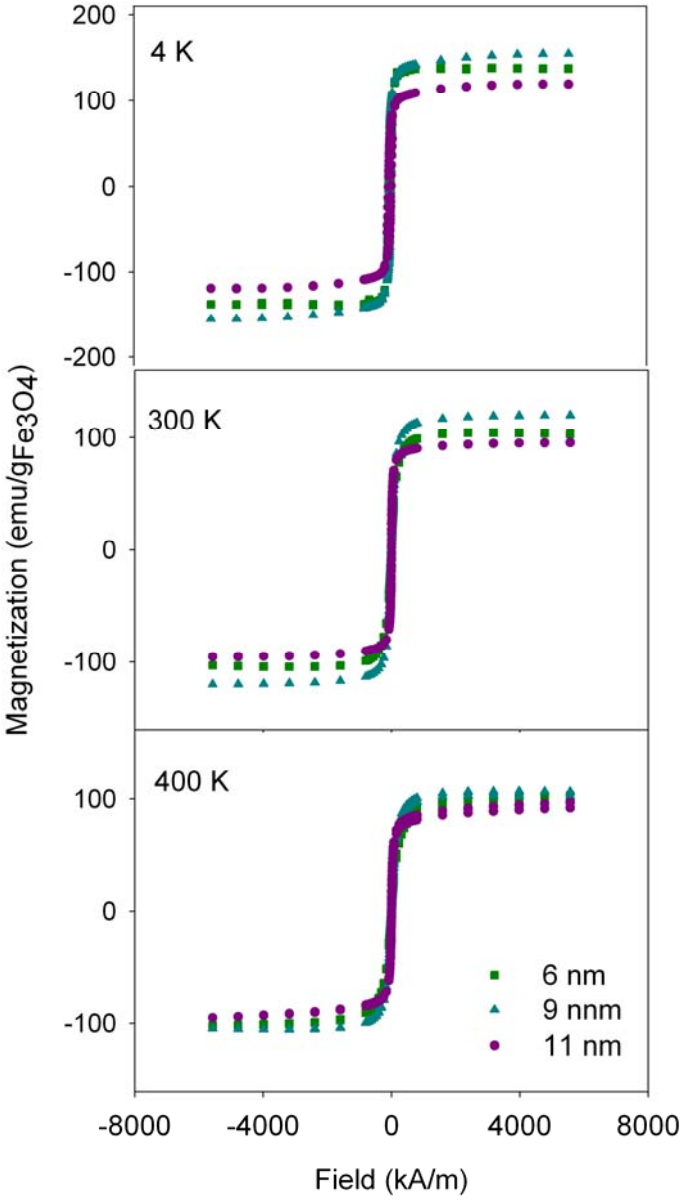

Figure 23: Magnetization curves at 4, 300, and 400 K of magnetite nanoparticles with diameter of 6, 9, and 11 nm fixed in a poly(styrene-divinylbenzene) matrix.

It is expected that upon increasing the particle diameter, the saturation magnetization would increase due to an increase in the relative volume of the magnetic core. In contrast, a decrease in the saturation magnetization was obtained which was

attributed to small particles presented in the polydisperse sample. The second factor affecting these observations are errors in mass determined by TGA. An error of 0.01% in the Fe_3O_4 mass produces a difference of ~10 % in the value calculated for the saturation magnetization.

Table 6-3: Magnetic properties of magnetite with different diameters.

D (nm)	T_0 (K)	T_B (K)	4 K				300 K	400 K
			Hc (Oe)	Mr (emu/g_{Fe3O4})	Ms (emu/g_{Fe3O4})	Mr/Ms	Ms (emu/g_{Fe3O4})	Ms (emu/g_{Fe3O4})
6	14	20	377	61	141	0.43	108	99
9	16	25	378	60	159	0.38	122	106
11	17	26	496	49	123	0.40	97	97

The interaction temperature parameter (T_0) was determined by measuring the initial susceptibility at low fields in a temperature range of 4 K – 400 K (Figure 24). The data were well described by the Curie-Weiss model, equation (11). As expected, T_0 was similar for the three samples because they had the same mass fraction of particles. This indicates that the separation between particles was similar (Table 6-3).

ZFC and FC magnetization was measured by applying a magnetic field of 10 Oe (Figure 25). The continuous increase in the FC magnetization with decreasing temperature indicates that interparticle interactions were weak. The ZFC peak shifted to higher temperatures with increase in particle diameter (Table 6-3). This indicates that

particles are blocked at higher temperatures when the diameter increases. It was noticed that ZFC magnetization curve for the magnetite particles with 11 nm diameter presented a wide peak which was attributed to the broader size distribution ($\ln \sigma = 0.23$) compared to the particles with 6 and 9 nm diameter ($\ln \sigma = 0.19$ for these samples).

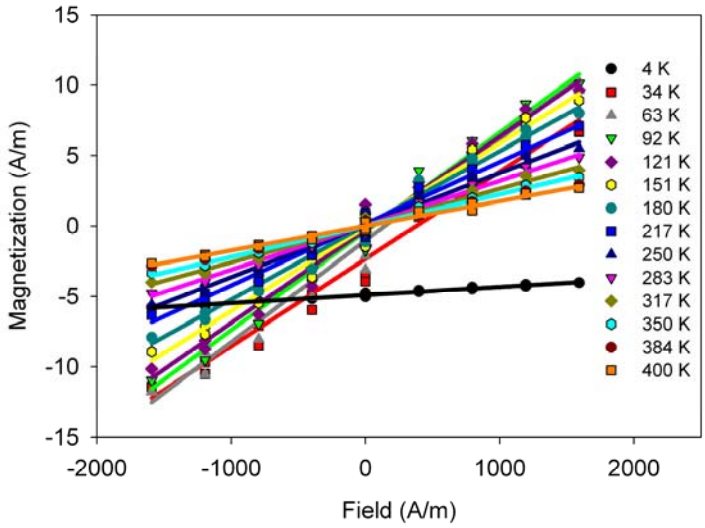

Figure 24: Magnetization curve at low field for magnetite nanoparticles of 6 nm

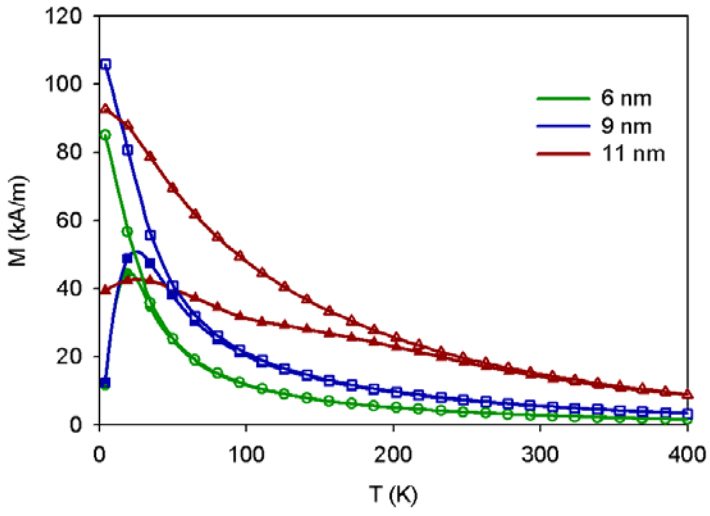

Figure 25: Zero field cooled (closed symbols) and field cooled (open symbols) magnetization curves for magnetite nanoparticles with 6, 7, and 11 nm.

The anisotropy constant was determined using equation (12) (Table 6-4). Values of the anisotropy constant in the same order of magnitude as the bulk were obtained. An increase in the anisotropy constant from 129 to 617 kerg/cm^3 with decreasing particle diameter from 11 to 6 nm was observed using the Néel model whereas an increase from 45 to 183 Kerg/cm^3 were obtained using the VF model. This increase in the anisotropy constant could be attributed to a spin disorder layer present at the surface. With diminishing particle size, the spin disorder layer has more influence on the surface anisotropy, as a consequence of the increase in surface area/volume ratio.

Table 6-4: Anisotropy constants determined from ZFC measurements and AC susceptibility measurements using the Neel (N) and Vogel-Fulcher (VF) models.

	ZFC		AC susceptibility			
D (nm)	K_N (kerg/cm^3)	K_{VF} (kerg/cm^3)	$\tau_{0\text{-}N}$ (s))	K_N (kerg/cm^3)	$\tau_{0\text{-}VF}$ (s)	K_{VF} (kerg/cm^3)
6	610	183	$1x10^{-10}$	623	$6x10^{-7}$	168
9	255	82	$1x10^{-12}$	311	$2x10^{-7}$	96.8
11	129	45	$1x10^{-15}$	415	$6x10^{-13}$	251
Bulk	135					

Figure 26 shows the in-phase component of the susceptibility for the magnetite particles. It was observed that the peak shifts to higher temperatures as the diameter increases whereas the peak magnitude decreases. Again, a wide peak was observed for 11 nm magnetite particles. The anisotropy constant was determined through equation (10) using the peak value of the temperature dependence of the in-phase component of the susceptibility at several frequencies (Figure 27) and the values are shown in Table 6-4.

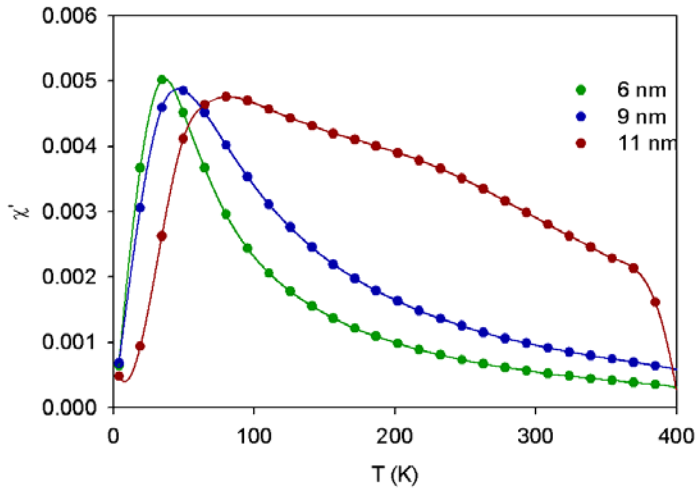

Figure 26: In-phase component of the dynamic susceptibility at 1 Hz for magnetite nanoparticles.

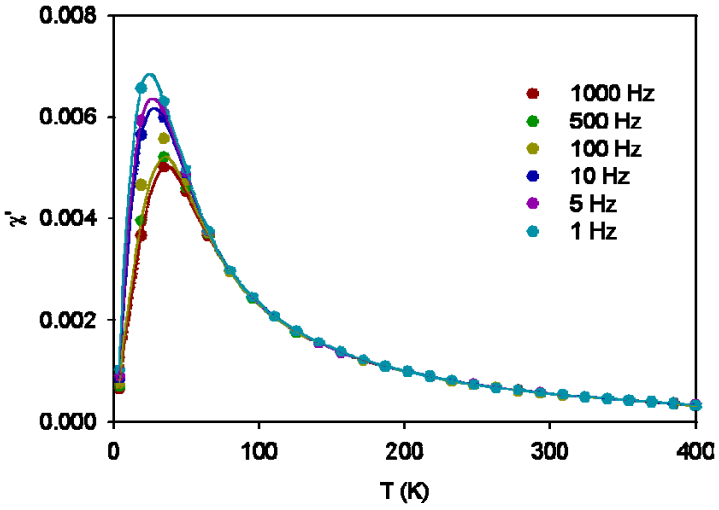

Figure 27: In-phase component of the dynamic susceptibility of 6 nm particles at several frequencies.

Increasing the diameter from 6 to 9 nm, the anisotropy constant decreased from 623 to 311 kerg/cm^3. Whereas increasing the diameter from 9 to 11 nm, the anisotropy increased but it was smaller than the anisotropy constant of 6 nm particles. This increase was attributed to the presence of particles with diameter less than 11 nm which contribute

to the surface anisotropy. The characteristic time τ_0 was in the expected range for the samples with nanoparticles with 6 and 9 m in diameter which indicates that the anisotropy constants values determined by AC susceptibility are reliable. Whereas for magnetite of 11 nm, τ_0 value was too small to be physically realistic.

6.5. Conclusions

Highly crystalline magnetite nanoparticles with diameters of 6, 9, and 11 nm and narrow size distribution were synthesized by the thermal-decomposition method. Magnetic properties were determined by fixing the magnetic nanoparticles in a polystyrene-divinylbenzene (PSVB) matrix to avoid particle rotation. The anisotropy constant was determined using ZFC and AC susceptibility measurements. As the particle diameter decreased, the anisotropy constant determined from these measurements increased to values that were larger but in the same order of magnitude as the bulk material. The value of τ_0 for the three samples was in the range expected, indicating that the anisotropy constant values were reliable and representative of the intrinsic anisotropy constant. The determination of the anisotropy constant using AC susceptibility measurements was affected by the wide size distribution giving a value of anisotropy constant higher than the value of the anisotropy constant determine by ZFC. One potential source of the discrepancy is that in using ZFC curves a characteristic time τ of 10^{-9} s is assumed whereas using AC susceptibility measurements values of $\tau = 10^{-15}$ and

10^{-13} s are obtained. Additionally, a broad size distribution implies a distribution of relaxation times which have a strong impact in AC susceptibility measurements.

Based on our measurements, magnetite nanoparticles of 6, 9, and 11 nm possess an anisotropy constant of approximately ~ 170-180, ~ 80-100, and ~ 50 kerg/cm^3 which is in the same order of magnitude as the bulk material.

7. LIGAND EXCHANGE AND FUNCTIONALIZATION OF PARTICLES FOR SENSOR APPLICATIONS

Cobalt-substituted ferrite ($Co_{0.78}Fe_{2.22}O_4$) nanoparticles functionalized with carboxylic groups were obtained by ligand exchange between oleic acid and COO^--silane. COO^--cobalt-ferrite nanoparticles could be suspended in water and do not precipitate for more than 6 months. Stability studies showed that aqueous ferrofluid was stable in a wide range of pH (3-10). COO^--cobalt-ferrite nanoparticles were tested as sensors using biotin-avidin complex and AC susceptibility measurements. Biotin was successfully attached to the COO^--$CoFe_2O_4$ nanoparticles through amine linkage. Avidin was detected using the frequency-dependent out-of-phase component of the AC susceptibility. A shift in the out-of-phase component was observed after addition of avidin solution due to an increase in the hydrodynamic diameter of the nanoparticles after attachment of avidin. The temporal change in out-of-phase component at 100 Hz was measured. A decrease in χ'' was observed due to an increase of the hydrodynamic nanoparticle diameter after avidin addition. Similar measurements could be used to study nanoparticle binding and aggregation due to biomolecular interactions.

7.1. Ligand Exchange

One disadvantage of the thermal-decomposition method is that the nanoparticles obtained are immiscible in aqueous solutions because the surfactants used in this method possess hydrophobic chains. Such particles are not suitable for biological applications. Additionally, the majority of surfactants used in the thermal-decomposition method, such as oleic acid, do not possess a functional endgroup, limiting the functionalization of these nanoparticles.

In order to use these nanoparticles in biological applications, they must be transfered to aqueous solution. Sun et al [78] synthesized FePt nanoparticles with oleic acid ligands which were exchanged by dodecanethiol and 11-mercaptoundecanoic acid ligands. In both cases, the FePt nanoparticles were dispersed in a solution of hexane and octane (50/50) and the ligand was added to the solution. 11-mercaptoundecanoic acid was dissolved in ciclohexanone before adding to the ferrofluid. The mixture was shaken and nanoparticles washed with ethanol and resuspended in distilled water and ammonium hydroxide. XPS confirmed the exchange of ligand. Binding energies of 164 and 400 eV were observed which are characteristic of sulfur and nitrogen and a shift of the S2p peak was obtained due to binding of sulfur and iron. The oxygen peak at 533 eV decreased, indicating that most of the oleic acid was replaced by dodecanethiol. Sun et al [79] replaced oleic acid on iron oxide nanoparticles with tetramethylammonium 11-aminoundecanoate. The nanoparticles were re-suspended in hexane and mixed with a solution of tetramethylammonium in dichloromethane, obtaining water-soluble

nanoparticles. IR spectra show bands in 1564 and 1478 cm^{-1} corresponding to free tetramethylammonium 11-aminoundecanoate, confirming ligand exchange.

Oleic acid-maghemite nanoparticles with Fe-rich surfaces were synthesized and modified to be hydrophilic with 3-mercaptopropionic acid (MPA) by Woo et al [80]. The nanoparticles in octyl ether were mixed with 3-mercaptopropionic acid and the solution was heated to reflux. Then, ethanol was added to precipitate the nanoparticles. XRD patterns verified the presence of MPA bound on the particle surface, peaks due to planes (110), (112), (114), and (300) of the hexagonal FeS were observed, which were attributed to covalent bonds between Fe and S. FTIR showed an increase in the bands at 3380 and 603 cm^{-1} of the O-H and Fe-O bonds respectively and a decrease of C-H band at 3000 cm^{-1} after ligand exchange. The change in the spectrum was attributed to decreasing of the organic chain length from C_{18} of the oleic acid to C_3 of the MPA.

Ligand exchange was also used by de Palma and co-workers [81] on hydrophobic magnetic nanoparticles using alkylsilanes with different functional endgroups (amino-, aldehyde-, isocyanate-, thiol-, cyano-, acrylate-, carboxylic acid-, and polyethylene glycol-silane). The nanoparticles suspended in hexane with 0.01 % (v/v) acetic acid were mixed with a solution of 0.5 % (v/v) of trialkoxysilane. The mixture was shaken for 72 h and a precipitate was observed. In the case of ligand exchange with COOH-, NH_2-, and PEG-silanes complete precipitation was obtained. The precipitate was washed with hexane to remove excess silanes and then redispersed in deionized water. FTIR confirmed the exchange of oleic acid with alkylsilanes. A broadening and shift of the band at 585 cm^{-1} characteristic of Fe-O was observed and attributed to the formation of Fe-O-Si bond. New bands at 1000 and 1150 cm^{-1} were obtained which are characteristic

of Si-O-Si vibrations. When acrylate-, thiol-, amino-, and carboxylic acid-silanes were used, a band at 2954 cm^{-1} was observed which was attributed to the symmetric CH_3 stretching of the alkoxy anchor group. The bands characteristic of the endgroups also were observed in each case. XPS was used to calculate the surface elemental composition and concentrations. An increase in the concentration of silane after exchange was obtained whereas a decrease in the Fe and Co concentration was found. The decrease in Fe and Co concentrations was attributed to the attenuation of the Fe2p and Co2p photoelectron through the silane layer. XPS spectra of the modified nanoparticles show peaks at 531.5 and 532.5 eV which were assigned to Fe-O-Si and Si-O bonds, respectively.

7.1.1. Silane coupling agents

Silicone coupling agents or organofunctional silicones have been used to improve bonding of organic resins to mineral surfaces. Organofunctional silicones are hybrids of silica and organic materials with the general formula X_3SiRY, where Y is an organofunctional group and X is a hydrolyzable group. In general, the organofunctional group is selected for its reactivity with either a polymer or biomolecule while the hydrolyzable group serves as intermediate in formation of silanol groups for bonding to mineral surfaces [82].

One of the most common hydrolysable groups are the trialkoxysilanes, $YSi(OR)_3$, which hydrolyze in water to give silanols and then condense to siloxanes (see Figure 28).

Both reaction rates depend on pH, the hydrolysis reaction being faster than the condensation reaction. The hydrolysis reaction rate depends also on the alkoxysilane size, longer chains hydrolyze more slowly because of their hydrophobicity [82].

$$YSi(OR)_3 \xrightarrow{H_2O} YSi(OH)3 \rightarrow HO- \begin{matrix} R \\ Si \\ OH \end{matrix} - \left(-O- \begin{matrix} R \\ Si \\ OH \end{matrix} - \right)_n -O- \begin{matrix} R \\ Si \\ OH \end{matrix} -OH$$

Figure 28: Schematic of hydrolization of trialkoxysilane

When metals and metal oxides are in equilibrium with atmospheric moisture, water is adsorbed on the metal surface as hydroxyl groups (M-OH) and as molecular water held by hydrogen bonding with the surface hydroxyls. These hydroxyl groups and water layer are enough to hydrolyze the alkoxysilane group to silanols, which form strong hydrogen bonds and covalent oxane bonds (M-O-Si) with the mineral surface. Although the alkoxysilanes have three reactive silanols per molecule, only one silanol group can bond to the glass surface because reactive sites are spaced. The other two silanol groups may condense to form a siloxane layer or remain partly uncondensed at the surface [82].

7.1.2. Materials

N-(trimethoxysilylpropyl)ehtylenediamine triacetic acid ($C_{14}H_{25}Na_3O_9Si$, 50% inwater) was acquired from UCT specialties: acetic acid (CH_3COOH,), hexane (C_6H_{14}),

and cellulose membrane (6 – 8 kD) from Fisher Scientific. Deionized water (0.05 uS/cm) was obtained by treatment (Barnstead Nanopure Diamond).

7.1.3. Characterization

Using a Zeiss 922 200 kV Tansmission Electron Microscope, morphology of the particles was determined. Samples were prepared by submerging an ultrathin carbon grid in the particle solution. The grid was placed on filter paper to absorb the excess solvent and dried at room temperature to promote the slow evaporation of the solvent to obtain a uniform deposition of nanoparticles on the grid. Then the grid was placed in a vacuum oven at 80 ºC to assure the complete evaporation of the solvent. A Brookhaven Instruments BI-90 Plus Particle Size and Zeta Poetential Analizer was used to measure the hydrodynamic diameter and zeta potential of the particles. In order to confirm ligand exchange, Fourier Transform Infrared spectra were obtained in a Varian 800 FT-IR. Magnetic properties were measured using a Quantum Design MPMS XL-7 SQUID magnetometer.

7.1.4. Ligand exchange procedure

Cobalt-substituted ferrite nanoparticles with 11 nm diameter and geometric deviation of 0.12 were synthesized by the thermal-decomposition method described in Section 4.2. The nucleation and growth temperatures were 150 ºC and 300 ºC, respectively, with a reaction time of 60 min in each stage.

Magnetic nanoparticles, as prepared, were suspended in hexane at a concentration 9.9 mg/ml. 25 µl of acetic acid were added to the solution and mixed for 10 min by sonication, then 4 ml of COO-silane were added. The solution was heated to 60 ºC under vigorous stirring and kept at this temperature for 48 hours. After 48 hours, the solution was removed and a precipitate was observed. 20 ml of DI water was added to suspend the precipitate and then the solution was stirred for 2 min and allowed to rest in a separation funnel. Two phases were formed: a clear organic solvent (hexane) and a black aqueous solution, where the majority of the particles were present. The aqueous phase was recovered and dialyzed for 48 hours with DI water to eliminate the COO-silane unattached to the particles. DI water was changed every 12 hours.

7.1.5. Results

FTIR (Figure 29) confirmed the attachment of COO^--silane to the particle surface. Bands of vibrations of COO^- (~1570 cm^{-1}), COH (~1400 cm^{-1}), and CO (~1328 cm^{-1}) characteristic of carboxylic groups were observed. Bands at ~1100 cm^{-1} and ~923 cm^{-1} were also observed which were attributed to presence of Si-O-CH_3 and Si-OH. A low intensity band at ~2040 cm^{-1} (CH_2) indicated a decrease in the length of carbon chain due to exchange of oleic acid by COO^--silane.

TEM (Figure 30) revealed non-agglomerated nanoparticles and closed-packed arrangement after ligand exchange. Interparticle distance was measured before and after

ligand exchange. A decrease from ~4 nm to ~2 nm in interparticle distance after ligand exchange was observed which indicated decrease in the length of the molecules attached to the particle surface. Oleic acid length is ~ 2nm whereas COO^--silane length is ~ 1nm. Therefore ~ 4 nm in interparticle distance indicated an oleic acid monolayer whereas ~ 2 nm indicated a COO^--silane monolayer which confirmed the ligand exchange.

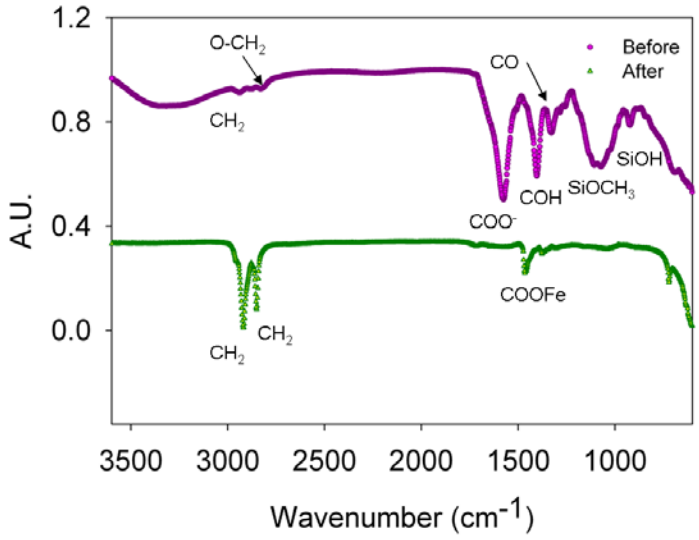

Figure 29: FTIR of cobalt-substituted ferrite nanoparticles before and after ligand exchange between oleic acid and COO^--silane.

After ligand exchange, the particles could be suspended in DI water in contrast with the particles without exchange which only suspended in organic solvents. COO^- -silane nanoparticles suspended in water were stable for more than one year.

Stability analysis was done by measuring zeta potential of particles in aqueous solution. Figure 31 reveals that particles were stable with negative charge in a wide pH range (3 -10). A schematic of the particle surface is presented in Figure 32. At pH ~ 2,

zeta potential was near zero which indicates low stability by electrostatic repulsion because at this pH the carboxylic groups of the silane were protonated.

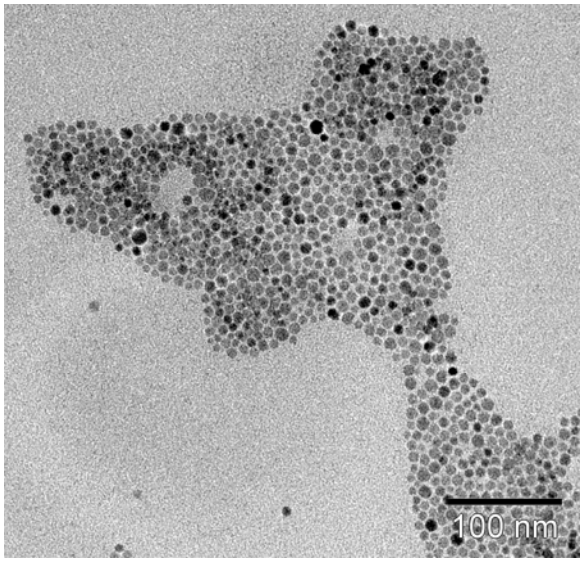

Figure 30: TEM image of cobalt-substituted ferrite nanoparticles functionalized with COO^--silane.

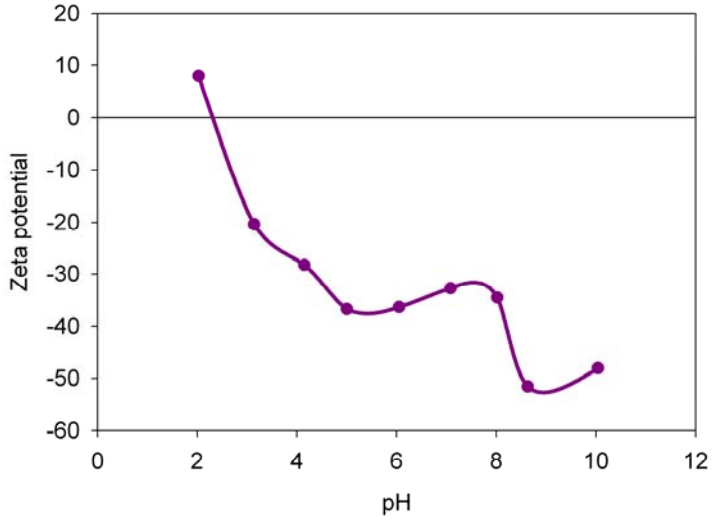

Figure 31: Zeta potential of COO^- -silane nanoparticles suspended in water.

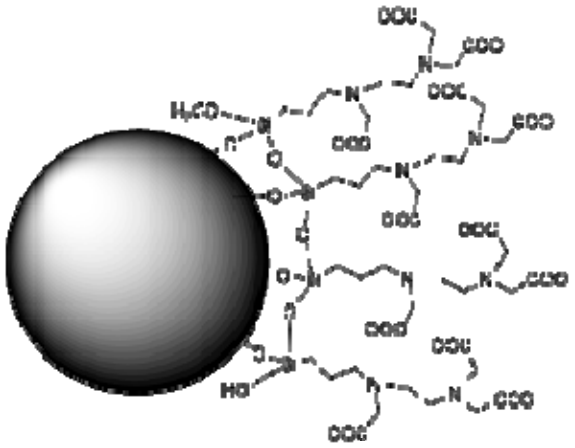

Figure 32 : Schematic representation of nanoparticles functionalized with N-(trimethoxysilylpropyl)ehtylenediamine triacetic acid

7.2. Cobalt ferrite nanoparticles used as sensors

Because magnetic nanoparticles posses field dependent magnetic and optical properties, they are of recent interest in development of nanosensors where analyte specificity is achieved by proper funtionalization of the particle surface. A magnetic response makes these suspensions specially suitable in applications where optical response is undesirable, such as in biological assays where the medium under study is typically turbid. Furhtermore, state-of-the art magnetometric technology, such as Supeconducting Quantum Interferece Devices (SQUIDs), makes detection of femtomole amount of analytes possible.

Table 7-1 shows a literature review of magnetic nanoparticles used to detection of biomolecules. One of advantages to use AC susceptibility is that sample not need to be optical transparent like MRI image. Astalan et al {Astalan, 2004 #51} used AC

susceptibility measurement to detect prostate specific antigen. The shift of out-of-phase component peak was attributed to increase of the particle diameter by PSA attachment but no measurements of hydrodynamic diameter were done to confirm the PSA attachment. Fornara et al {Fornara, 2008 #79} used both AC susceptibility and light scattering measurements to detect Brucella antibodies. The shift of out-of-phase component was attributed to increasing of hydrodynamic diameter of the particle by Brucella antibodies attachment which was confirmed by light scattering technique.

Table 7-1: Literature review of magnetic nanoparticles used as sensors

	Particles	analyte	Method
Halbreich et al (1998)	AnnexinV-Fe_2O_3	Phosphatidylserine on mouse blood cells (cerebral malaria)	Magnetic separation
Astalan et al (2004)	antiPSA-Fe_3O_4	prostate specific antigen (PSA)	Out-of-phase component
Chung et al (2005)	Avidin-Fe_3O_4	S-protein	Out-of-phase component
Hung et al (2005)	Heceptin-Fe_3O_4	HER2/neu receptor of breast cancer cells	MRI image
Fornara et al (2008)	Lipopolysaccarides-Fe_3O_4	Brucella antibodies	Out-of-phase component DLS

Both works, Fornara {Fornara, 2008 #79} and Astalan {Astalan, 2004 #51}, were qualitative analysis. In this work, we present AC susceptibility measurements as an alternative technique to detect biomolecules through qualitative and quantitative analysis.

In order to use cobalt-substituted nanoparticles as a sensor, avidin was used as analyte. In this case, biotin-avidin complex was used due to bound between biotin-avidin is strong and it complex is highly reported in the literature as link between proteins.

7.2.1. AC susceptibility measurements.

As mentioned in Chapter 3, the relaxation of magnetic nanoparticles can be characterized by Brownian and Néel relaxation. In the case of cobalt ferrite nanoparticles, whose anisotropy constant is high, it is expected that only the Brownian mechanism will be active. The Brownian relaxation time depends of the hydrodynamic diameter of the particle, therefore, an increase in the hydrodynamic diameter causes an increase in the Brownian relaxation time.

The Brownian relaxation time can be determined using AC susceptibility measurements. The out-of-phase component of the dynamic susceptibility can be used to determine the relaxation time because $\Omega\tau = 1$ at the peak of a frequency sweep [86]. A shift of the peak to lower frequencies will be observed in response to an increase of the Brownian relaxation time caused by an increase in the hydrodynamic diameter of the nanoparticle (Figure 33).

At high frequencies, equation (7) could be reduced to

$$\chi'' = \frac{\chi_0}{\Omega\tau} \tag{13}$$

whereas at low frequencies it is given by

$$\chi'' = \chi_0 \Omega \tau \tag{14}$$

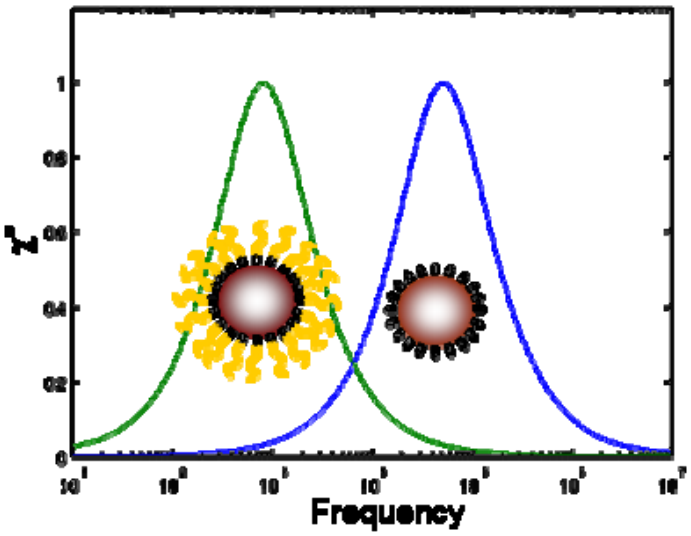

Figure 33: Frequency depend out-of-phase component of dynamic susceptibility for particles with 20 and 80 nm.

If a fixed frequency is considered in both cases, equation (14) indicates than at high frequencies, a decrease of χ'' with hydrodynamic diameter must be expected whereas equation (15) reveals an increase of χ'' with hydrodynamic diameter at low frequencies.

Based on the hydrodynamic diameter-dependence of the χ" vs. frequency curve, magnetic nanoparticles could be use as sensors. In this case, magnetic nanoparticles must be functionalized with a molecule that is specific to the analyte to be detected. When the functionalized nanoparticles are put in contact with the analyte solution, the analyte will

attach to the magnetic nanoparticle increasing its hydrodynamic diameter and therefore increasing its Brownian relaxation time. This change in the Brownian relaxation time can be observed through of the out-of-phase component of dynamic susceptibility measured wit a frequency sweep. A shift of the peak will be observed. The change in the Brownian relaxation time can also be observed by measurement of the out-of-phase component of dynamic susceptibility at a constant frequency. As mentioned above, at high frequencies decrease in the out-of-phase component with increasing hydrodynamic diameter is expected, whereas at low frequencies an increase in the out-of-phase component should be observed. This technique has the advantage that a change in the out-of-phase component can be observed in a few minutes (~ 20 min) whereas using the frequency sweep the change can only observed after some hours (~ 2 to 4 hours).

7.2.2. Biotin-avidin complex

Biotin-avidin complex is the strongest known noncovalent, biological interaction between protein (avidin) and ligand (biotin or vitamin H). Its bond is formed very rapidly and is unaffected by pH, temperature under 100 ºC, and denaturing agents. Due to its strong bond, this complex has been used for chromatography, cytochemistry, immunoassays, sensors, crosslinking, drug delivery, and immobilization, among others.

Avidin is a glycoprotein originally isolated from chicken egg white. Avidin contains four identical subunits with a total mass of 67000-68000 daltons. Each subunit consists of 128 amino acids and binds to one molecule of biotin [87].

Biotin is a 244 dalton vitamin found in all living cells. It binds with high affinity to avidin. Biotin is a relatively small molecule which can be conjugated to many proteins without significantly altering their biological activity.

In order to use biotin for the applications mentioned above, biotin has been coupled to low-or-high molecular weight molecules (biotinylation reagents) without affecting its affinity to avidin. This coupling is done through the carboxyl group of the valeric acid side chain without modifying the bicyclic ring system which is required for recognition by avidin (see Figure 34) [87, 88].

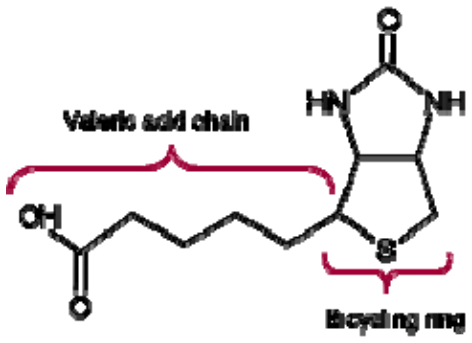

Figure 34: Biotin molecule

One of those biotinylation reagents is amide PEG_2 Biotin (APEGB Figure 36). APEGB is a biotin derivative which can be used to target carboxyl groups on

macromolecules through an amide linkage; it is a water-soluble and amine-reactive biotinylation reagent that contains an extended, hydrophilic spacer arm. The hydrophilic polyethylene oxide (PEO) spacer arm gives it water solubility that is transferred to the biotinylated molecule. The PEO present in APEGB also gives this reagent a long and flexible connection to minimize steric hindrance involved with binding to avidin molecules.

In the process of biotinylation, the amine group reacts with carboxylic groups to form an amide linkage. The reaction between amine and carboxylic group is mediated by 1-ethyl-3-(3-dimethylaminopropyl) carbodiimide (EDC). EDC is a zero-length cross-linking agent that reacts with a carboxyl to form an amine-reactive O-acylisourea intermediate (Figure 35). This intermediate may react with an amine group to form a stable amine bond. In the case that an amine group is not present in the solution, the intermediate hydrolyzes and regenerates the carboxyl group [89, 90].

7.2.3. Materials

EZ link$^{@}$ amide PEG_2 Biotin (APEGB), 1-ethyl-3-(3-dimethylaminopropyl) carbodiimide (EDC), avidin, and dialysis cartridges from Fisher Scientific. Deionized water (0.05 uS/cm) was obtained by treatment (Barnstead Nanopure Diamond).

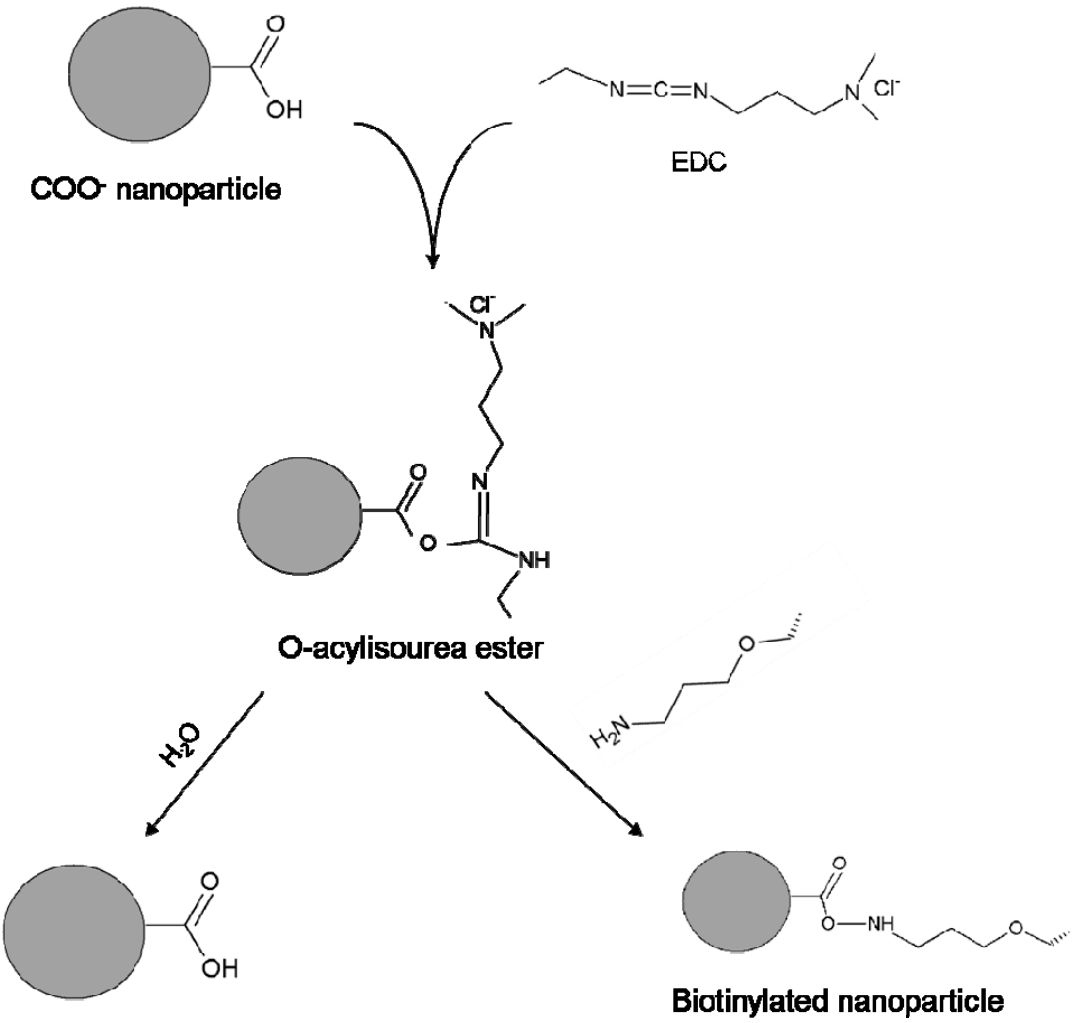

Figure 35: Schematic of mediation of EDC for formation of bond between amide and carboxylic group.

7.2.4. Procedure

a) Biotinylation

An aqueous solution of COO^- -silane nanoparticles (2 mg/ml) was prepared in DI water. Then 5 ml of this solution was mixed with 0.6 ul of APEGB solution and 0.3 ul of

EDC solution previously prepared as follows. A mass of 19 mg of APEGB (or EDC) were dissolved in 1 ml of DI water. The solution was stirred until APEGB (or EDC) was completely dissolved. The particle mixture was incubated for 48 hours at room temperature. Then a dialysis process was done for 48 hours to eliminate the APEGB not attached to COO^- -silane nanoparticles. A schematic of the attachment is presented in Figure 36.

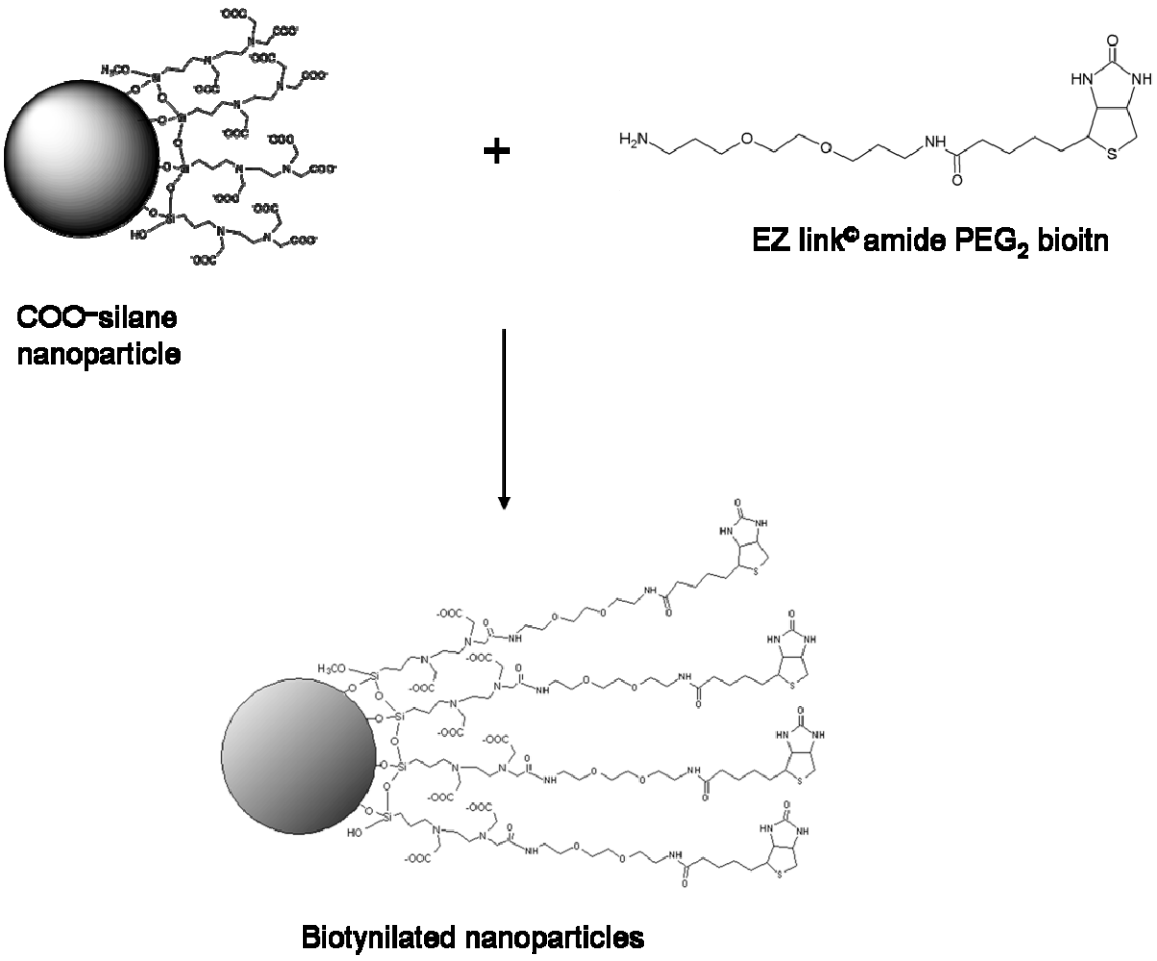

Figure 36: Schematic representation of biotinylation of COO- -silane nanoparticles.

b) Formation of biotin-avidin complex

Biotinylated nanoparticle solution (3 ml at ~0.005 mg_{Fe}/ml) was mixed with 100 μl of avidin solution (~2 mg/ml). The solution was mixed by inversion and rested to permit complex formation. This sample was used for DLS measurements.

In the case of AC susceptibility measurements 100 μl of biotinylated nanoparticles solution at 0.06 mg_{Fe}/ml were mixed with 4 μl of avidin solution at 2 mg/ml. The concentration of avidin in the final solution is approximately 1 μM and roughly 8 μg of protein were used.

7.2.5. Results

DLS data (Table 7-2) showed an increase of hydrodynamic diameter of 2 nm which was attributed to biotinylation of COO^- -silane nanoparticles. When attaching APEGB, whose length is ~ 1nm an increase of ~2 nm in hydrodynamic diameter is expected. Consistent with DLS measurements. There was no change in the sample polydispersity after biotinylation which demonstrated that the attachment of APEGB did not induce particle agglomeration, which was also confirmed by TEM (Figure 37).

Table 7-2: Hydrodynamic diameter of cobalt-substituted nanoparticles before and after biotinylation

	Biotinylation	
D (nm)	Before	After
Number	16.0	18.4
Area	23.5	25.8
Volume	28.6	30.6
Intensity	46.3	46.9
Polydispersity	0.23	0.21

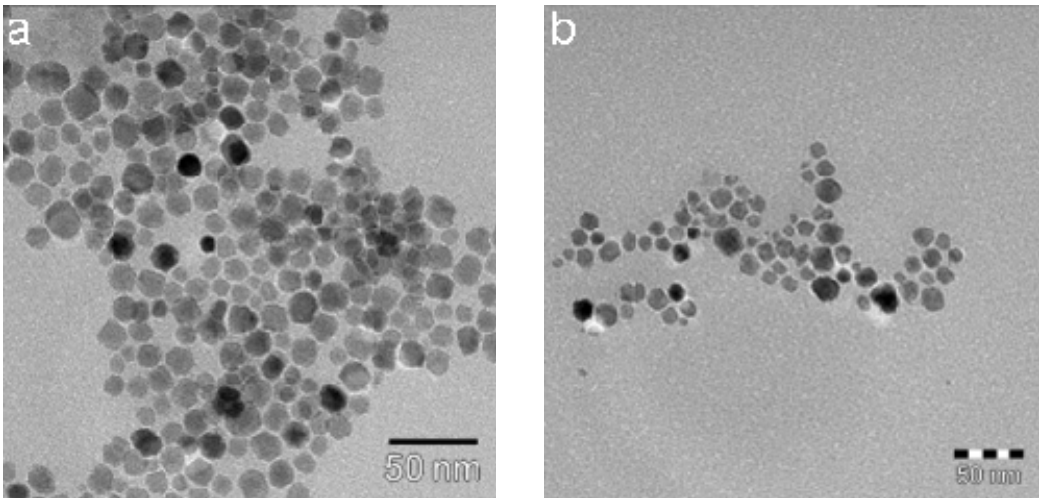

Figure 37: TEM images of COO- -silane nanoparticles a) before and b) after botinylation

The biotinylated nanoparticles were used to detect avidin in solution. Dynamic light scattering showed an increase in the hydrodynamic diameter (Figure 38) with time after addition of avidin solution. The inset of Figure 38 shows two images of particle suspension before (t = 0 hours) and 240 hours after addition of avidin. Completely precipitated nanoparticles were observed after 10 days whereas biotinylated nanoparticles

without avidin were stable for months. The precipitation of the nanoparticles was attributed to increase of the hydrodynamic diameter of the nanoparticles (D > 1000 nm).

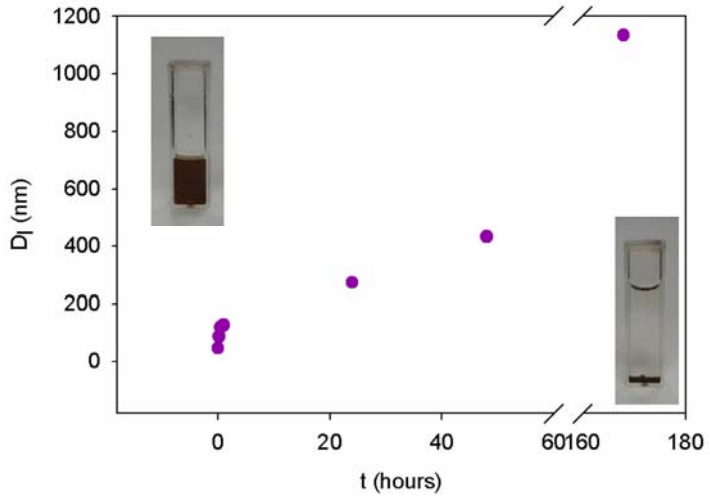

Figure 38: Hydrodynnamic diameter change after addition of avidin.

AC susceptibility measurements were done before and after addition of avidin. In this case, only 100 µl of biotinylated nanoparticles solution were necessary for the measurement. First, out-of-phase component change with time was measured at 100 Hz.

Equation (14) reveals that upon increasing the hydrodynamic diameter of the particle the Brownian relaxation time τ increases, consequently χ'' decreases. Therefore, after addition of avidin a decrease in χ'' with time was expected. Figure 39a shows the change in out-of-phase component with time. As expected, a decrease of χ'' with time was observed which confirmed the attachment of avidin to biotinylated nanoparticles.

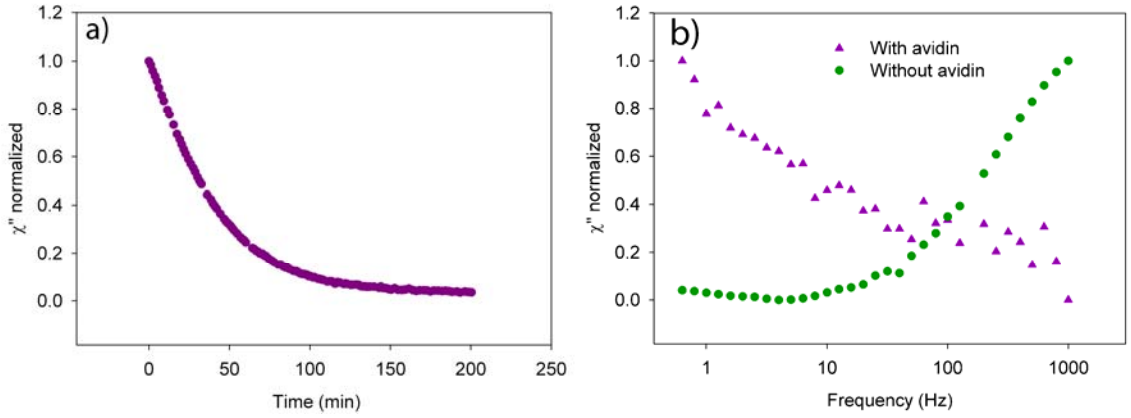

Figure 39: AC measurements a) out-of-phase component of dynamic susceptibility change with frequency before and after addition of avidin b) change of out-of-phase component of dynamic susceptibility at 100 Hz with time after addition of avidin.

The out-phase component was also measured with frequency (see Figure 39b). The peak of χ'' vs frequency curve of biotinylated nanoparticles was not observed between 1 and 1000 Hz. But an increase of χ'' with frequency could be observed. This indicated that the peak of χ'' vs. frequency was a higher frequencies due to relaxation time of nanoparticles with ~20 nm diameter was in the range of kHz. After the addition of avidin, the peak of χ'' vs frequency was not observed. In contrast with the biotinylated nanoparticles, a decrease of χ'' with increasing frequency was observed. This means that the χ'' peak was at a frequency lower than 1 Hz which corresponds to relaxation of nanoparticles with diameter higher than ~100 nm. Therefore, the shift of out-of-phase component after addition of avidin was attributed to an increase of the Brownian relaxation time of the biotinylated nanoparticles because of attachment of avidin molecules.

The out-of-phase component of the dynamic susceptibility measurement could be used to detect a change in the hydrodynamic diameter of biotinylated nanoparticles caused by avidin attachment. Only a small amount of biotinylated nanoparticles solution (~100 μl at 0.06mg_{Fe}/l) was necessary to determine the presence of avidin in solution at a concentration of ~1 μM whereas a short time of detection was used when the change of out-of-phase component with time at a fix frequency was measured. This demonstrated that an AC susceptibility measurement is a good and fast alternative method to detect biomolecules.

7.3. Conclusions

Water soluble and non-agglomerated nanoparticles were obtained via ligand exchange between oleic acid and COO-silane. Fourier transform infrared confirmed the nanoparticle surface was coated with COO-silane molecules after the ligand exchange process. COO-silane nanoparticles were stable in a wide range of pH (3-10) which was revealed by zeta potential analysis. This stability permits using COO-silane nanoparticles in biological applications. Additionally, precipitates were not observed for various months indicating high stability in aqueous solutions given by carboxylic groups.

In this work, cobalt ferrite nanoparticles coated with COO-silane agent were biotinylated to detect avidin in aqueous solution using AC susceptibility measurements. After addition of biotinylated nanoparticles to an avidin solution, an increase in the Brownian relaxation time was observed by AC susceptibility measurements. This

increase was caused by an increase in the hydrodynamic diameter because of attachment of avidin molecules. An alternative technique to detect biomolecules using small amount of sample and short measurement time and a sensitivity of 2 μM was demonstrated.

BIBLIOGRAPHY

[1] T. Hyeon, "Chemical synthesis of magnetic nanoparticles," *Chemical Communications*, pp. 927-934, 2003.

[2] I. Safarik and M. Safarikova, "Magnetic nanoparticles and biosciences," *Monotshefte fut Chemie*, vol. 133, pp. 737, 2002.

[3] W. Callister, *Materials science and engineering an introduction*, Sixth ed. New York, 2003.

[4] N. Spaldin, *Magnetic Materials: Fundamentals and device applications*. Cambridge: Cambridge University press, 2003.

[5] R. M. Bozorth, *Ferromagnetism*. New york: Editorail Board, 1993.

[6] R. E. Rosensweig, *Ferrohydrodynamics*. Mineola, New York: Dover Publications, INC, 1985.

[7] G. D. Moeser, K. A. Roach, W. H. Green, P. E. Laibinis, and T. A. Hatton, "Water-based magnetic fluids as extractants for synthetic organic compounds," *Industrial & Engineering Chemistry Research*, vol. 41, pp. 4739-4749, 2002.

[8] P. A. Voltairas, D. Fotiadis, and L. Michalis, "Hydrodynamics of magnetic drug targeting," *Journal of Biomechanics*, vol. 35, pp. 813, 2002.

[9] C. Alexiou, A. Schmidt, R. Klein, P. Hulin, C. Bergemann, and W. Arnold, "Magnetic drug targeting: biodistribution and dependency on magnetic field strength*1," *Journal of Magnetism and Magnetic Materials*, vol. 252, pp. 363-366, 2002.

[10] A. Halbreich, E. V. Groman, D. Raison, C. Bouchaud, and S. Paturance, "Damage to the protein synthesizing apparatus in mouse liver in vivo by magnetocytolysis in the presence of hepatospecific magnetic nanoparticles," *Journal of Magnetism and Magnetic Materials*, vol. 248, pp. 276-285, 2002.

[11] M. Berger, J. Castelino, R. Huang, M. Shah, and R. H. Austin, "Design of an microfabricated magnetic cell separator," *Electrophoresis*, vol. 22, pp. 3883, 2001.

[12] V. Calero-DdelC, C. Rinaldi, and M. Zahn, *Magnetic fluid and nanoparticle based sensors*, vol. 5: C.A. Grimes, E.C. Dickey, and M.V. Pishko, Eds: American Scientific Publishers, 2006.

[13] J. Connolly and T. G. St Pierre, "Proposed biosensors based on time-dependent properties of magnetic fluids," *Journal of Magnetism and Magnetic Materials*, vol. 225, pp. 156-160, 2001.

[14] L. D. Tung, V. Kolesnichenko, D. Caruntu, N. H. Chou, C. J. O'Connor, and L. Spinu, "Magnetic properties of ultrafine cobalt ferrite particles," *Journal of Applied Physics*, vol. 93, pp. 7486-7488, 2003.

[15] A. Goldman, *Modern Ferrite Technology*. New York, 1990.

[16] C. R. Lin, R. K. Chiang, J. S. Wang, and T. W. Sung, "Magnetic properties of monodisperse iron oxide nanoparticles," *Journal of Applied Physics*, vol. 99, pp. 08N710, 2006.

[17] M. Nikolo, "Superconductivity: A guide to alternating current susceptibility measurements and alternating current susceptometer design," *American Journal of Physics*, vol. 63, pp. 57-65, 1995.
[18] M. I. Youssif, A. A. Bahgat, and I. A. Ali, "AC magnetic susceptibility technique for the characterization of high temperature superconductors," *Egyptian Journal of Solids*, vol. 23, pp. 231-250, 2000.
[19] P. Vanderbemden, "Design of an A.C. susceptometer based on a cryocooler," *Cryogenics*, vol. 38, pp. 839-842, 1998.
[20] J. Park, K. An, Y. Hwang, J. G. Park, H. J. Noh, J. Y. Kim, J. H. Park, N. M. Hwang, and T. Hyeon, "Ultra-large-scale syntheses of monodisperse nanocrystals," *Nature Materials*, vol. 3, pp. 891-895, 2004.
[21] M. F. Casula, Y. Jun, D. J. Zazisky, E. M. Chan, A. Corrias, and A. P. Alivisatos, "The concept of delayed nucleation in nanocrystal growth demonstrated for the case of Iron oxide nanodisks," *Journal of the American Chemical Society*, vol. 128, pp. 1675-1682, 2006.
[22] C. B. Murray, S. Sun, H. Doyle, and T. Betley, "Monodisperse 3d transition-metal (Co, Ni, Fe) nanoparticles and their assembly into nanoparticle superlattices," *MRS Bulletin*, vol. 12, pp. 985-991, 2001.
[23] A. C. S. Samia, J. A. Schlueter, J. S. Jiang, S. D. Bader, C. J. Qin, and X. M. Lin, "Effect of ligan-metal interactions on the growth of transition-metal and alloy nanoparticles," *Chemical of Materials*, vol. 18, pp. 5203-5212, 2006.
[24] M. Yin, A. Willis, F. Redl, N. J. Turro, and S. P. O'Brien, "Influence of capping groups on the synthesis of g-Fe2O3 nanocrystals," *Journal of Materials Research*, vol. 19, pp. 1208-1215, 2004.
[25] S. Sun and C. B. Murray, "Synthesis of monodisperse cobalt nanocrystals and their assembly into magnetic superlaticces," *Journal of Applied Physics*, vol. 85, pp. 4325-4330, 1999.
[26] T. Hyeon, Y. Chung, J. Park, S. S. Lee, Y.-W. Kim, and B. H. Park, "Synthesis of highly crystalline and monodisperse cobalt ferrite nanocrystals," *Journal of Physical Chemistry B*, vol. 106, pp. 6831-6833, 2002.
[27] S. Sun, H. Zeng, D. B. Robinson, S. Raoux, P. M. Rice, S. X. Wang, and G. Li, "Monodisperse MFe_20_4 (M = Fe, Co, Mn) nanoparticles," *Journal of the American Chemical Society*, vol. 126, pp. 273-279, 2004.
[28] A. G. Roca, M. P. Morales, K. O'grady, and C. J. Serna, "Structural and magnetic properties of uniforma magnetite nanoparticles prepared by high temperature decomposiitonof organic precursors," *Nanotechnology*, vol. 17, pp. 2783-2788, 2006.
[29] E. Kang, J. Park, Y. Hwang, M. Kang, J. G. Park, and T. Hyeon, "Direct synthesis of highly crystalline and monodisperse manganese ferrite nanocrystals," *Journal Of Physical Chemistry B*, vol. 108, pp. 13932-13935, 2004.
[30] L. Zhang, R. He, and H. C. Gu, "Oleic acid coating on the monodisperse magnetite nanoparticles," *Applied Surface Science*, vol. 253, pp. 2611-2617, 2006.
[31] J. Lange, R. Kotitz, A. Haller, L. Trahms, W. Semmler, and W. Weitschies, "Magnetorelaxometry - a new binding specific detection method based on

magnetic nanoparticles," *Journal of Magnetism and Magnetic Materials*, vol. 252, pp. 381-383, 2002.

[32] J. Connolly and T. G. Pierre, "Proposed biosensors based on time-dependent properties of magnetic fluids," *Journal of Magnetism and Magnetic Materials*, vol. 225, pp. 156-160, 2001.

[33] S. H. Chung, A. Hoffmann, K. Guslienko, S. D. Bader, C. Liu, B. Kay, L. Makowski, and L. Chen, "Biologial sensing with magnetic nanoparticles using Brownian relaxation," *Journal of Applied Physics*, vol. 97, pp. 10R101, 2005.

[34] A. Fornara, P. Johansson, K. Petersson, S. Gustafsoon, J. Qin, E. Olsson, D. Ilver, A. Krozer, M. Muhammed, and C. Johansson, "Tailored magnetic nanoparticles for direct and sensitive detection of biomolecules in biological samples," *Nano Letters*, vol. 8, pp. 3423-3428, 2008.

[35] G. Salazar-Alvarez, R. T. Olsson, J. Sort, W. A. A. Macedo, J. D. Ardisson, M. D. Baro, U. W. Gedde, and J. Nogues, "Enhanced coercivity in Co-Rich Near-stoichiometric $Co_xFe_{3-x}O_{4+\delta}$ nanoparticles prepared in large batches," *Chemistry of Materials*, vol. 19, pp. 4957-4963, 2007.

[36] S. K. Sharma, R. Kumar, S. Kumar, M. Knobel, C. T. Meneses, V. V. Siva Kumar, V. R. Reddy, M. Singh, and C. G. Lee, "Role of interparticle interactions on the magnetic behavior of $Mg_{0.95}Mn_{0.05}Fe_2O_4$ ferrite nanoparticles," *Journal of Physics: Condensed Matter*, vol. 20, pp. 235214, 2008.

[37] Y. Lee, J. Lee, C. J. Bae, J. G. Park, H. J. Noh, J. H. Park, and T. Hyeon, "Large-scale synthesis of uniform and crystalline magnetite nanoparticles using reverse micelles as nanoreactors under reflux conditions," *Advanced Functional Materials*, vol. 15, pp. 503-509, 2005.

[38] A. D. Arelaro, E. Lima Jr., L. M. Rossi, P. K. Kiyohara, and H. R. Rechenberg, "Ion dependence of magnetic anisotropy in MFe_2O_4 (M=Fe, Co, Mn) nanoparticles synthesized by high-temperature reaction," *Journal of Magnetism and Magnetic Materials*, vol. 320, pp. e335-e338, 2008.

[39] W. W. Yu, F. J.C., C. T. Yavuz, and V. L. Colvin, "Synthesis of monodisperse iron oxide nanocrystals by thermal decomposition of iron carboxylate salts," *Chemical Communication*, pp. 2306-2307, 2004.

[40] E. V. Shevchenko, D. V. Talapin, H. Schnablegger, A. Kornowski, O. Festin, P. Svedlindh, M. Hasase, and H. Weller, "Study of nucleation and growth in the organometallic synthesis of magnetic alloy nanocrystals: The role of nucleation rate in size control of $CoPt_3$ nanocrystals," *Journal of the American Chemical Society*, vol. 125, pp. 9090-9101, 2003.

[41] Y. Chen, X. Luo, G. H. Yue, X. Luo, and D. L. Peng, "Synthesis of iron-nckel nanoparticles via a nonaqueous organometallic route," *Materials Chemistry and Physics*, vol. 113, pp. 412-416, 2009.

[42] C. A. Crouse and A. R. Barron, "Reagent control over the size, uniformity, and composition of Co-Fe-O nanoparticles," *Journal of Materials Chemistry*, vol. 18, pp. 4146-4153, 2008.

[43] C. Srivastava, D. E. Nikles, and G. B. Thompson, "Compositional evolution during the synthesis of FePt nanoparticles," *Journal of Applied Physics*, vol. 104, pp. 064315, 2008.

[44] N. Shukla, E. B. Svedberg, J. Ell, and A. J. Roy, "Surfactant effects on the shapes of cobalt nanoparticles," *Materials Letters*, vol. 60, pp. 1950-1955, 2006.
[45] G. Leem, S. Sarangi, S. Zhang, I. Rusakova, A. Brazdeikis, D. Litvinov, and L. T.R., "Surfactant-controlled size and shape evolution of magnetic nanoparticles," *Crystal Growth & Design*, vol. 9, pp. 32-34, 2009.
[46] Y. Lu, X. Lu, B. T. Mayers, T. Herricks, and Y. Xia, "Synthesis and characterization of magnetic Co nanoparticles: A comparison study of three different capping surfactants," *Journal of Solid State Chemistry*, vol. 181, 2008.
[47] X. Teng and H. Yang, "Effects of surfactants and synthetic conditions on the sizes and self-assembly of monodisperse iron oxide nanoparticles," *Journal of Materials Chemistry*, vol. 14, pp. 774-779, 2004.
[48] J. Xie, S. Peng, N. Brower, N. Pourmand, S. X. Wang, and S. Sun, "One-pot synthesis of monodisperse iron oxide nanoparticles for potential biomedical applications," *Pure and Applied Chemistry*, vol. 78, pp. 1003-1014, 2006.
[49] H. Gu, K. Xu, C. Xu, and B. Xu, "Biofunctional magnetic nanoparticles for protein separation and pathogen detection," *Chemical Communications*, pp. 941-949, 2006.
[50] A. Hoshino, N. Ohmishi, M. Yasuhara, K. Yamamoto, and A. Kondo, "Separation of murine neutrophils and macrophages by thermoresponsive magnetic nanoparticles," *Biotechnology Progress*, vol. 23, pp. 1513-1516, 2007.
[51] N. T. Phan, C. S. Gill, J. V. Nguyen, Z. J. Zhang, and C. W. Jones, "Expanding the utility of one-pot multistep reaction networks through compartmentation and recovery of the catalyst," *Angewandte Chemie-International Edition*, vol. 45, pp. 2209-2212, 2006.
[52] H. Yoon, S. Ko, and J. Jang, "Nitrogen-doped magnetic carbon nanoparticles as a catalyst supports for efficient recovery and recycling," *Chemical Communications*, pp. 1468-1470, 2007.
[53] A. Kuzubou and O. Ivanova, "Magnetic liquids for heat-exchange," *Journal de Physique III France*, vol. 4, pp. 1-6, 1994.
[54] V. K. Pecharsky and K. A. Gschneidner Jr, "Magnetocaloric effect and magnetic refrigeration," *Journal of Magnetism and Magnetic Materials*, vol. 200, pp. 44-56, 1999.
[55] I. Hilger, R. Hergt, and W. A. Kaiser, "Towards breast cancer treatment by magnetic heating," *Journal of Magnetism and Magnetic Materials*, vol. 293, pp. 314-319, 2005.
[56] R. Hiergeist, W. Andra, N. Buske, R. Hergt, I. Hilger, U. Richter, and W. Kaiser, "Application of magnetic ferrofluids for hyperthermia," *Journal of Magnetism and Magnetic Materials*, vol. 210, pp. 420-422, 1999.
[57] J. M. Perez, L. Josephson, T. O'Loughlin, D. Hogemann, and R. Weissleder, "Magnetic relaxation switches capable of sensing molecular interactions," *Nature Biotechnology*, vol. 20, pp. 816-820, 2002.
[58] C. B. Kriz, K. Radevik, and D. Kris, "Magnetic permeability measurements in bioanalysys and biosensors," *Analitical Chemistry*, vol. 68, pp. 1966, 1996.
[59] S. Shtrikman and E. P. Wohlfarth, "The theory of the Vogel-Fulcher law of spin glasses," *Physics Letters*, vol. 85A, pp. 467-470, 1981.

[60] J. L. Zhang, C. Boyd, and W. L. Luo, "Two mechanisms and a scaling relation for dynamics in ferrofluids," *Physical Review Letters*, vol. 77, pp. 390-393, 1996.
[61] M. Thakur, M. P. Chowdhury, S. Majumdar, and S. Giri, "Dominant dipolar interaction and glassy magnetic behaviour in polymer-coated magnetite nanoparticles," *Nanotechnology*, vol. 19, pp. 045706, 2008.
[62] N. Y. Ayoub, "The effect of dipolar interactions on the susceptibility peaks in a solidified ferrofluid," *Japanese Journal of Applied Physics*, vol. 30, pp. 3381-3385, 1991.
[63] G. A. Held, G. Grinstein, H. Doyle, S. Sun, and C. B. Murray, "Competing interactions in dispersions of superparamagnetic nanoparticles," *Physical Review B*, vol. 64, 2001.
[64] P. Poddar, T. Telem-Shafir, T. Fried, and G. Markovich, "Dipolar interactions in two- and three-dimensional magnetic nanoparticles array," *Physical Review B*, vol. 66, pp. 0604031-0604034, 2002.
[65] W. Luo, S. R. Nagel, T. F. Rosenbaum, and R. E. Rosenweig, "Dipole interaction with random anisotropy in a frozen ferrofluid," *Physical Review Letters*, vol. 67, pp. 2721-2724, 1991.
[66] C. Djurberg, P. Svedlindh, and P. Nordbland, "Dynamics of an interacting particles system: evidence of critical slowing down," *Physical Review Letters*, vol. 79, pp. 5154-5157, 1997.
[67] T. Jonsson, J. Mattsson, C. Djurberg, F. A. Khan, P. Nordbland, and P. Svedlindh, "Aging in a magnetic particle system," *Physical Review Letters*, vol. 75, pp. 4138-4141, 1995.
[68] C. R. Vestal, Q. Song, and Z. J. Zhang, "Effects of interparticles interactions upon the magnetic properties of $CoFe_2O_4$ and $MnFe_2O_4$," *Journal of Physics and Chemistry*, vol. 108, pp. 18222-18227, 2004.
[69] A. F. Lehlooh, S. H. Mahmood, and J. M. Williams, "On the particle size dependence of the magnetic anisotropy energy constant," *Physica B*, vol. 321, pp. 159-162, 2002.
[70] N. Hanh, O. K. Quy, N. P. Thuy, L. D. Tung, and L. Spinu, "Synthesis of cobalt ferrite nanocrystallites by the forced hydrolysis method and investigation of their magnetic properties," *Physica B-Condensed Matter*, vol. 327, pp. 382-384, 2003.
[71] K. J. Davies, S. Well, R. V. Upadhyay, S. W. Charles, K. O'Grady, M. El Hilo, T. Meaz, and S. Morup, "Observation of multi-axial anisotropy in ultrafine cobalt ferrite particles used in magnetic fluids," *Journal of Magnetism and Magnetic Materials*
Proceedings of the 7th International Conference on Magnetic Fluids, Jan 7-14 1995, vol. 149, pp. 14-18, 1995.
[72] A. T. Ngo, P. Bonville, and M. Pileni, "Nanoparticles of $Co_xFe_{y-z}O_4$: Synthesis and superparamagnetic properties," *The European Physical Journal B*, vol. 9, pp. 583-592, 1999.
[73] R. Tackett, C. Sudakar, R. Naik, G. Lawes, C. Rablau, and P. P. Vaishnava, "Magnetic and optical response of tuning the magnetocrystalline anisotropy in Fe3O4 nanoparticle ferrofluids by Co doping," *Journal of Magnetism and Magnetic Materials*, vol. 320, pp. 2755-2759, 2008.

[74] G. Baldi, D. Bonacchi, C. Innocenti, G. Lorenzi, and C. Sangregorio, "Cobalt ferrite nanoparticles: The control of the particle size and surface state and their effects on magnetic properties," *Journal of Magnetism and Magnetic Materials*, vol. 311, pp. 10-16, 2007.

[75] D. Parker, V. Dupuis, F. Ladieu, J. P. Bouchaud, E. Dubois, R. Perzynski, and E. Vincent, "Spin-glass behavior in an interacting y-Fe2)3 nanoparticle systemn," *Physical Review B*, vol. 77, pp. 104428, 2008.

[76] M. Hanson, C. Johansson, M. S. Pedersen, and S. Morup, "The influence of particle size and interactions on the magnetization and susceptibility of nanometer-size particles," *Journal of Physics: Condens: Condensed Matter*, vol. 7, pp. 9269-9277, 1995.

[77] G. F. Goya and M. P. Morales, "Field dependence of blocking temperature in magnetite nanoparticles," *Journal of Metastable and Nanocrystalline Materials*, vol. 20-21, pp. 673-678, 2004.

[78] X. Sun, "Self-assembly of magnetic biofunctional nanoparticles," *Journal Of Applied Physics*, vol. 97, pp. 10Q901, 2005.

[79] S. Sun, H. Zeng, D. B. Robinson, S. Raoux, P. M. Rice, S. X. Wang, and G. Li, "Optical properties of gold colloids formed in reverse micelles," *Journal of Chemical Physics*, vol. 98, pp. 9933-9950, 2004.

[80] K. Woo and J. Jhong, "Surface modification of hydrophobic iron oxide nanoparticles for clinical applications," *Ieee Transactions on Magnetics*, vol. 41, pp. 4137-4139, 2005.

[81] R. De-Palma, S. Peeters, M. J. V.-. Bael, H. Van-Den-Rul, K. Bonroy, W. Laueryn, J. Mullens, G. Borhs, and G. Maes, "Silane ligand exchange to make hydrophobic superparamagnetic nanoparticles water-dispersible," *Chemical Materials*, vol. 19, pp. 1821-1831, 2007.

[82] E. P. Plueddemann, *Silane coupling agents*. New York: Plenum Press, 1982.

[83] A. Halbreich, J. Roger, J. N. Pons, D. Geldwerth, M. F. Da Silva, M. Roudier, and J. C. Bacri, "Biomedical applications of maghemite ferrofluid," *Biochimie*, vol. 80, pp. 379-390, 1998.

[84] Y. M. Huh, Y. W. Jun, H. T. Song, S. J. Kim, J. S. Choi, J. H. Lee, S. Yoon, K. S. Kim, J. S. Shin, J. S. Suh, and J. Cheon, "In vivo magnetic resonance detection of cancer by using multifunctional magnetic nanocrystals," *Journal of the American Chemical Society*, vol. 127, pp. 12387-12391, 2005.

[85] L. Josephson, C. H. Tung, A. Moore, and R. Weissleder, "High-efficiency intracellular magnetic labeling with novel superparamagnetic-tat peptide conjugates," *Bioconjugate Chemistry*, vol. 10, pp. 186-191, 1999.

[86] V. Calero-DdelC and C. Rinaldi, "Synthesis and magnetic characterization of cobalt-substituted ferrite ($Co_xFe_{3-x}O_4$) nanoparticles," *Journal of Magnetism and Magnetic Materials*, vol. 314, pp. 60-67, 2007.

[87] M. D. Savage, *Avidin-Biotin Chemistry: A handbook*. Rockford, IL: Pierce Chemical Co, 1992.

[88] M. Wilchek and E. A. Bayer, "The avidin-biotin complex in bioanalytical applications," *Analytical Chemistry*, vol. 171, pp. 1-32, 1988.

[89] D. Seghal and I. Vijay, "A method for the high efficiency of water-soluble carbodiimide-mediated amidation," *Analytical Biochemistry*, vol. 218, pp. 87-91, 1994.

[90] E. Kynclova, E. Elsner, A. Kopf, G. Hawa, T. Schalkhammer, and F. Pittner, "Novel method for soupling of poly(ethyleneglycol) to carboxylic acid moities of proteins," *Journal of Molecular Recognition*, vol. 9, pp. 644-651, 1996.

APPENDIX A

Characterization of $Co_xFe_{3-x}O_4$ nanoparticles synthesized by thermal-decomposition method described in Chapter 4.

A.1. TEM images and size distribution of $Co_xFe_{3-x}O_4$ nanoparticles synthesized by thermal-decomposition method

Run 1

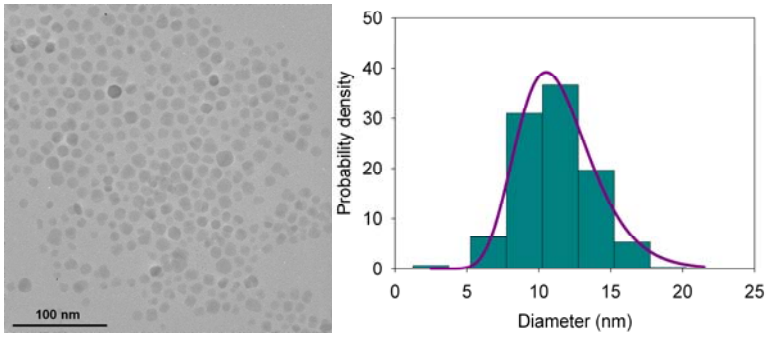

T_1= 250 ºC t_1=120 min T_2=300 ºC t_2=60 min

Run 2

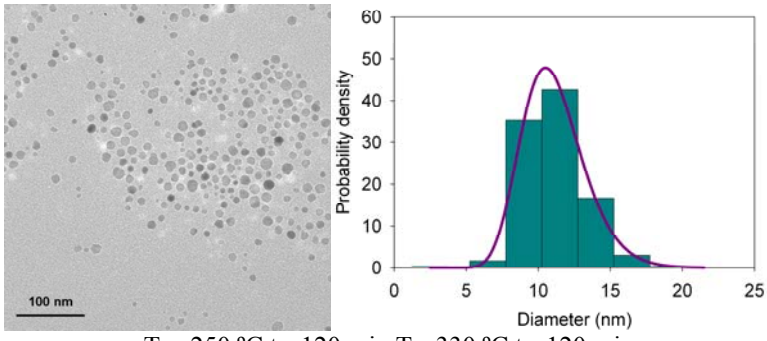

T_1= 250 ºC t_1=120 min T_2=330 ºC t_2=120 min

Run 3

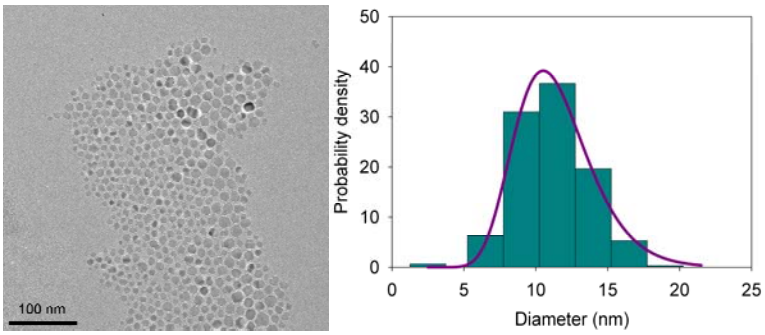

T_1= 150 ºC t_1=120 min T_2=300 ºC t_2=120 min

Run 4

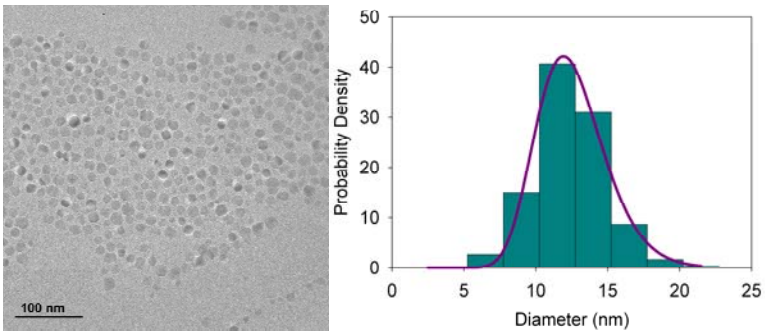

T_1= 200 ºC t_1=90 min T_2=315 ºC t_2=90 min

Run 5

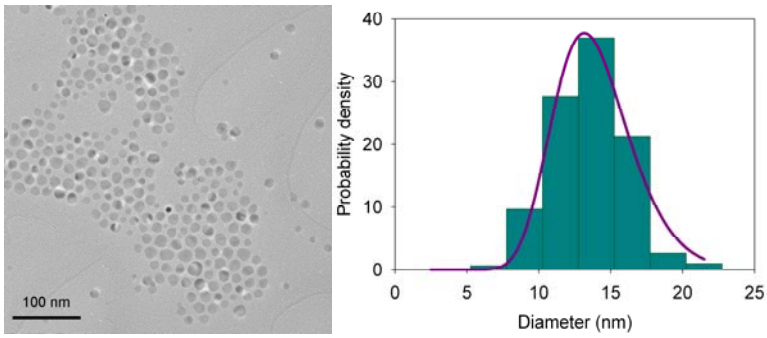

T_1= 150 ºC t_1=120 min T_2=330 ºC t_2=60 min

Run 6

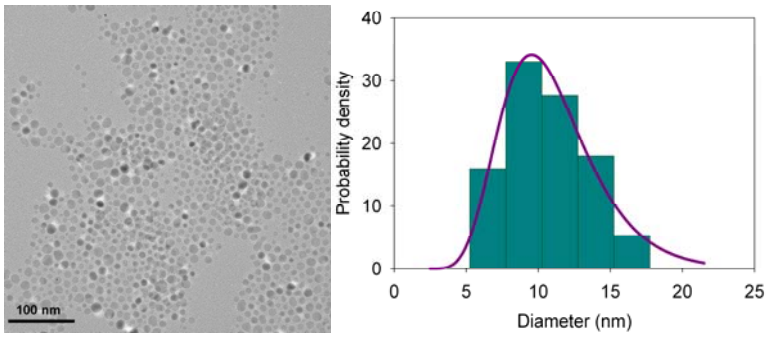

T_1= 250 ºC t_1=60 min T_2=330 ºC t_2=60 min

Run 7

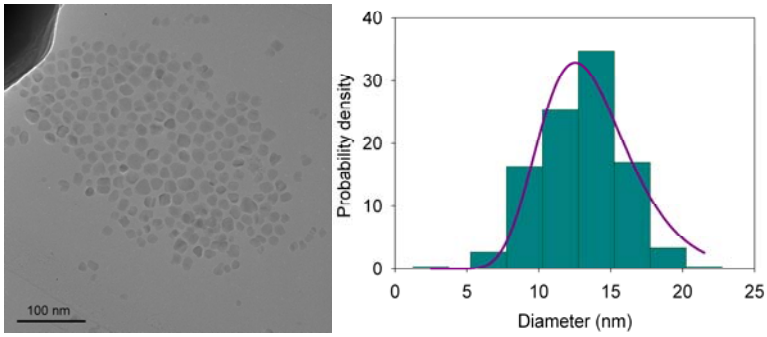

T_1= 250 ºC t_1=60 min T_2=330 ºC t_2=60 min

Run 8

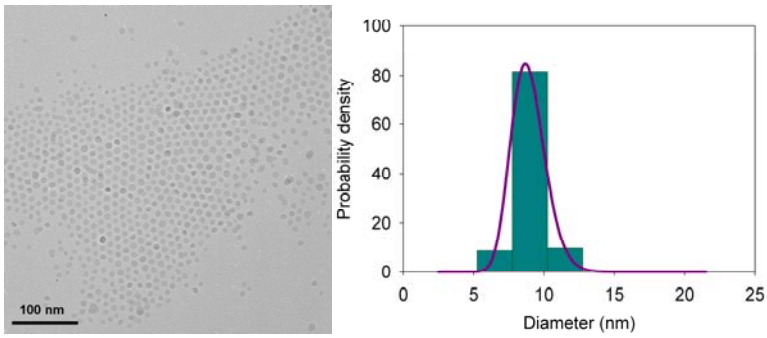

T_1= 250 ºC t_1=60 min T_2=300 ºC t_2=120 min

Run 9

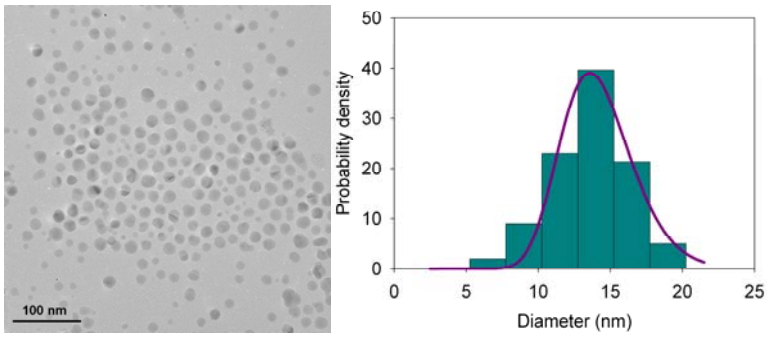

T_1= 150 ºC t_1=60 min T_2=330 ºC t_2=120 min

Run 10

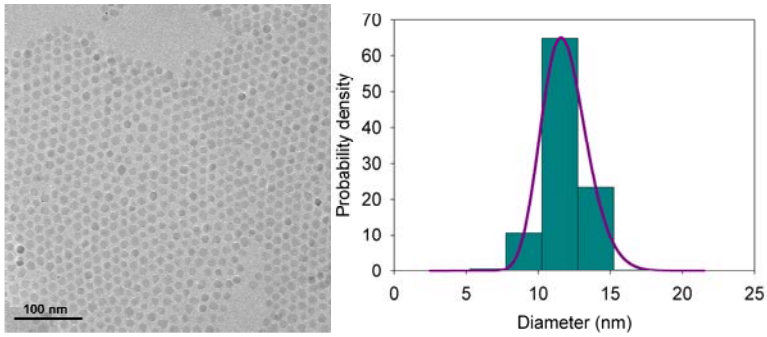

T_1= 150 ºC t_1=60 min T_2=300 ºC t_2=60 min

A.2. X-ray diffraction patterns of $Co_xFe_{3-x}O_4$ nanoparticles synthesized by thermal-decomposition method

Run 1

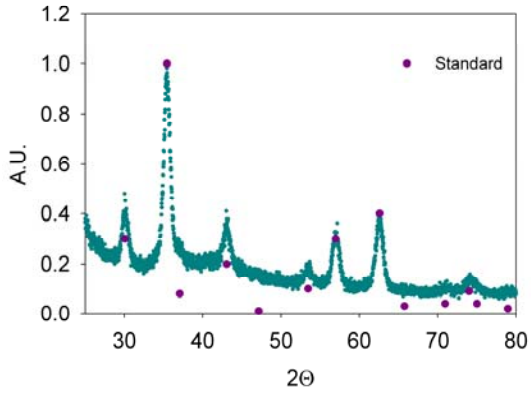

= 250 ºC t_1=120 min T_2=300 ºC t_2=60 min

Run 2

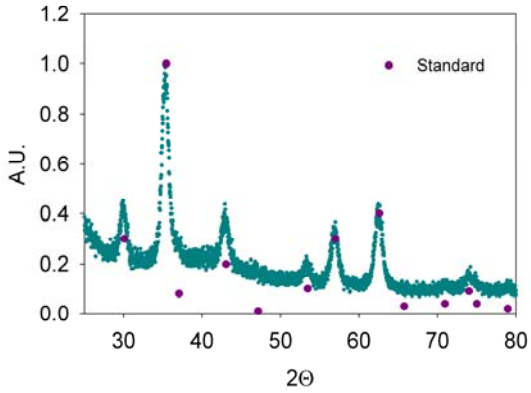

T_1= 250 ºC t_1=120 min T_2=330 ºC t_2=120 min

Run 3

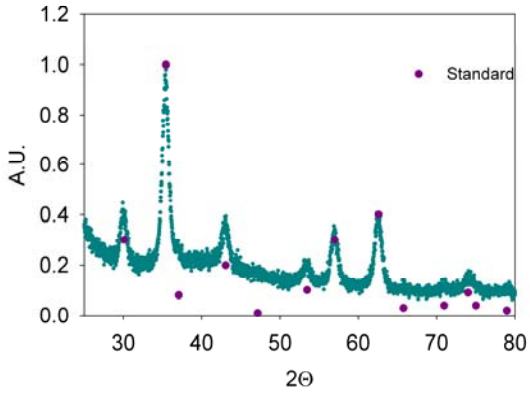

T_1= 150 ºC t_1=120 min T_2=300 ºC t_2=120 min

Run 4

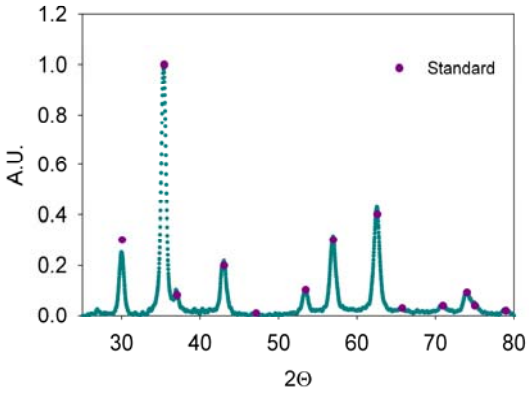

T_1= 200 ºC t_1=90 min T_2=315 ºC t_2=90 min

Run 5

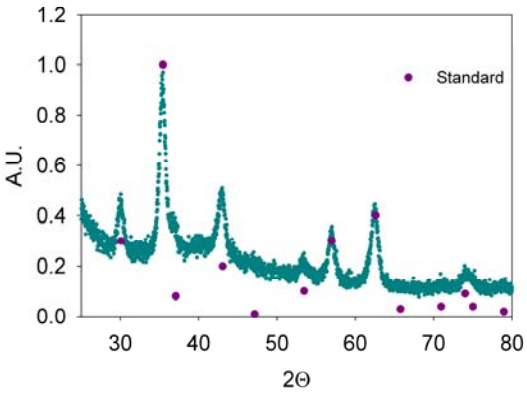

T_1= 150 ºC t_1=120 min T_2=330 ºC t_2=60 min

Run 6

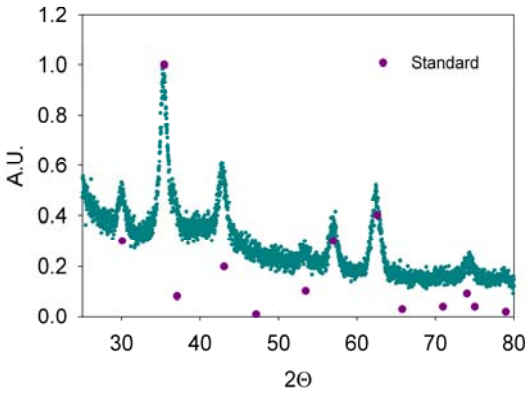

T_1= 250 ºC t_1=60 min T_2=330 ºC t_2=60 min

Run 7

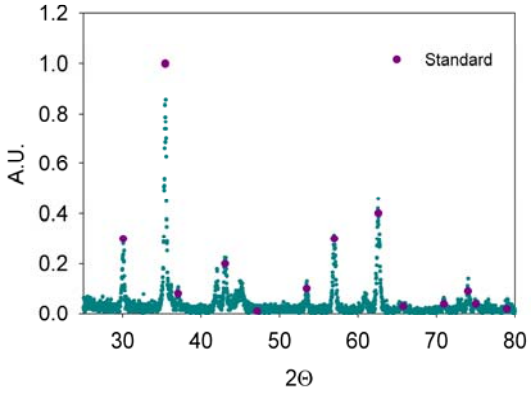

T_1= 200 ºC t_1=90 min T_2=315 ºC t_2=90 min

Run 8

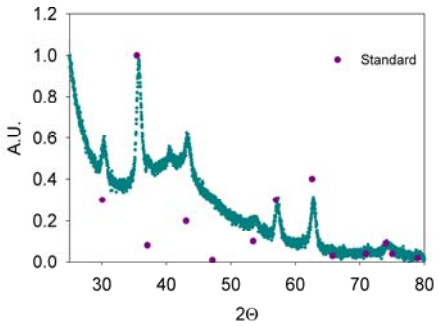

T_1= 250 ºC t_1=60 min T_2=300 ºC t_2=120 min

Run 9

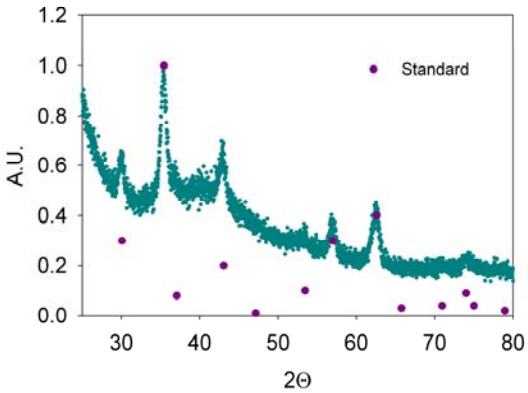

T_1= 150 ºC t_1=60 min T_2=330 ºC t_2=120 min

Run 10

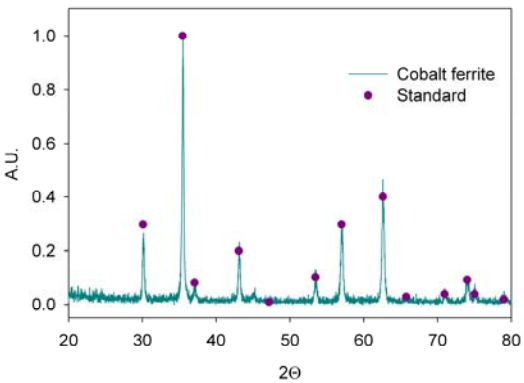

T_1= 150 ºC t_1=60 min T_2=300 ºC t_2=60 min

A.3. Magnetization curves at 5 K and 300 K of $Co_xFe_{3-x}O_4$ nanoparticles fixed in paraffin matrix

Run 1

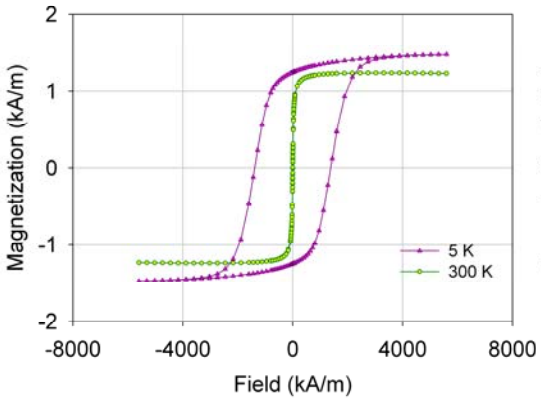

T_1= 250 ºC t_1=120 min T_2=300 ºC t_2=60 min

Run 2

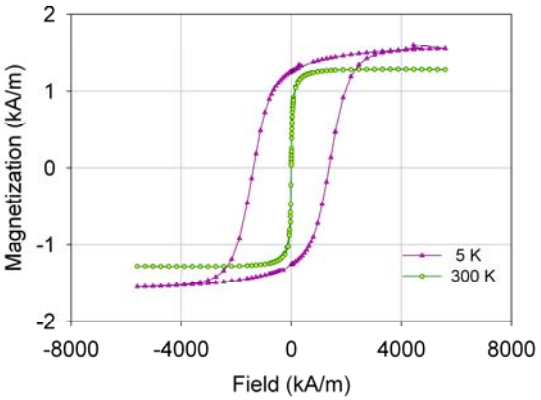

T_1= 250 ºC t_1=120 min T_2=330 ºC t_2=1200 min

Run 3

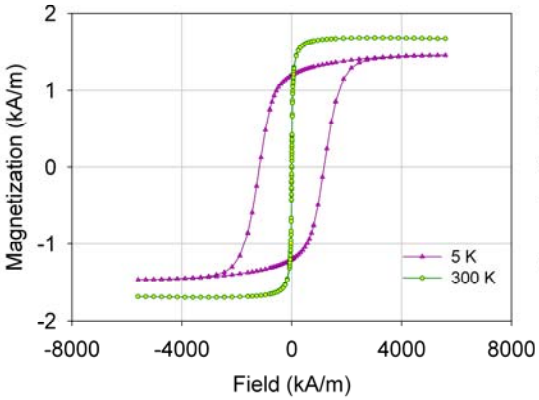

T_1= 150 ºC t_1=120 min T_2=300 ºC t_2=120 min

Run 4

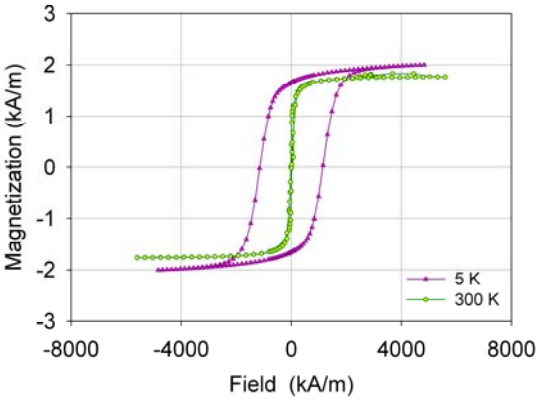

T_1= 200 ºC t_1=90 min T_2=315 ºC t_2=90 min

Run 5

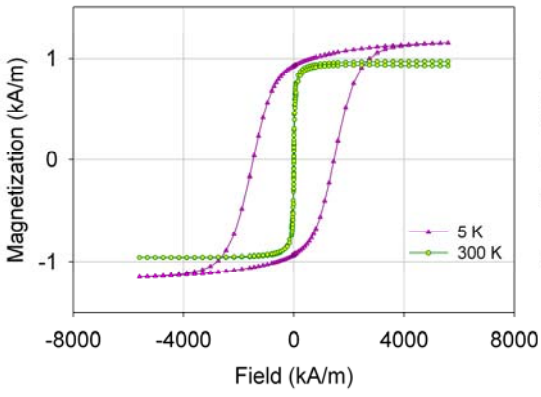

T_1= 150 ºC t_1=120 min T_2=330 ºC t_2=60 min

Run 6

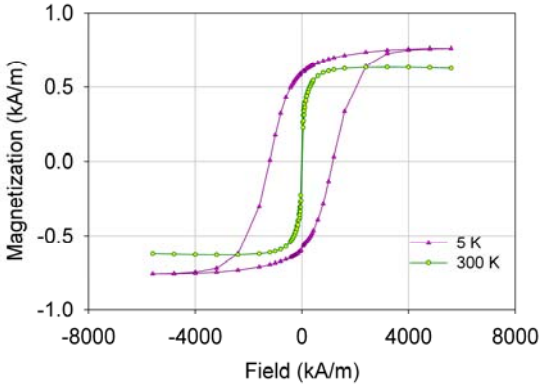

T_1= 250 ºC t_1=60 min T_2=330 ºC t_2=60 min

Run 7

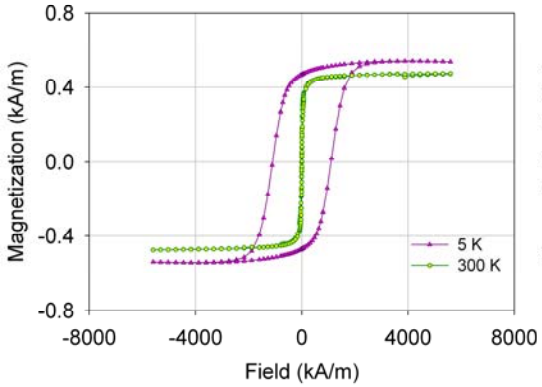

T_1= 200 ºC t_1=90 min T_2=315 ºC t_2=90 min

Run 8

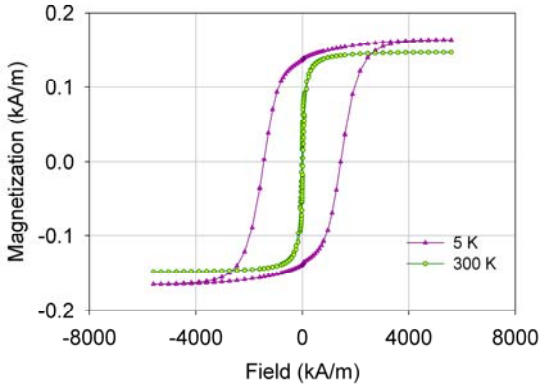

T_1= 250 ºC t_1=60 min T_2=300 ºC t_2=120 min

Run 9

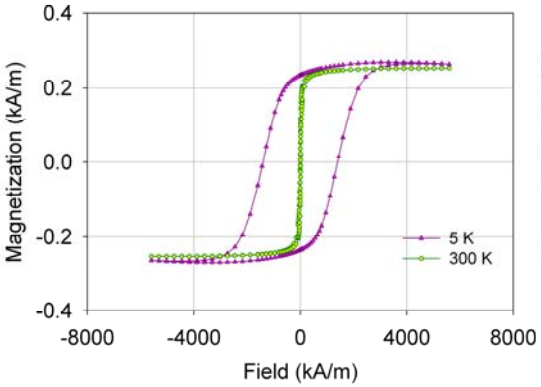

T_1= 150 ºC t_1=60 min T_2=330 ºC t_2=120 min

Run 10

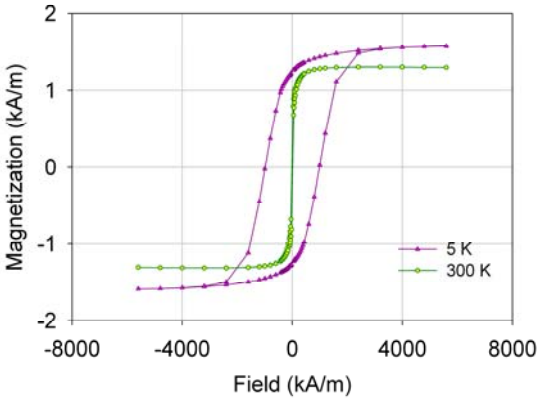

T_1= 150 ºC t_1=60 min T_2=300 ºC t_2=60 min

A.4. Statistical analysis using linear regression.

A.4.1. Regression between Fe/Co ratio and lattice parameter.

Term	Coeff	T	P
Constant	8.372	204.50	0.000
Fe/Co	0.006	0.36	0.728

R^2(adj)=0.0%

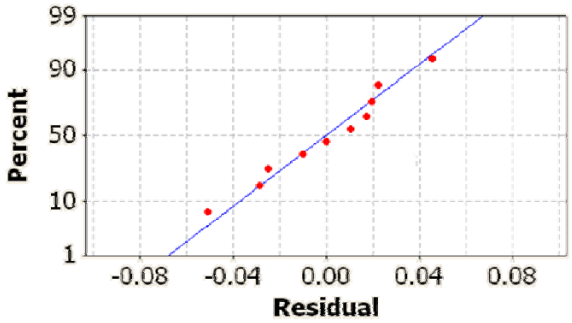

Normal probability plot of residuals for regression considering Fe/Co ratio as answer variable.

A.4.2. Regression between Fe/Co and coercivity

Term	Coeff	T	P
Constant	24.60	7.62	0.000
Fe/Co	-3.63	-2.53	0.039

R^2(adj)=40.3%

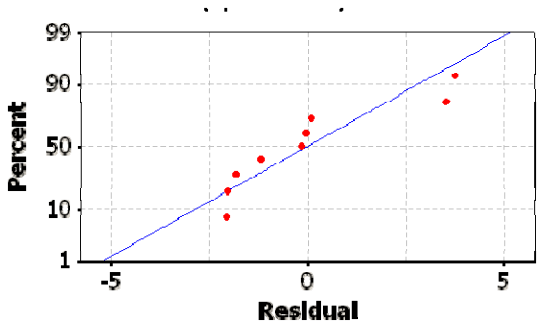

Normal probability plot of residuals for regression considering coercivity as answer variable.

A.4.3. Regression between Fe/Co and remanence reduced

Term	Coeff	T	P
Constant	0.86	22.44	0.00
Fe/Co	-0.02	-1.12	0.30

R^2(adj)=3.2%

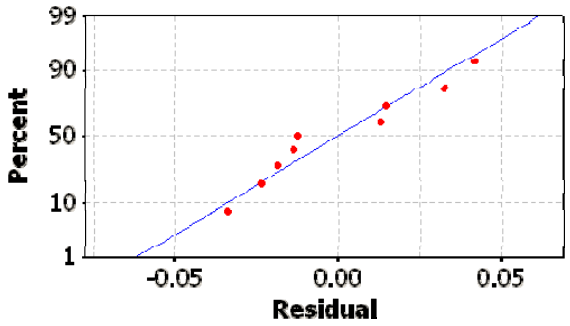

Normal probability plot of residuals for regression considering remanence reduced as answer variable.

A.4.4. Regression between Fe/Co and Saturation magnetization

Regression between Fe/Co ratio and saturation magnetization at 5 K.

Term	Coeff	T	P
Constant	81.21	2.11	0.07
Fe/Co	10.96	0.64	0.54

R^2(adj)=0.00%

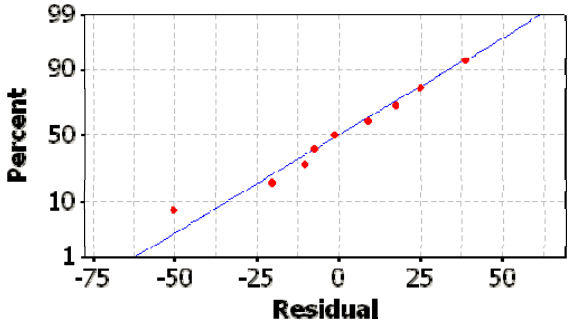

Normal probability plot of residuals for regression considering saturation magnetization at 5 K as answer variable.

Regression between Fe/Co ratio and saturation magnetization at 300 K.

Term	Coeff	T	P
Constant	66.14	1.97	0.09
Fe/Co	12.85	14.92	0.42

R^2(adj)=0.0%

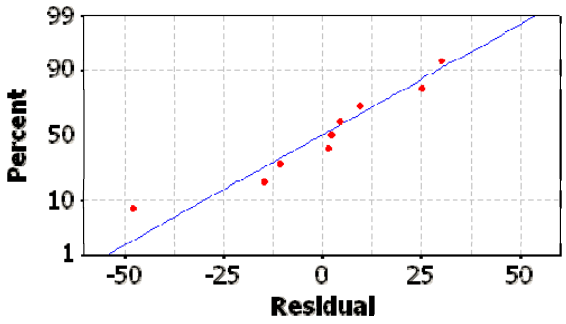

Normal probability plot of residuals for regression considering saturation magnetization at 300 K as answer variable.

A.4.5. Regression between particle diameter and coercivity.

Term	Coeff	T	P
Constant	16.02	2.37	0.05
Diameter	0.05	0.10	0.92

R^2(adj)=0.0%

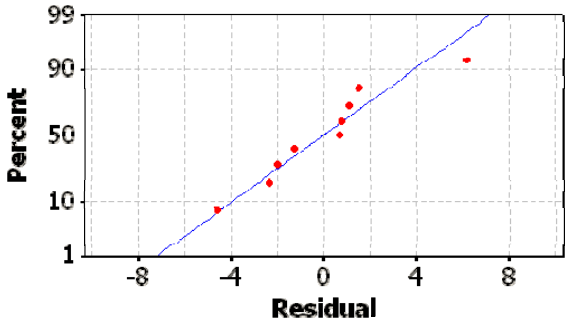

Normal probability plot of residuals for regression considering coercivity as answer variable.

A.4.6. Regression between particle diameter and remanence reduced.

Term	Coeff	T	P
Constant	0.73	13.71	0.00
Diameter	0.01	1.70	0.13

R^2(adj)=19.0%

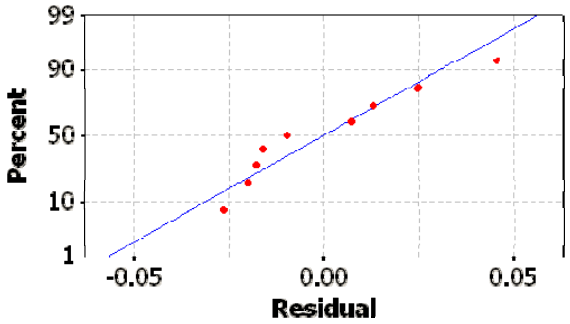

Normal probability plot of residuals for regression considering remanence reduced as answer variable.

A.4.6. Regression between particle diameter and saturation magnetization.

Regression between particle diameter and saturation magnetization at 5 K.

Term	Coeff	T	P
Constant	4.05	0.09	0.932
Diameter	8.14	2.23	0.061

R^2(adj)=33.1%

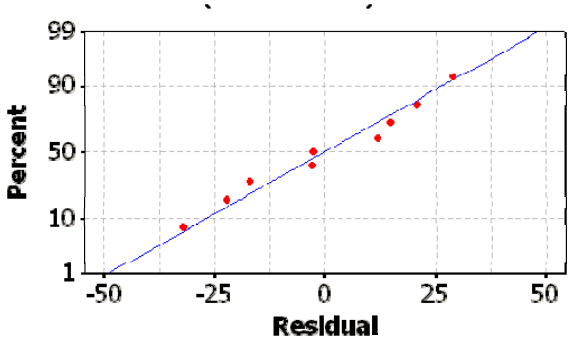

Normal probability plot of residuals for regression considering saturation magnetization at 5 K as answer variable.

Regression between particle diameter and saturation magnetization at 300 K.

Term	Coeff	T	P
Constant	11.10	0.26	0.804
Diameter	6.69	1.95	0.092

R^2(adj)=26.1%

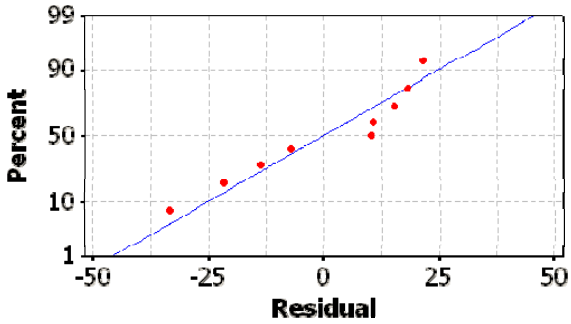

Normal probability plot of residuals for regression considering saturation magnetization at 300 K as answer variable.

APPENDIX B

Characterization of magnetite nanoparticles synthesized by the thermal-decomposition method described in Chapter 5.

B.1. Differential scanning calorimetry of polystyrene crosslinked with divinylbenzene (DVB).

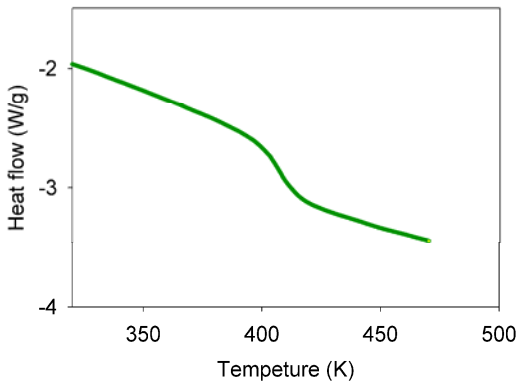

Polystyrene cross-linked with 10 % DVB.

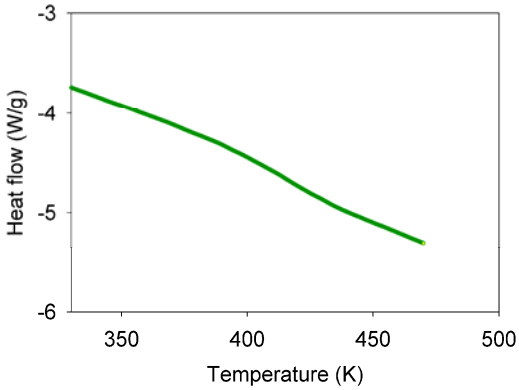

Polystyrene cross-linked with 15 % DVB.

B.2. Magnetization curve at low field for magnetite fixed in PSDVB at several concentrations.

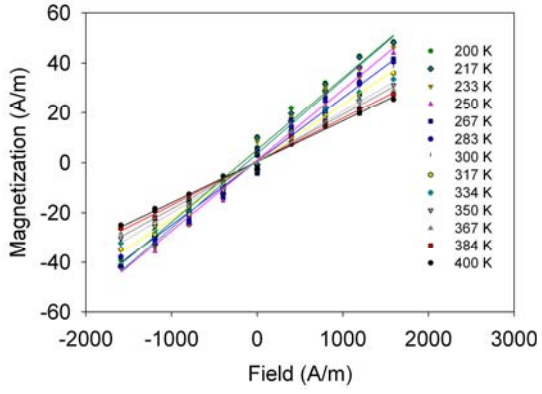

Magnetite at 0.1% in PSDVB

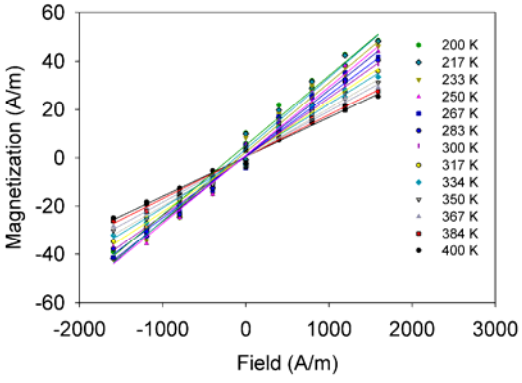

Magnetite at 1% in PSDVB

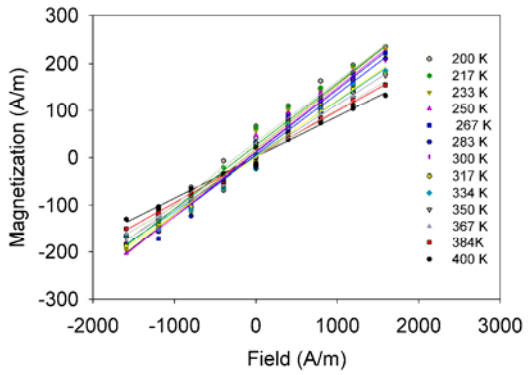

Magnetite at 6% in PSDVB

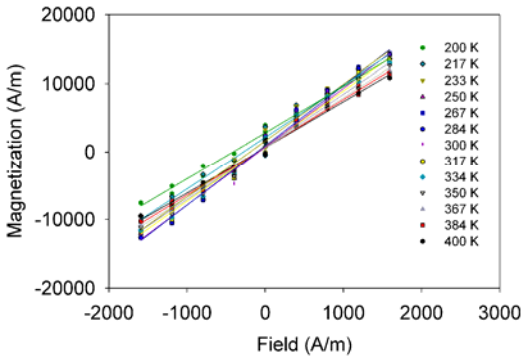

Magnetite at 33%

B.3. Initial susceptibility data fitted to Curie-Weiss model for magnetite fixed in PSDVB at several concentrations.

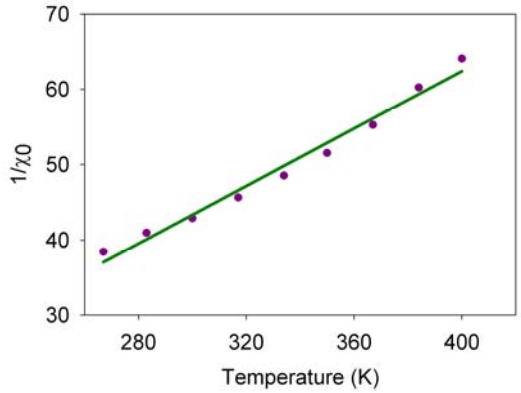

Magnetite at 0.1% in PSDVB

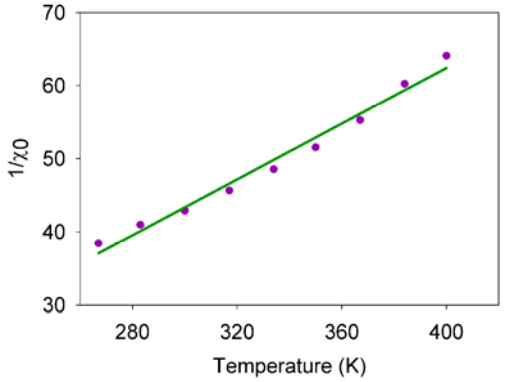

Magnetite at 1% in PSDVB

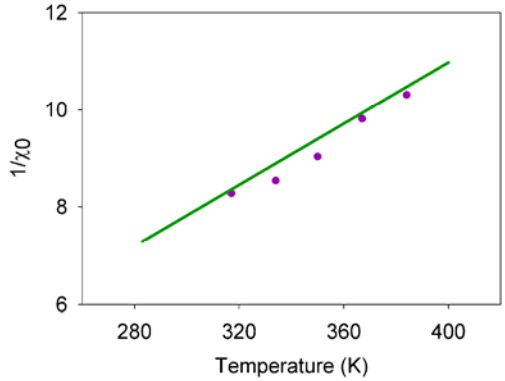

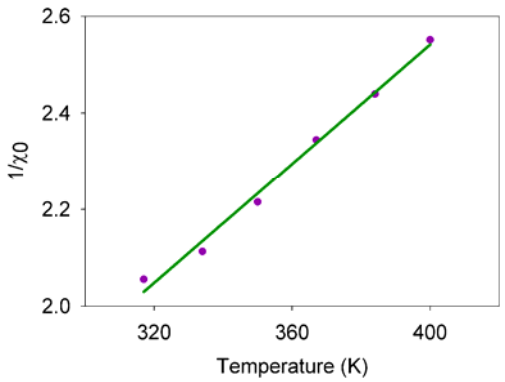

Magnetite at 6% in PSDVB Magnetite at 33%

B.4. Temperature-dependent in-phase component of dynamic susceptibility at several frequencies.

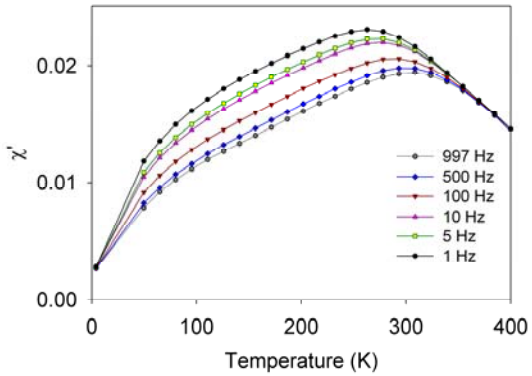

Magnetite at 0.1% in PSDVB

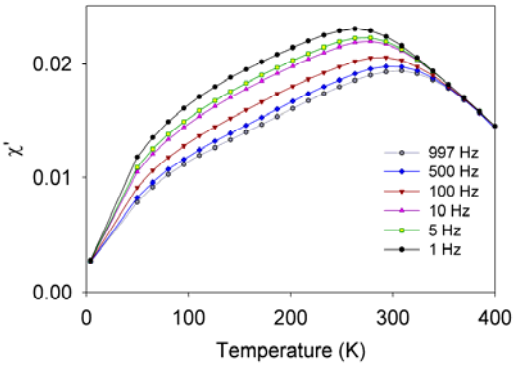

Magnetite at 1% in PSDVB

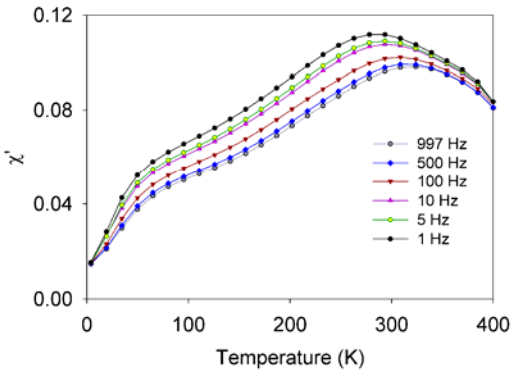

Magnetite at 6% in PSDVB

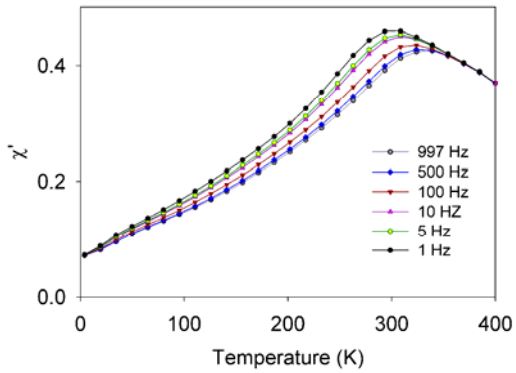

Magnetite at 33%

APPENDIX C

Characterization of magnetite nanoparticles synthesized by thermal-decomposition method described in Chapter 6.

C.1. Magnetization curve at low field for samples of magnetite with 9 nm and 11 nm diameter fixed in PSDVB.

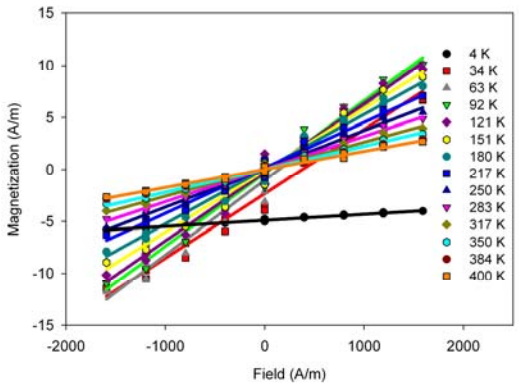

6 nm

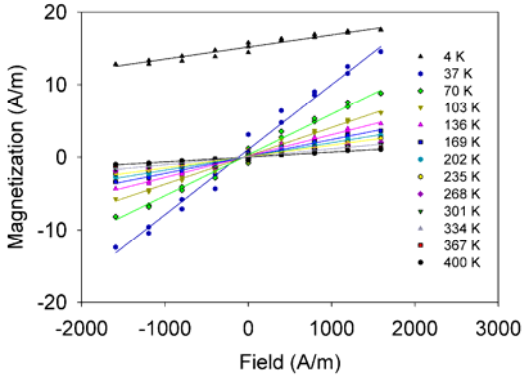

9 nm

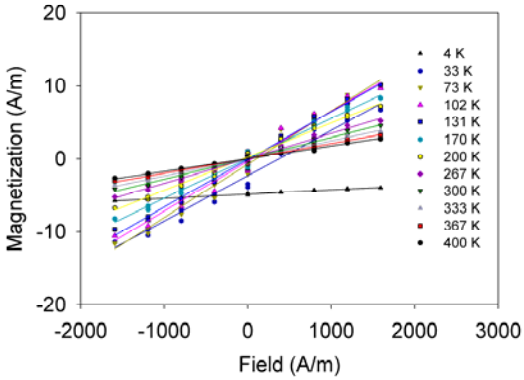

11 nm

C.2. Initial susceptibility data fitted to Curie-Weiss model for samples of magnetite with 9 nm and 11 nm diameter fixed in PSDVB.

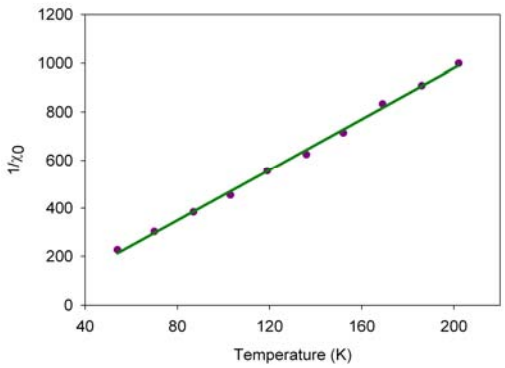

6 nm

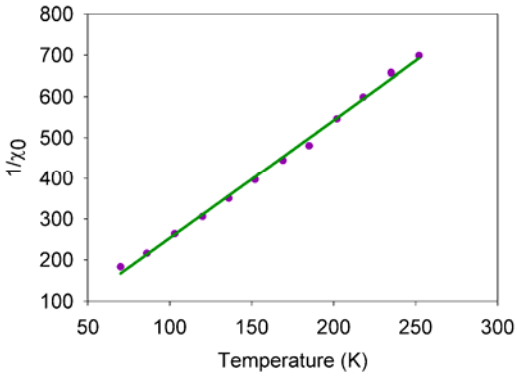

9 nm

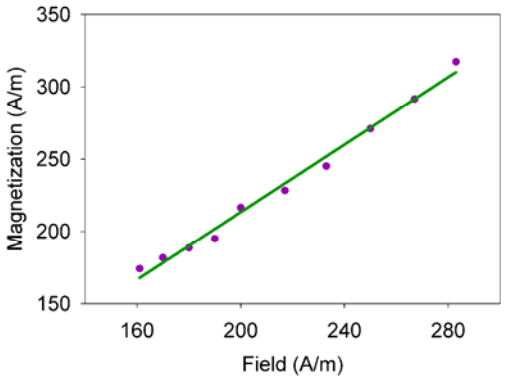

11 nm

C.3. Temperature-dependent in-phase component of dynamic susceptibility at several frequencies

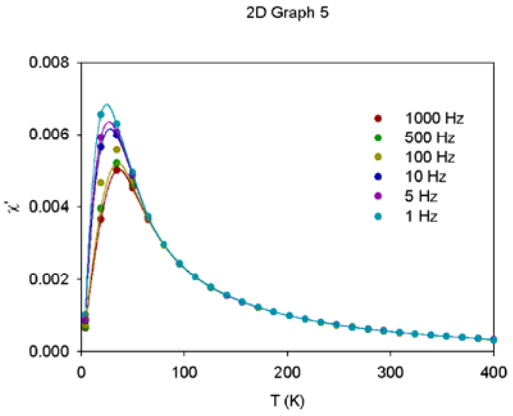

6 nm

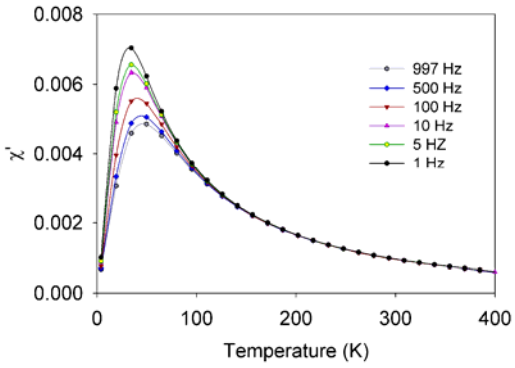

9 nm

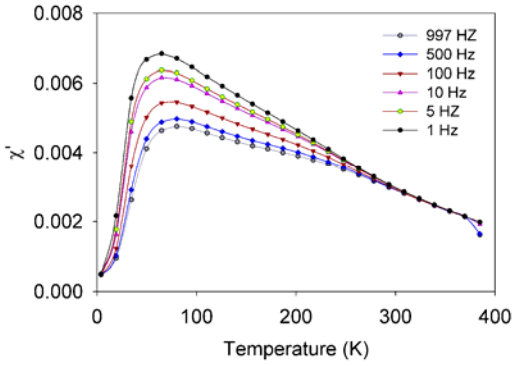

11 nm

C.4. Plot of the inverse applied field frequency as a function of the inverse temperature corresponding to the peak of in-phase component of dynamic susceptibility

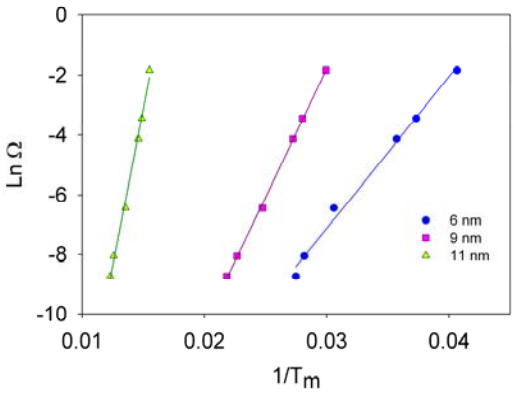

Néel model

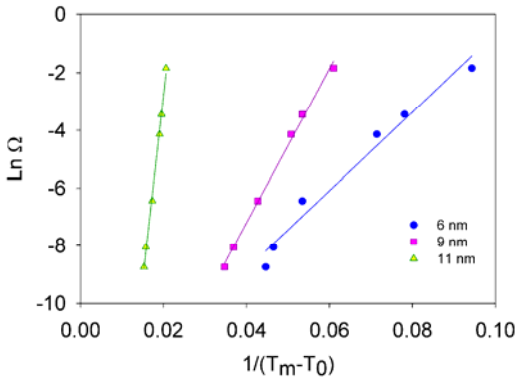

Vogel-Fulcher model